Irene Dalfen, BSc

Novel Long-Lifetime Fluorescent pH Indicators Based on Triangulenium Dyes

MASTER'S THESIS

to achieve the university degree of

Diplom-Ingenieurin

Master's degree programme: Technical Chemistry

submitted to

Graz University of Technology

Supervisor

Ass. Prof. kand. Sergey Borisov

Institute of Analytical Chemistry and Food Chemistry

Graz, March 2017

Warum leuchtet das...?

Abstract

In this thesis the functionalisation of diazaoxatriangulenium (DAOTA) dyes with photoinduced-electron-transfer (PET) groups was investigated. The aim was to test the applicability of these dyes for pH sensing, especially in the fluorescence decay time mode. Furthermore modification with bromine- and primary amine-linkers was attempted for future coupling of the dyes with a FRET acceptor or binding them covalently to a crosslinked polymer.

Triangulenium dyes are especially attractive for optical sensing, because their excitation/emission takes place in the red part of the spectrum ($\geq$560 nm) and the extraordinarily long fluorescence decay times enable lifetime-based read out, which is essentially self-referenced and hence preferable to intensity-based readout. DAOTA dyes were modified with PET groups containing secondary amines as well as phenol groups. The indicators were characterised in solution and immobilised in different hydrogels as well as in nanoparticles. While phenol PET-groups showed excellent PET efficiency, hardly any quenching of fluorescence was observed in dyes modified with an amine PET-group. Investigation of photostability showed highly satisfying light fastness of a PET modified DAOTA$^+$ dye.
Characteristic long luminescence lifetimes of up to 20 ns were observed in all media and with every dye. pH dependence of fluorescence intensity is described by sigmoidal calibration curves. More importantly, fluorescence lifetime decreased by 24-68 % (lifetime in protonated "on" state $\sim$18 ns) upon deprotonation in a sigmoidal manner, which makes the DAOTA$^+$ dyes promising candidates for fluorescence lifetime pH sensing. The lifetime in the deprotonated state is around 8 ns, which is still comparatively long for organic fluorophores. These properties are very attractive for fluorescence lifetime based sensing, which grants the enormous advantage of self referenced read out compared to colorimetric or fluorescence intensity based sensing. The successful preparation of nanoparticles might be the first step in designing intracellular probes for fluorescence lifetime imaging with DAOTA$^+$ dyes.

Kurzfassung

In dieser Arbeit wurde die Funktionalisierung von diazaoxatriangulenium (DAOTA) Farbstoffen mit Gruppen für photoinduzierten Elektronentransfer (PET) untersucht. Ziel war es, die Eignung dieser Farbstoffe für pH Sensorik zu validieren, mit besonderem Fokus auf Fluoreszenzlebenszeit-Messungen. Außerdem wurde angestrebt, diazaoxatriangulenium Farbstoffe mit Linkern wie Brom- oder primären Amingruppen zu modifizieren, um sie mit FRET Akzeptoren zu koppeln oder kovalent in ein quervernetztes Polymer zu integrieren.

Triangulenium Farbstoffe sind wegen ihrer langwelligen Absorption/Emission ($\geq$560 nm) und ihrer außerordentlich langen Fluoreszenz Abklingzeiten, welche selbst-referenzierte Lebenszeit basierte Messungen ermöglichen, besonders attraktiv für optische Sensorik. $DAOTA^+$ Farbstoffe wurden sowohl mit sekundären Amin- also auch Phenol-PET Gruppen modifiziert. Die Charakterisierung der Indikatoren erfolgte in Lösung sowie immobilisiert in verschiedenen Hydrogelen sowie in Nanopartikeln. Die PET Effizienz der Phenol-PET Gruppen erwies sich als exzellent während bei der Amin-PET Gruppe kaum Fluoreszenzlöschung zu berichten ist. Messungen der Photostabilität ergaben höchst zufriedenstellende Lichtbeständigkeit eines PET modifizierten $DAOTA^+$ Farbstoffs.
Die charakteristisch langen Fluoreszenzlebenszeiten von bis zu 20 ns konnten in all diesen Medien bei sämtlichen Farbstoffen beobachtet werden. pH Abhängigkeit der Fluoreszenzintensität kann mit sigmoidalen Kurven beschrieben werden. Noch wichtiger ist jedoch, dass die Fluoreszenzlebenszeit in sigmoidaler Weise um 24-68 % (Lebenszeit im protonierten "an" Zustand ~18 ns) abnimmt, wenn der Farbstoff deprotoniert wird. Das macht $DAOTA^+$ Farbstoffe zu besonders vielversprechenden Kandidaten für pH Sensorik mittles Fluoreszenzlebenszeit Messung. Die Lebenszeit in deprotoniertem Zustand beträgt immer noch um 8 ns, was für organische Fluorophore ein beträchtlicher Wert ist. Diese Eigenschaften sind sehr attraktiv für Lebenszeit basierte pH Sensorik, die im Vergleich zu kolorimetrischen oder Fluoreszenzintensität basierten Methoden den Vorteil der selbst-Referenzierung aufweist. Die erfolgreiche Herstellung von Nanopartikeln, die $DAOTA^+$ Farbstoffe enthalten, könnte wegweisend sein für Intrazelluläre Sonden und Bildgebende Fluoreszenzlebenszeit Messungen mit diesen Farbstoffen.

AFFIDAVIT

I declare that I have authored this thesis independently, that I have not used other than the declared sources/resources, and that I have explicitly indicated all material which has been quoted either literally or by content from the sources used. The text document uploaded to TUGRAZonline is identical to the present master‘s thesis.

EIDESSTATTLICHE ERKLÄRUNG

Ich erkläre an Eides statt, dass ich die vorliegende Arbeit selbstständig verfasst, andere als die angegebenen Quellen/Hilfsmittel nicht benutzt, und die den benutzten Quellen wörtlich und inhaltlich entnommenen Stellen als solche kenntlich gemacht habe. Das in TUGRAZonline hochgeladene Textdokument ist mit der vorliegenden Masterarbeit identisch.

13.03.2017	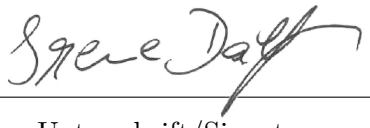
Datum/Date	Unterschrift/Signature

Danksagung

Ich möchte mich bei allen bedanken, die mich bei meiner Masterarbeit und auf meinem Weg dahin begleitet und unterstützt haben.
Sergey, danke, dass du mich in den vergangenen Monaten so tatkräftig betreut hast. Du hattest immer einen Rat für mich und dein fundiertes Wissen hat mir immer weitergeholfen. Vor allem inspiriert mich aber, wenn du durchs Labor saust, auf der Suche nach einem Proof-of-Concept oder um das Verhalten eines Farbstoffes zu untersuchen und dabei eine Begeisterung für alles Lumineszierende an den Tag legst, die ihresgleichen sucht ("Ich kann machen dass das besser leuchtet."-Sergey über Larissas magische Knete).
Vielen Dank an Ingo, dass ich die Möglichkeit hatte, in diesem tollen Team zu Arbeiten. Du hast mir durch deine vielen kritischen Fragen sehr oft geholfen, auch wenn sie mich im Moment manchmal ein bisschen ins Schwitzen gebracht haben.
Natürlich ein riesen Dankeschön an Eveline, die bei jedem Problem eine Lösung entweder schon parat hat oder in kürzester Zeit findet.
Ein Dank gebührt auch Tobias Burger, ohne den ich damals nicht als Oompa Loompa ans Institut gekommen wäre. Diese Zeit war eine tolle Erfahrung und ich habe viel von Dir gelernt!
An die gesamte Arbeitsgruppe: Ihr wart die besten Kollegen, die man sich wünschen kann, habt mir immer weitergeholfen, wenn ich eine Frage hatte und habt auch in der Freizeit für viel Spaß und Abwechslung gesorgt, sei es beim Feierabend-Bier, beim Beachvolleyball spielen, beim Business-run oder einfach beim Kaffee trinken. Diesbezüglich danke an Peter fürs Organisieren unterschiedlichster Aktivitäten. An meine Masterstudi-Kollegen Andi, Luki, Max, Tanja, Nici und Nicola: es war eine Freude mit euch zu studieren und zu arbeiten! Ein besonderes Dankeschön an Christoph, fürs Korrekturlesen meiner Arbeit und die wertvollen Beiträge bei den Gruppenseminaren. Außerdem *Danke Luki* (und Fips und Christoph) für die Hilfe beim Schreiben der Arbeit mit LaTeX und an Max, fürs gemeinsame Problemsuchen. Überhaupt habe ich mit Max, Birgit und Sergey ganz tolle Bürokollegen, mit euch teile ich immer gerne meine Schokolade oder ziehe als heimlicher Nikolaus mit euch durchs Institut ;)
Viele schöne Erinnerungen teile ich auch mit meinen Freunden außerhalb der Arbeitsgruppe von denen ich besonders Larissa und Meli hervorheben möchte. Ihr habt maßgeblich zu einer tollen Studienzeit beigetragen.
Ein riesengroßes Dankeschön gebührt natürlich auch meiner Familie, ohne die ich das alles nie geschafft hätte. Natürlich bin ich euch dankbar für die finanzielle Unterstützung, die mir ein so sorgenfreies Studium ermöglicht hat. Viel wichtiger ist mir aber, dass ihr immer für mich da

wart. Meiner Godi samt Familie vielen Dank dass ihr immer an mich geglaubt habt und oft viel mehr von mir überzeugt wart als ich selber. Danke Opa, dass du mich immer motiviert hast mein Bestes zu geben. Andi, danke dass du mich an der Hand nimmst, wenn ich etwas allein nicht schaffe! Der größte Dank gebührt meinen Eltern, die immer für mich da waren und mir in jeder Lebenslage zur Seite gestanden sind! Abschließend danke ich Gregor, der mich in den letzten Jahren auf meinem Weg begleitet hat und mir immer geholfen hat, auch in stressigen Zeiten den Überblick zu behalten.

Irene Dalfen, BSc Graz, March, 2017

Contents

1 Introduction

Many biological and ecological systems are based on a delicate equilibrium between a wide range of different parameters. One of the most important is the pH, which is not only relevant in biology/biotechnology, but also in medicine, oceanography, environmental monitoring to mention only a few fields. [1–6]

Intracellular pH monitoring is essential for the investigation of many biological processes [1, 2]. However, measurement of physiological pH, while being important in medical applications, is impeded by many factors. Among them are highly scattering and absorbing samples, small sample volumes and the necessity of non-invasive methods.
In environmental science, delicate equilibriums exist that can easily be compromised by change in pH which is often accelerated by anthropogenic activities. Examples include acid rain [3] leading to acidification of surface water and ocean acidification due to high atmospheric CO_2 levels. [4] that ultimately leads to destruction of coral reefs [5] and thinning in calcareous shells of sea organisms and plankton [6].
Those are just a few examples highlighting the necessity of accurate and continuous pH monitoring in many different environments.

Optical pH chemosensors proved to be powerful analytical tools since they are free from electromagnetic interferences, enable non-invasive measurement and are available in a variety of formats ranging from planar optodes and fiber optic sensors to nanoparticles [7]. Fibre optic sensors also enable measurement from great distances (up to 1000 m), in case the measurement has to be conducted in inaccessible places or harsh environments. Some optical pH sensors have been commercialised and are applied in academia and industry alike. Many pH indicators rely on changes in absorption properties [8] or luminescence intensity [9], however both methods have limitations concerning coloured and turbid samples.
Fluorescence decay time measurement is essentially self-referenced and if the excitation/emission occurs in the red part of the spectrum (above ∼550 nm), minimal influence from biological components is to be expected [10]. However, not many pH indicators exist, that fulfill those requirements along with those of high luminescence quantum yields, good photostability, long decay times and a pK_a in the physiological range.

In this thesis, triangulenium dyes were chosen as a platform for design of novel pH indicators. These super stabilised cationic dyes exhibit fluorescence decay times of around 20 ns and their

absorption and emission spectra can be bathochromically shifted by substituting the oxygen- with nitrogen-bridges so that λ_{abs}max of 560 nm is obtained which is the wavelength range typical for many established chromophores (rhodamines, BODIPYs). While the absorption coefficients of triangulenium dyes are moderate, their high quantum yields lead to good luminescence brightness. The long decay time of diazaoxatriangulenium dye [11] was already demonstrated to be very useful for elimination of cellular autofluorescence [12]. Although the pH sensitivity can be introduced by synthesising the fluorescein-similar trihydroxytrioxatriangulene [13], the lifetimes of this dyes do not exceed 4.3 ns in any protonation/deprotonation state, thus eliminating the strongest advantage of this dye group.
Therefore, modification of diazaoxatriangulenium dyes with PET groups was chosen instead as a pathway to obtain pH indicators with long-lived fluorescence and long wavelength. Additionally the PET modified $DAOTA^+$ dyes promise to display different pK_a values depending on the nature of the receptor.

2 Theoretical Background

2.1 Luminescence

This section is based on references [14] and [15], all other references will be pointed out explicitly. Luminescence is regarded as the emission of light from an electronically excited state, usually accompanied by relaxation of the luminophore to the electronic ground state. There are different types of luminescence depending on the source for the energy of excitation and the nature of the excited state from which the emission takes place. Among the various modes of excitation (through radioactive irradiation, temperature, electric energy,...) only excitation through irradiation with light in the UV/Vis range is of interest for this thesis.

2.1.1 Absorption of Light

Excitation of a luminophore through UV/Vis irradiation is based on the absorption of light which leads to promotion of an electron from an occupied molecular orbital to an unoccupied, antiboding molecular orbital of the luminophore. Depending on the kind of molecular orbitals involved in this process, different transitions can take place. A rather simple example that still covers the most important transitions is formaldehyde. In this case the electrons from the σ and π molecular orbitals of the carbonyl double bond can take part in the excitation process, as well as the electron lone pairs on the oxygen.

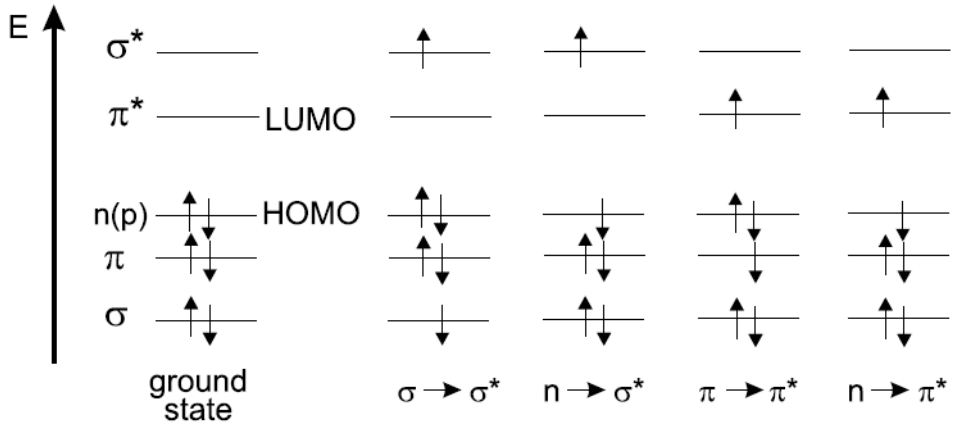

Figure 2.1: Possible transitions in a formaldehyde molecule when irradiating with UV/Vis light [15]

The energy of these transitions is higher if the MO the electron originates from and the MO

it is excited to have a big difference in potential energy. As a result the $\sigma \rightarrow \sigma^*$ transition has the highest energy of all transitions depicted in figure 2.1 while the n $\rightarrow \pi^*$ transition has the lowest energy. The energy of the transition is related to the wavelength of the absorbed light according to equation 2.1.

$$\Delta E = h \cdot \nu \tag{2.1}$$

ΔE denotes the energy difference between excited state and ground state, h is the Planck constant and ν the irradiation's frequency, related to the wavelength, λ via the speed of light c.

$$\lambda = \frac{c}{\nu} \tag{2.2}$$

In conjugated systems the energy of the $\pi \rightarrow \pi^*$ transition becomes smaller the bigger the conjugated system is, leading to a bathochromic shift in the absorption spectrum.

The transitions shown in figure 2.1 occur from a molecule in singlet state to an excited singlet state of this molecule. In each case, one out of two paired electrons is promoted to an unoccupied MO, during which its spin does not change and also the overall spin quantum number stays the same $S = \sum s_i = 0$ with $s_i = \pm\frac{1}{2}$. The spin multiplicity ($M = 2S + 1$) in both cases is one, which makes the ground and excited state singlet states. In some cases, an excited electron can change it's spin so that the spin is parallel to that of the unpaired electron remaining in the ground state. The overall spin quantum number in this case will be $S = 1$, the spin multiplicity consequently is $M = 3$, meaning there are three states of equal energy which is denoted as a triplet state. Hund's rule states that a triplet state will have lower energy than a singlet state having the same configuration (figure 2.2).

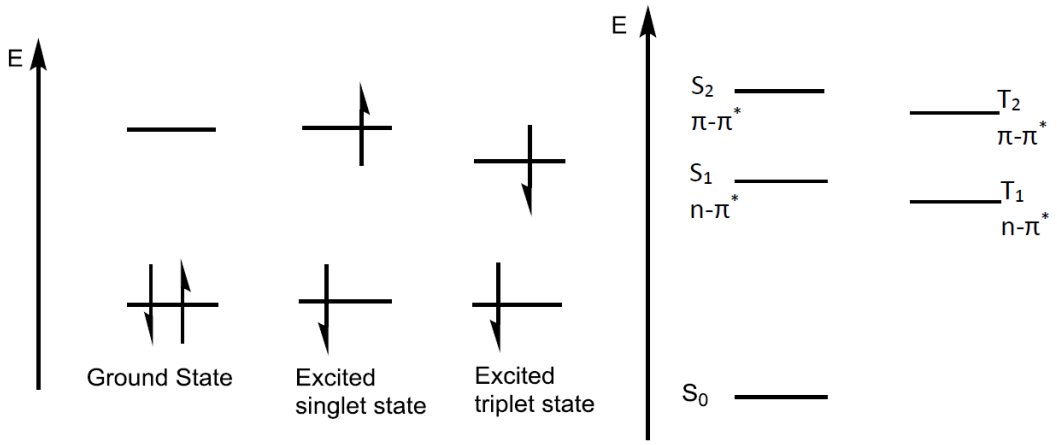

Figure 2.2: Energy diagram of singlet and triplet excited states of formaldehyde

The Absorption Spectrum

The efficiency of light absorption of a certain medium is experimentally defined by it's absorbance, A, and described by equation 2.3

$$\begin{aligned} A(\lambda) &= log\frac{I_\lambda^0}{I_\lambda} = -logT(\lambda) \\ T(\lambda) &= \frac{I_\lambda}{I_\lambda^0} \end{aligned} \tag{2.3}$$

I_λ^0 and I_λ are representing the intensity of the incident light beam and the beam leaving the absorption medium respectively while $T(\lambda)$ is the transmittance. In dilute solutions the absorption follows Beer-Lambert's law.

$$A(\lambda) = c \cdot l \cdot \varepsilon(\lambda) \tag{2.4}$$

Where l is the optical pathway through the measurement solution, c the concentration of the dye solution in $mol \cdot L^{-1}$ and ε the molar absorption coefficient in $L \cdot mol^{-1}cm^{-1}$. Deviations from linear dependence of Beer-Lambert's law can occur in concentrated solutions for example because of aggregation.
Classical view of light absorption states that ε depends on the *oscillator strength* of a molecule that is considered an oscillating dipole. The higher the oscillator strength, the higher is the molar absorption coefficient of a molecule. In quantum mechanics, the transient dipole which is created by charge displacement during excitation is considered by introduction of a so called transition moment. This is especially important for experiments with polarized light because molecules are excited preferentially when their transition moment is parallel to the electric vector of the incident light that is linearly polarized.
The two main selection rules, determining if a transition is allowed, are:

Spin-forbidden transitions: Transitions between states of the same spin multiplicity (singlet-singlet, triplet-triplet) are allowed while a transition that results in a change of spin multiplicity (singlet-triplet or vice versa) is forbidden. However, spin-orbit-coupling results in a small interaction between the wavefunctions of different spin multiplicities, leading to small fractions of wavefunctions of the relative other spin multiplicity in the wavefunction of a singlet or triplet state. As a result, transitions between different spin multiplicities can effectively be observed.

Symmetry-forbidden transitions: Symmetry may also be the reason why certain transitions are forbidden. Since at temperatures >0 K vibrations slightly distort a molecule's symmetry, those transitions take place nonetheless. However, molar absorption coefficients of those transitions are usually small and distinct vibronic bands can be observed in the corresponding absorption spectra.

The Franck-Condon Principle

The Born-Oppenheimer approximation states, that the motion of electrons is much more rapid than that of atomic nuclei (as e.g. in molecular vibrations). The timescale of electron-promotion is in the area of 10^{-15} s while vibronic transitions occur at a timescale of $10^{-12} - 10^{-10}$ s. As a result the Franck-Condon principle states that an electronic transition occurs without change in position of the atomic nuclei in the molecule. Quantum mechanically, the transition occurs from the lowest vibrational state of the ground state to that vibrational state of the excited state, whose vibrational wavefunction most resembles that of the ground state. In classical theory, the transition occurs when the distance between the nuclei is equal to the equilibrium bond length in the ground state and the position of the nuclei does not change while the vertical transition (promotion of the electron) is in progress. The terminal point of the transition is the intersect between the vertical line and the potential energy curve of the lowest excited state. Once the transition is complete the molecule starts vibrating at the frequency corresponding to the energy of the excited vibrational state.
Since there is a continuous set of vibrational sublevels to each electronic energy level, homogeneous band broadening is observed in absorption spectra. At room temperature the molecule is in it's lowest vibrational state according to Boltzmann, and the purely electronic transition is a 0-0 transition to the lowest vibrational state of the excited state. The transition with the next higher energy is to the first vibrational level of the excited state (0-1) and so on. The intensities of the vibronic transitions depends on the relative shape and position of the potential energy curves. Inhomogeneous band broadening can be observed due to fluctuations of the solvation sphere in solution. The Franck-Condon principle is illustrated in figure 2.3.

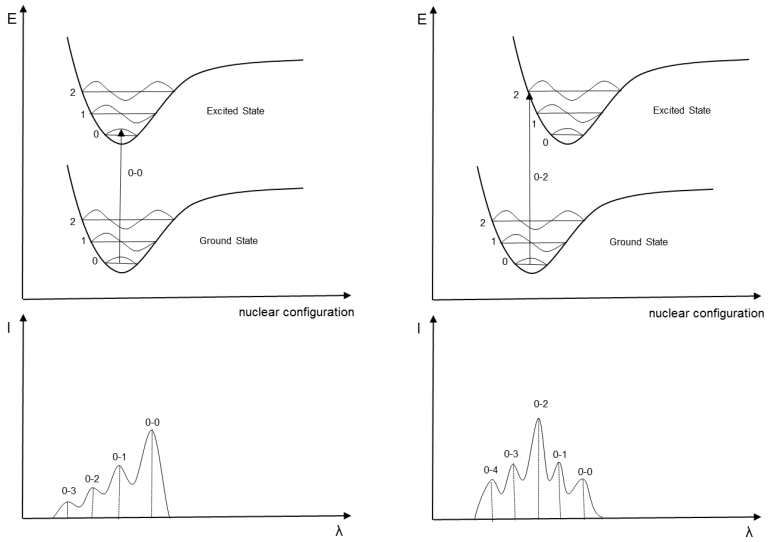

Figure 2.3: Illustration of the Franck-Condon principle. Top: potential energy curves and vertical transitions; Bottom: resulting absorption spectra for gas phase (dotted lines) and in solution (solid curves)

2.1.2 De-Excitation Mechanisms

There are multiple ways for an excited molecule to return to it's ground state. The Jablonski diagram (figure 2.4)is a compact way of visualising the different transitions that can take place in a molecule upon promotion of an electron [16]. Here the electronic ground state is denoted as S_0 and the first and second excited states as S_1 and S_2.

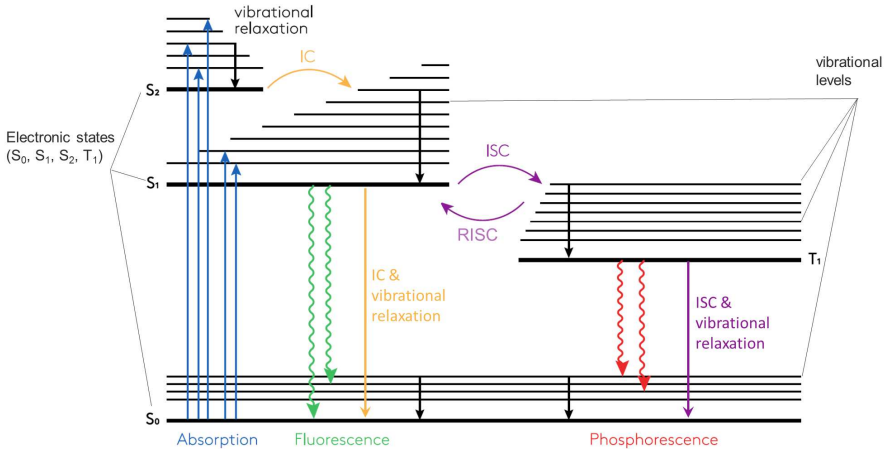

Figure 2.4: Perrin-Jablonski diagram displaying most common transitions from an electronically excited state; figure adapted from [17]

In figure 2.4, the most important transitions following excitation by visible/UV light are displayed. They are explained in detail in the following paragraphs.

Internal Conversion (IC)

Internal conversion describes a non-radiative transition between two electronic states of the same spin multiplicity. Happening in a timescale of $10^{-11} - 10^{-9}$ s, this process is rapid and usually completed before emission takes place. In solution, vibrational relaxation to the lowest vibrational level of S_1 (the thermally equilibrated excited state) takes place and the excess energy is passed on to the surrounding solvent molecules via collision.
In theory, IC can also occur from S_1 to S_0, however, the energy gap is much higher than between S_2 and S_1, which is why IC to the ground state is much slower.

Fluorescence

An excited molecule may undergo radiative relaxation, usually from the thermally equilibrated excited state (S_1) to it's ground state (S_0). This transition is called fluorescence. The energy of fluorescence transitions is usually independent from the wavelength of the excitation light source, because as discussed above, before emission takes place, the molecule relaxes to the lowest vibrational level of S_1 via internal conversion. This independence of emission wavelength from the energy of exciting light is called *Kasha's rule* [18]. Because the nuclear geometry

of a fluorophore is not drastically altered during electric excitation, the spacing between the vibrational levels in the excited and in the ground state are very similar. As a result the fluorescence emission spectrum often is the mirror image to the absorption spectrum (*mirror image rule*). However, fluorescence emission always occurs at higher wavelengths than the corresponding excitation. This is due to energy loss during vibronic transitions from higher vibrational levels of S_1 or even S_2 to the thermally equilibrated excited state before emission takes place as well as from higher vibrational levels of the ground state to the lowest vibrational level of S_0. This behaviour was first published by Stokes [19]. However, there might still exist an overlap between excitation and emission spectrum at room temperature, meaning that some fluorescence transitions have a higher energy than certain absorption transitions. This *energy defect* is possible because at room temperature some molecules may be in a higher vibrational level of S_0. The distribution between the different vibrational levels of the ground state follows Boltzmann's law.

$$\frac{N_1}{N_0} = e^{-\left(\frac{E_1 - E_2}{kT}\right)} \tag{2.5}$$

In equation 2.5 N_0 and N_1 denote the number of molecules in the vibrational levels 0 and 1 and E_0 and E_1 the corresponding energy. Furthermore k is the Boltzmann constant and T the temperature in Kelvin. This deviation from Stokes law should disappear at lower temperatures when higher vibrational levels of the ground state are not populated any more.

Intersystem Crossing (ISC)

Intersystem crossing is another non-radiative transition. In contrast to internal conversion it is a spin forbidden transition between two isoenergetic vibrational levels of different spin multiplicity. The transition occurs between the lowest vibrational level of S_1 and the vibrational level of T_1 with the same energy at a timescale of $10^{-10} - 10^{-4}$ s and is followed by rapid vibronic transition to the lowest vibrational level of T_1. Even though ISC is in principle forbidden, spin-orbit coupling leads to successful transitions. Spin-orbit coupling describes an interaction between the magnetic moment that arises from the electrons spin around its own axis and the magnetic moment arising from its revolving around the atomic nucleus. As a result the wavefunctions of the singlet and triplet state each contain a small fraction of the wavefunction of the corresponding other state, enabling transitions between states of different spin multiplicity ($\Psi = \alpha^1\Psi + \beta^3\Psi$). Spin-orbit coupling is increased by presence of heavy atoms such as bromine (*heavy atom effect*).

Reverse Intersystem Crossing (RISC) and Delayed Fluorescence

From an excited triplet state, several different relaxation processes can take place (see figure 2.5). One of them is reverse intersystem crossing, the transition back to the excited singlet state. RISC can take place if the energy levels of the excited singlet and triplet states are

very similar and if the lifetime of T_1 is long enough. Often additional energy (e.g. in the form of temperature) is necessary to enable RISC. If after RISC, radiative decay from S_1 to S_0 takes place, the emission spectrum will have the same shape and wavelength as regular fluorescence. The lifetime however will be significantly longer, because the molecule stays in the excited triplet state for some time. For this reason, radiative emission from S_1 after RISC is called *delayed fluorescence*. If the energy for RISC was supplied by elevated temperature, the phenomenon is called *thermally activated delayed fluorescence* (TADF). Apart from RISC, triplet-triplet annihilation can also lead to delayed fluorescence.

Phosphorescence

If radiative decay takes place from T_1 to S_0, the process is called *phosphorescence*. Since this is another spin-forbidden process, made possible by spin-orbit coupling, phosphorescence is a rather slow transition. At room temperature, non-radiative decay is predominant for most molecules compared to phosphorescence since it is facilitated through collisions with solvent molecules leading to intersystem crossing and vibrational relaxation to the ground state. The lifetime of the excited triplet state can range from microseconds up to several seconds. Phosphorescence efficiency can be drastically increased at low temperatures and upon immobilisation in rigid matrices due to lower quenching probabilities of the triplet state.
Because the lowest vibrational level of T_1 is lower in energy than that of S_1, phosphorescence emission is shifted to higher wavelengths than fluorescence.

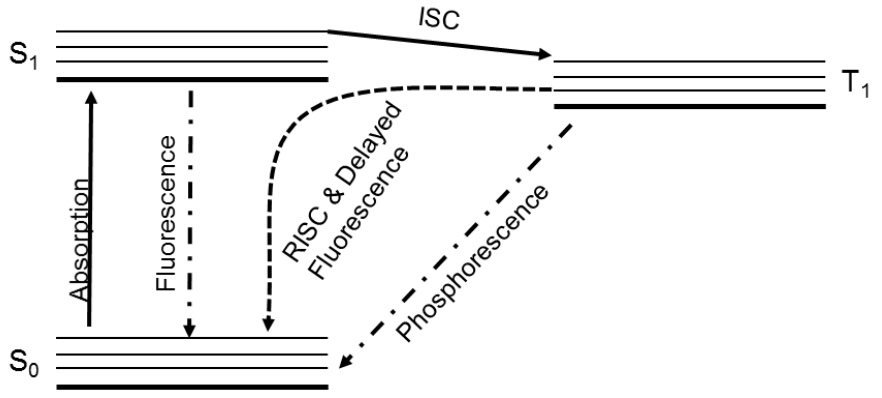

Figure 2.5: Intersystem crossing and possible de-excitation pathways from an excited triplet state as compared to fluorescence

2.1.3 Luminescence Decay Time

The radiative transition from an excited singlet or triplet state is a very fast process ($\sim 10^{-15}$), the radiative decay curve is therefore determined by the lifetime of the excited S_1 or T_1 state. Without intermolecular quenching processes, an excited singlet state has a lifetime of $10^{-10} - 10^{-7}$ s, before either fluorescence or non-radiative decay leads to relaxation to the

ground state. Because transitions to S_0 or S_1 from T_1 are spin forbidden, deactivation processes from an excited triplet state are much less likely and consequently the lifetime of T_1 is with $10^{-6} - 1\,s$ much longer than that of S_1. If an excited singlet state is considered, the possible deactivation pathways and their corresponding rate constants are:

radiative deactivation $S_1 \rightarrow S_0$ (fluorescence), k^S_{rad}

non-radiative deactivation $S_1 \rightarrow S_0$ (internal conversion), k^S_{IC}

non-radiative deactivation $S_1 \rightarrow T_1$ (intersystem crossing), k^S_{ISC}

When looking at fluorescence emission, the rate constants of all competing, non-radiative deactivation can be summed up to $k^S_{nr} = k^S_{IC} + k^S_{ISC}$. If a very short light pulse excites a certain portion of molecules in a dilute solution ($[A] \rightarrow [A^*]$) at time 0 to S_1, the rate at which the excited molecules return to the ground state via any of the processes named above can be written as:

$$-\frac{[A^*]}{dt} = (k^S_{rad} + k^S_{nr}) * [A^*] \tag{2.6}$$

Integration leads to:

$$[A^*]_t = [A^*]_0 \cdot e^{(-(k^S_{rad}+k^S_{nr})\cdot t)} \tag{2.7}$$

The lifetime of the excited singlet state can be described as $\tau^S = \frac{1}{(k^S_{rad} + k^S_{nr})}$. The fluorescence intensity (in mole of photons per unit of time and volume) at a certain time t after excitation with a short light pulse at time *t=0* is proportional to the concentration of excited species at that time $[A^*]_t$ with the rate constant for radiative decay being the proportionality factor.

$$i_F(t) = k^S_{rad} \cdot [A^*]_t \tag{2.8}$$

Where the concentration of excited species at any given time t is defined by equation 2.9.

$$[A^*]_t = [A^*]_0 \cdot e^{\left(-\frac{t}{\tau^S}\right)} \tag{2.9}$$

In a macroscopic sample of a fluorophore, the fluorescence lifetime of a compound is defined as the average time, a molecule of this component stays in the excited state.
Determining the lifetime of a component can be experimentally done in the time and in the frequency domain (pulse- or phase-modulation fluorimetry).

Time Domain Lifetime Measurements

In this method, excitation is done with a short light pulse (δ-pulse, much shorter than τ) and the fluorescence intensity is recorded over time. In the simplest case the intensity at a given

time t follows a single exponential decay curve.

$$I(t) = I_0 e^{\left(\frac{-t}{\tau}\right)} \tag{2.10}$$

If this is the case, the lifetime can be gathered from the slope of the curve *log I(t)* vs. *t*.
In reality, the excitation pulse is not infinitely short and deconvolution of the fluorescence response, which is the convolution product of the excitation function and the δ pulse response, is necessary.
One widely used technique for experimentally determining lifetime via pulse fluorimetry is time corelated single photon counting (TCSPC). It is based on the fact that the probability of detecting a single (emitted) photon at a certain time after the excitation pulse is proportional to the fluorescence intensity at that time. In practice, less than one photon per pulse is recorded, to avoid recording two photons per excitation pulse. The decay curve is imitated by a histogram of the pulse heights after many excitation/detection events. Deconvolution, if necessary, is achieved by recording the excitation pulse time profile under measurement conditions by use of a scattering sample solution (e.g. dispersion of poly-(*N*-vinylpyrrolidone-co-styrene), colloidal silica).
Advantages of TCSPC include high sensitivity, extraordinary dynamic range and linearity (10^3-10^4) and well defined statistics.

Frequency Domain Lifetime Measurements

The excitation light used in frequency domain or phase-modulation fluorometry is sinusoidally modulated at high frequency. The convoluted response is analysed directly in the frequency domain, which makes deconvolution unnecessary. The response is modulated sinusoidally at the same frequency as the excitation light but shifted in phase and sometimes demodulated. This harmonic repsonse is the Fourier-transform of the δ-pulse response The demodulation factor M describes the modulation depth (AC/DC ratio) of the emission relative to that of the excitation light. The phase shift Φ describes the delay between absorption and emission and is usually measured from the zero-crossing times of both modulated

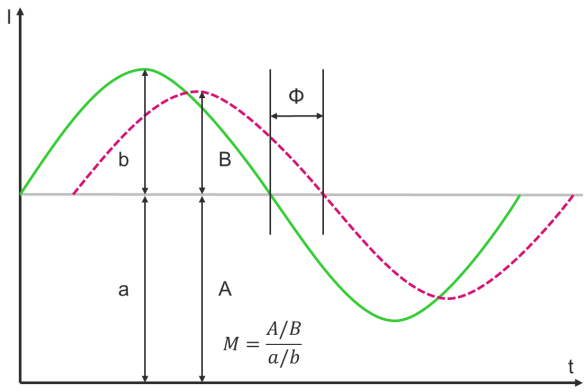

Figure 2.6: Phase shift and demodulation in a frequency domain lifetime measurement;
A/a=AC-part of fluorescence/excitation respectively, B/b=DC-part of fluorescence/excitation respectively, Φ=phase shift (solid line: excitation, dotted line: emission)

components (see figure 2.6). Both, phase shift and demodulation are functions of the modulation frequency ω (in radians/s). In case of a simple, single exponential decay, the fluorescence lifetime can be calculated from the phase shift or the demodulation, both should yield identical results.

$$\tau_\Phi = \frac{1}{\omega} tan\Phi \qquad (2.11) \qquad\qquad \tau_M = \frac{1}{\omega}\left(\frac{1}{M^2} - 1\right)^{\frac{1}{2}} \qquad (2.12)$$

The frequency range used in a phase-modulation measurement depends on the (expected) decay time of the sample. It should be in an order of magnitude, that $\omega\tau$ is close to 1 ($f \approx \frac{1}{2\pi\tau}$). This would result in an optimum measurement frequency of about 16MHz for a component with a lifetime of 10 ns.

2.1.4 Quantum Yield

Luminescence quantum yield is defined as the number of emitted photons per number of absorbed photons. Since without the influence of an external quencher, the competing processes are the same as when considering excited state lifetimes, fluorescence quantum yield can be calculated as follows:

$$\Phi^F = \frac{k^S_{rad}}{k^S_{rad} + k^S_{nr}} = k^S_{rad} \cdot \tau^S \qquad (2.13)$$

An alternative way of calculating the quantum yield of a deactivation process is by using equations 2.8 and 2.9 to calculate the number of emitted photons ($i_F(t)$) per photons absorbed ($[A^*]_0$).

$$\frac{i_F(t)}{[A^*]_0} = k^S_{rad} \cdot e^{\left(-\frac{t}{\tau^S}\right)} \qquad (2.14)$$

To determine the quantum yield of the entire emission process, this expression has to be integrated over time from the beginning of the emission process($t = 0$) until it's end ($t = \infty$).

$$\frac{1}{[A^*]_0}\int_0^\infty i_F(t)dt = k^S_{rad} \cdot \tau^S = \Phi^F \qquad (2.15)$$

The same way, quantum yield can be calculated for phosphorescence, by using the corresponding rate constant of the phosphorescence transition. In that case the competing processes are reverse intersystem crossing to S_1 and intersystem crossing to S_0.
Multiplication of the fluorescence quantum yield with the absorption coefficient gives the fluorophores *brightness*.

2.1.5 Luminescence Quenching

Radiative decay and vibronic transitions are not the only pathways for deactivation of an excited state. By interaction with other species in the solution, the excited state can be deactivated

prior to other intrinsic deactivation processes. The excited state is *quenched*. Depending on the nature and concentration of the interacting species (quencher), different situations can be distinguished.

Dynamic Quenching

In dynamic quenching, quenching happens through collision between the quencher and the excited molecule. Such quenchers can be oxygen molecules, halides like bromine, iodine, or chloride as well as amines or electron deficient molecules like acrylamide. The quencher is not present in a big excess, however diffusion of excited luminophore and quencher to each other within the lifetime of the excited species is possible. The process of quenching is therefore diffusion controlled, and the decrease in luminescence intensity due to quenching can be described by the Stern-Volmer equation, which is dependent of the unquenched excited state lifetime τ_0, the quencher concentration $[Q]$ and the quenching rate constant k_q. The latter can be determined by time resolved experiments with and without quencher present. The luminescence quantum yield with consideration of dynamic quenching can therefore be formulated as:

$$\Phi = \frac{k_{rad}}{k_{rad} + k_{nr} + k_q[Q]} = \frac{k_{rad}}{\frac{1}{\tau_0} + k_q[Q]} \tag{2.16}$$

When the quantum yield or luminescence decay time of the unquenched luminophore ($\Phi_0 = k_{rad}\tau_0$) is set in relation to the quantum yield or luminescence decay time under influence of quenching, the Stern-Volmer equation can be derived:

$$\frac{\tau_0}{\tau} = \frac{\Phi_0}{\Phi} = \frac{I_0}{I} = 1 + k_q\tau_0[Q] = 1 + K_{SV}[Q] \tag{2.17}$$

In the above equation, K_{SV} denotes the *Stern-Volmer constant*. Experimentally, this constant can be obtained by plotting $\frac{I_0}{I}$ vs. $[Q]$. The slope of this *Stern-Volmer* plot gives K_{SV}.

Static Quenching

Static quenching can happen when a non-luminescent ground-state complex between a luminophore and a quencher is created according to $M + Q \rightleftharpoons MQ$. While in dynamic quenching the luminescence decay time is affected by the quenching process, static quenching only has influence on the luminescence intensity whereas the decay time stays unchanged. The change in luminescence intensity can be used to calculate the stability constant of the quenching-complex. For this the stability constant and the mass conservation law have to be taken into consideration.

$$K_S = \frac{[MQ]}{[M] \cdot [Q]} \tag{2.18}$$

$$[M]_0 = [M] + [MQ] \tag{2.19}$$

As the luminescence intensity is proportional to the concentration of luminophore, equation 2.20 can be derived.

$$\frac{I_0}{I} = \frac{[M]_0}{[M]} = 1 + K_S[Q] \tag{2.20}$$

This relation can be plotted similar to a Stern-Volmer plot to receive a linear dependence between intensity proportion and quencher concentration.
Only in few cases does evidence exist that such a quencher-complex is formed. Otherwise it is useful to consider an effective sphere of quenching. This model assumes that $[M^*]$ and $[Q]$ cannot diffuse within the excited state lifetime and thus quenching only takes place, if $[Q]$ already is within a certain radius of the luminophore, the resulting volume inside which quenching will be effective is called *sphere of effective quenching* or simply *active sphere*. The probability that n quencher molecules are within the active sphere of a luminophore is described by a Poisson distribution.

$$P_n = \frac{\langle n \rangle^n}{n!} e^{-\langle n \rangle} \tag{2.21}$$

In the above equation, $\langle n \rangle$ denotes the mean number of quencher molecules within the active sphere V_q (in litres). $\langle n \rangle = V_q[Q]N_A$. Therefore the probability that there is no quencher within the active sphere of a luminophore is:

$$P_0 = exp(-\langle n \rangle) = e^{(-V_q[Q]N_A)} \tag{2.22}$$

The luminescence intensity is proportional to P_0, which relates to the amount of unquenched luminophores, therefore the effect of quenching can be described as:

$$\frac{I_0}{I} = e^{(V_q[Q]N_A)} \tag{2.23}$$

This non-linear dependence of $\frac{I_0}{I}$ vs. $[Q]$ can be approximated with a linear equation at low quencher concentration when $exp(V_q[Q]N_A) \sim 1 + (V_q[Q]N_A)$. Where this approximation is valid, the volume of the active sphere can be calculated from the slope of the plot.

Photoinduced Electron Transfer (PET)

Photoinduced electron transfer is a common fluorescence quenching mechanism. PET happens when a charge transfer takes place between a donor (D) and an acceptor (A) in order to lower the energy of the donor-acceptor complex ($D-A$). The charge transfer happens after excitation because it changes the ability of a fluorophore to donate or accept electrons. Depending if the fluorophore is the donor or acceptor, we speak of oxidative or reductive electron transfer respectively, as depicted in figure 2.7.

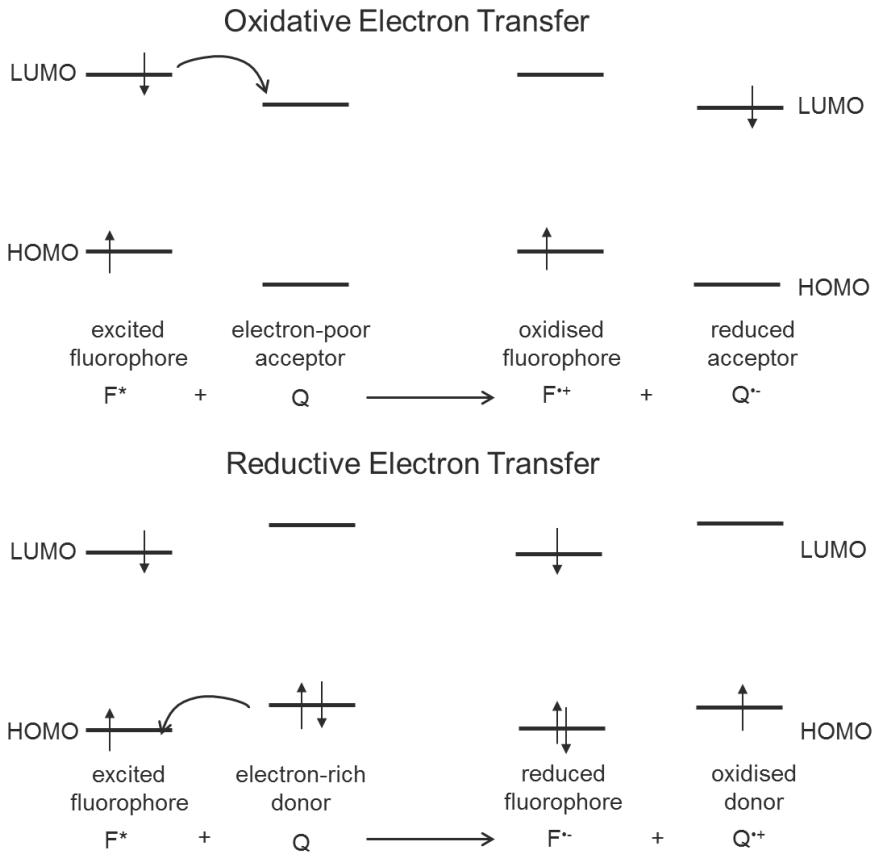

Figure 2.7: Schematic depiction of reductive and oxidative electron transfer between an excited fluorophore (F^*) and a donor or acceptor (Q)

In many cases, the quencher is a electron donor moiety within the fluorophore, like an amine or hydroxy group. This is a special case of static quenching, where $[F] = [Q]$ ([F] being the fluorophore concentration). When the fluorophore is excited, an electron from the HOMO of the PET group can be transferred to the now only half-occupied HOMO of the fluorescent moiety (e.g. an aromatic group), thus quenching the fluorescence. If the PET group is however bound to a proton or a cation in some cases, the HOMO of the PET group is lowered (the reduction potential increases) and electron transfer is not possible any more. The excited electron can now undergo non-radiative deactivation to the PET group (see figure 2.8).

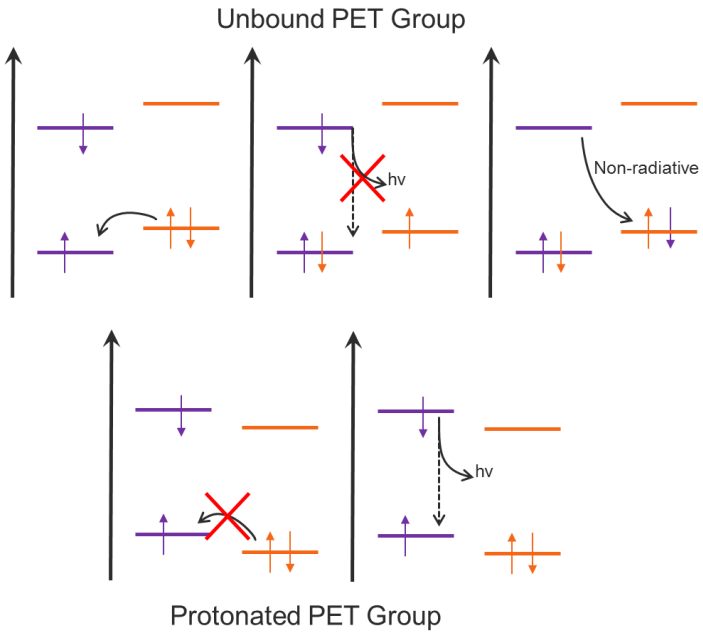

Figure 2.8: Quenching of fluorescence by intramolecular PET effect

2.1.6 Excited State Proton Exchange

This section is based on [20] and [21].

When talking about excited state reactions, such as protonation/deprotonation, only the thermally equilibrated levels of S_1 and T_1 are of interest. Similar to Kasha's rule this is due to the fact that vibrational relaxation is much faster than any protonation/deprotonation processes. Emission however, might very well be in competition with chemical processes if the lifetime of the excited state in question is long enough.

Considering a generic acid BH that is in a solution with a pH that equals the compound's pK_a, then $[BH] = [B^-]$. If the protonated form $[BH]$ absorbs at a lower wavelength (higher energy) than the deprotonated form, the excited form $[BH^*]$ will also have a higher energy than the excited deprotonated form $[B^{-*}]$. Thus deprotonation will lead to lowering of the energy level of the excited species and $[BH^*]$ will therefore become a stronger acid than $[BH]$. The reverse is the case when $[B^-]$ absorbs at a lower wavelength. $[B^{-*}]$ becomes a stronger base than $[B^-]$. While also in normal conditions, dynamic proton exchange may happen, different absorption/emission properties of ground- and excited state lead to a situation where e.g. BH is excited and the emission takes place from B^{-*} with its different spectral properties.

2.2 Chemical Sensors

This section is primarily based on references [7, 22–26] others will be cited explicitly.
In 1991, IUPAC defined chemical sensors as follows: "A chemical sensor is a device that transforms chemical information, ranging from the concentration of a specific sample component to total composition analysis, into an analytically useful signal. The chemical information, mentioned above, may originate from a chemical reaction of the analyte or from a physical property of the system investigated." [24]. An ideal sensor should be a small, robust and cheap device, able to measure an analyte selectively in a broad dynamic range with fast response time. For continuous measurements, reversibility and absence of drifts are crucial. To enable use by untrained personnel, simple handling and easy calibration or even calibrationless measurement are desirable.
A sensor is usually composed of a receptor, the recognition element interacting with sample components, and a transducer that converts the physicochemical signal generated by the receptor in an electrical signal like current or voltage that can be measured.
Classification of sensors can be according to the transducer principle, the type of stimulus (optical, acoustic, electric, magnetic, thermal,..), the mode of application (in vivo/vitro,...), the duration of use or the structure. Most commonly however, sensors are classified according to their transducer principle. This results in a the following classes of chemical sensors according to IUPAC (1991) [24]:

Optical Sensors: using absorption, scattering and reflection of light, luminescence, refractive index or optothermic effects

Electrochemical Sensors: like voltammetric, potentiometric or high temperature potentiometric sensors and field effect transistors

Electrical Sensors: measuring conductivity, permittivity, also oxide ceramic gas sensors and organic semiconductors

Mass Sensitive Sensors: for example piezoelectric devices or surface acoustic wave sensors

Magnetic Sensors: monitoring the paramagnetic properties of a gaseous analyte (e.g. oxygen)

Thermometric Sensors: for determination of reaction- or absorption heat

2.2.1 Conventional pH Sensing - the Glass Electrode

The probably most widely used device for pH measurement is the glass membrane electrode. As an ion selective, pH sensitive electrode, the glass electrode employs a potentiometric measurement principle.

A typical combination electrode, where external and internal reference electrode are implemented in on single setup, connected via a salt bridge, is shown in figure 2.9. Both reference electrodes are usually Ag/AgCl electrodes. The glass membrane is a thin layer of sodiumsilicate glass (ca. 0.4 mm thin). A potential difference across the membrane is achieved when sodium ions at the glass surface are exchanged with protons from the measurement solution.

$$SiO{-}Na^+ + H^+ \rightleftharpoons SiO{-}H^+ + Na^+_{(aq.)}$$

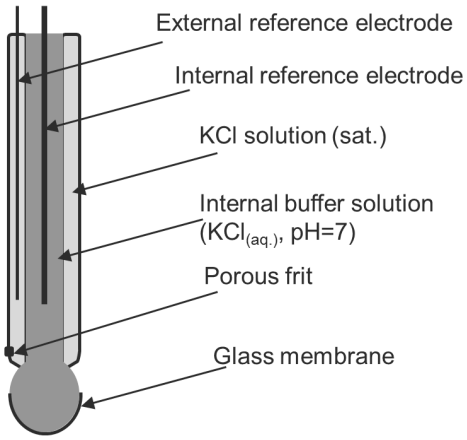

Figure 2.9: Schematic of a combination glass membrane electrode for pH measurement

There are several potentials at the various interfaces, that constitute to the overall electrode potential:

$$\underset{g_r}{Ag,AgCl} \;/\; \underset{g_j}{KCl_{(sat.)}} \;//\; \underset{g_g}{\text{measurement solution}} \;/\; \underset{g_{g'}}{\text{glass membrane}} \;/\; \underset{g_{r'}}{\text{internal buffer}} \;/\; Ag,AgCl$$

Where g_i are the galvani potentials at the interfaces, namely between the reference electrodes and surrounding buffer/solution ($g_{r/r'}$), across the salt bridge (g_j) and between the measurement solution and the glass electrode and the glass electrode and the internal buffer ($g_{g/g'}$). It can be assumed that all potentials except g_g, which depends on the pH of the measurement solution, are constant.

As a potentiometric measurement technique, the glass electrode is based on the Nernst equation:

$$E = E^{\Theta'} + \frac{0.059}{z_i} \cdot log(a_{H_3O^+}) \tag{2.24}$$

Since both the pH value and the electrode potential are logarithmic functions of H_3O^+ activity, the resulting calibration curve is linear.

$$E = E_{As} - S \cdot pH \tag{2.25}$$

In completely nernstian behaviour, the slope of the calibration curve (equation 2.25) is 0.059 mV. E_{As}, the asymmetry potential, should be zero if the pH values of the sample solution and the internal buffer solution are equal. In reality, both E_{As} and the slope deviate from this values and have to be determined experimentally by calibration.

The glass electrode is a widespread device for measuring pH conveniently over almost the entire pH range. However, there are several limitations to this format. For precise measurement, the glass electrode requires frequent calibration and optimally also pre-conditioning of the

glass membrane for one to two hours. Especially at low H_3O^+ concentration (basic media), other cations like alkali metal ions adsorb at the glass membrane and influence the membrane potential (alkali error). Furthermore, miniaturisation is not possible with glass electrodes, limiting its application to sample volumes of at least a few millilitres.

2.2.2 Optical Chemical Sensors

There are two main sensor platforms used for realisation of optical chemical sensors, the planar waveguide chemical sensor geometry and fibre optic chemical sensors. Both rely on optical phenomena including *total internal reflection* and *evanescent fields*.

Total Internal Reflection This phenomenon describes how a beam of light is reflected at the interface between two media with big difference in optical density if the angle of incidence is smaller than the critical angle for TIR, as is shown in figure 2.10.

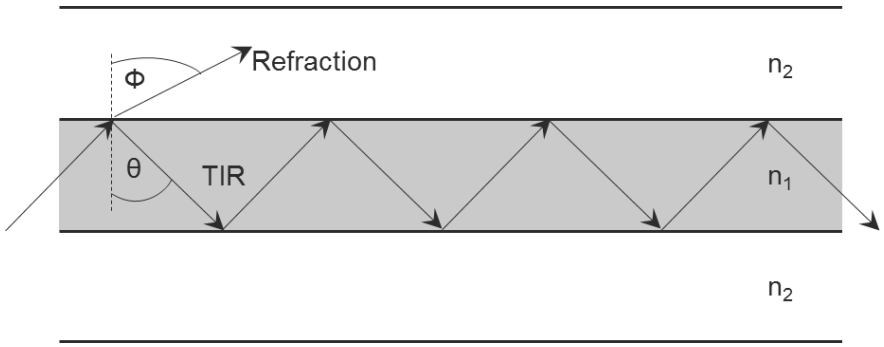

Figure 2.10: Total internal reflection of a light beam at the interface between two media with different optical densities ($n_1 > n_2$)

When the angle of refractance Φ equals $\frac{\pi}{2}$ and the angle of incidence Θ is the critical angle for TIR Θ_{crit}, the cricital angle for TIR is equal to the ratio $\frac{n_2}{n_1}$. This concludes that TIR takes place only if $\Theta_{crit} > \frac{n_2}{n_1}$.

Evanescent Field When viewing light as a wave, new properties are given to a beam of light. The light is now considered to move in different, distinguishable forms, also called *modes*. At the interface between two media of different optical density, the a so called *evanescent field* is formed. It is an electromagnetic field that is created at the point where a standing wave is created between the incident and the reflected beam.

Different materials can be used for optical components, depending on the area of application. The cheapest materials are polymers like PS, which however limit the spectral area for measurements to wavelengths above ∼450 nm because of absorption of the material in the shorter wavelength range. Regular glass can be used until 350 nm below which fused silica is the material of choice. In the IR region above 1000 nm germanium crystal materials have to be used.

Planar Waveguide Chemical Sensors [PWCS]

This relatively new sensor format is ideal for applications like flow cells or lab-on-a-chip. The basis is a planar substrate that can also double as the waveguide. Otherwise an additional layer can be deposited on that substrate to act as a waveguide. The incident light is coupled via prisms or gratings and subsequently travels through the waveguide layer which is only a few μm thick. As a result the light is reflected at the interfaces very often, giving high interaction with the sample medium. Often the interaction occurs via the evanescent field created at the reflection points. This can either occur via absorption of the energy from the evanescent field by analyte/receptor molecules or by inducing fluorescence in dye molecules on the surface. Absorption will lead to energy loss in the light beam that can be detected while in fluorescence an additional, longer wavelength component can be detected.

Fibre Optic Chemical Sensor (FOCS)

Fibre optic sensors can either work as a direct sensor, where the properties of the light are influenced by an intrinsic property of the analyte such as refractive index, or extrinsic using a mediator that changes its optical properties upon interaction with an analyte species. The second format is much more versatile and can be realised in many different configurations. The fibre is composed of a core transporting the light beam and a cladding for guaranteeing TIR and guiding of the light to the interaction site. This can be a declad site along the length of the fibre with or without an alternative active cladding. Another possibility is to replace the cladding at the fibre tip with an active cladding. Such active claddings can contain for example indicators entrapped or covalently linked to a polymer support. A fibre optic sensor containing a chemical recognition layer is also called *optode* or *optrode* in reference to electrodes as used in electrochemical sensing applications.
In direct comparison with electrochemical sensors, opt(r)odes have many advantages: No reference cell is needed, miniaturisation is easily possible to yield small, lightweight and flexible sensors, the optical signal can be transported over great distances (several 100 m) with minimal losses and is not subject to electrical influences, additionally, a fibre can transport much more information at once (light at different wavelengths), also many fibres are cheaper than other sensor platforms and are chemically inert in electrolyte solutions (no corrosion). On the other hand, several drawbacks of fibre optic sensors have to be mentioned as well. Among those are interference through ambient light, optical interferences by sensor components such as light source, connectors and the fibre itself. The stability of a fibre optic sensor also depends largely on the photostability of the used indicator.

Other Sensor Designs

Optical sensing is not limited to the two sensor platforms mentioned above. Planar sensors can be designed, where the light is not coupled in the substrate of the sensing layer. Readout of such *planar optodes* can be performed with an external readout device e.g. from above or below the sensing layer. Planar optodes can be in the form of large-area sensing layers or in the form of small sensor spots. The latter can be used in combination with an optical fibre, which in this case serves solely as a lightguide for excitation light and transferring the signal to a detector. Another, quite different sensor design is presented by nanoparticles for imaging applications. A luminescent indicator dyes is immobilised in polymer nanoparticles that are able to penetrate cell walls. With this technique, cell compartments or different conditions inside cells can be visualised.

2.2.3 Immobilisation Matrices

The receptor, i.e. the indicator has to be in contact with the sensor's transducer while being able to interact with the analyte medium. For this purpose, it is necessary to immobilise the indicator in a way that allows interaction with the analyte while showing good adhesion to the solid support (optical fibre, sensor chip, etc.). The simplest form of immobilisation is adsorption to a surface, other methods include microencapsulation between membranes, covalent attachment to the support, cross-linking to the transducer using a bifunctional agent or, most importantly, entrapment in a polymer or gel matrix [25]. The materials used for immobilisation will be discussed more closely in the following section, based on references [8, 27–31].
Materials used for indicator immobilisation include hydrophilic polymers like cellulose, dextran, polyacrylamides or polyurethanes commonly referred to as *hydrogels* that swell in water and are permeable to water soluble analytes such as protons, various ions, urea, H_2O_2 or glucose. More hydrophobic polymers like PVC, polystyrene and sol-gels may be used for sensing of gaseous compounds (NH_3, CO_2) or also e.g. for pH sensing when modified with proton carrier groups.

Sol-gels

Sol-gels are polysiloxane produced by hydrolysis and consecutive polycondensation of tetraalkoxysilanes. The nature of the resulting polymer can be strongly influenced by choosing either acidic or alkaline hydrolysis conditions. Organic modification of the silane monomers gives polymers with tunable hydrophobicity and can provide better mechanical stability as well as faster gas diffusion. These organically modified sol-gels are also called *ormosils*. Sol-gels are widely used as gas sensors, for example in oxygen sensing. In pH sensing they can be used in environments ranging from very acidic to moderately basic.

Hydrogels

Hydrogels are much more widely used in sensing of water soluble analytes. They are water insoluble polymers that show substantial swelling when in contact with an aqueous solution. This enables fast diffusion of analytes like protons or ions to the entrapped indicator. Furthermore, due to their high water content hydrogels are similar to the intracellular fluid and display high biocompatibility. Different kinds of hydrogels include:

Cellulose is an excellent material for ion sensing due to its high permeability. Apart from mechanical entrapment, the dye can also be covalently linked to the cellulose via vinylsulfonyl groups (Remazol process). Those react with cellulose under first strongly acidic, then strongly basic conditions to yield an indicator coupled to cellulose matrix [8].

Polyurethanes are a group of polymers that show good blood and tissue compatibility. Depending on the length of the alkyl chains of the diisocyanate and the diol monomers and optionally also the amount of polyol monomers for crosslinking, different properties can be achieved. The solid polymer will often retain hydrophobic and hydrophilic domains. This may lead to slight local differences in behaviour of the entrapped indicator depending on the nature of the microenvironment.

Poly(2-hydroxyethyl methacrylate) (pHEMA) is a poly(methacrylate) that is used in many medical applications (drug delivery systems, contact lenses,...) due to its high biocompatibility. Substantial swelling with water uptake of up to 67 % [30] guarantees good permeability for aqueous measurement solutions. The use of pHEMA is limited to solutions with moderate pH values, since the ester bonds are hydrolysed in alkaline media, e.g. biocomposites of pHEMA with maleic acid/anhydride and poly(caprolactone) show beginning degradation of the composites at pH 10.4 [32].

2.3 State-of-the-Art Optical pH Indicators

Colorimetric pH Indicators

Many pH indicators rely on changes in absorption properties, like aza dyes [8] or triphenylmethane dyes like bromothymol blue [33, 34] and phenol red [35] (figure 2.11). However, the use of such indicators is severely restricted to non-scattering media and measurement in cells or tissues is virtually impossible.

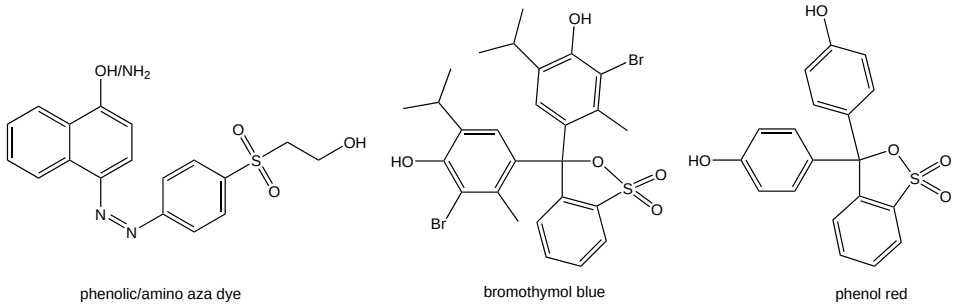

Figure 2.11: Examples for pH indicators based on changes in absorption spectra [8, 33–35]

Luminescence Intensity pH Indicators

In contrast to colorimetric pH chemosensors those exploring luminescence intensity are significantly more versatile [9]. Luminescent chemosensors have the advantages of a higher signal to noise ratio, better suitability for referencing and versatility of formats. Some representatives of fluorescence intensity probes are xanthene dyes [36, 37], derivatives of 8-hydroxypyrene-1,3,6-trisulfonic acid (HPTS) [38, 39] and naphthalimides [40, 41]. However, those dyes are all subject to different limitations (low photostability and self-quenching of xanthenes, high cross-sensitivity to ionic strength of HPTS, low molar absorption coefficients of naphthalimides). NIR excitable/emissive probes have proven to be advantageous for use in biological tissues due to high light penetration depths and low interference through light scattering or autofluorescence. One example for NIR-excitable probes are seminaphthorhodafluors (SNARF) which however suffer from poor photostability [42]. On the contrary, BF_2-chelates of aza-boradiazaindacenes show excellent photostability and also favourable modularity of the sensing properties[43–45]. Luminescence intensity itself represents a rather ambiguous parameter which is affected by intensity of excitation light, sensitivity of the photodetector, turbidity and colouration of the sample etc. Reliable sensing and imaging is therefore only possible if adequate referencing scheme is applied. So far, ratiometric two wavelength referencing and so called dual lifetime referencing (DLR) [46, 47] have been most popular. These schemes rely on addition of a reference luminophore which, for instance, has an excitation spectrum very similar to that of the indicator but a very different emission spectrum (ratiometric scheme) or a very different luminescence decay time (DLR scheme). Unfortunately, leaching or bleaching of the indicator or/and reference in these schemes severely affects the calibration. Only a few self-referenced ratiometric pH probes are known [28] (e.g. HPTS which possesses dual excitation or SNARF dyes with dual emission) but they mostly suffer from short-wavelength excitation or poor photostability. It should also be mentioned that ratiometric probes do not compensate for the variation in scattering since this effect is wavelength-dependent. For all those reasons, pH indicators that do not rely on an additional reference dye and instead enable self-referencing at only one excitation/emission wavelength are preferable.

Luminescence Decay Time pH Indicators

The measurement of luminescence decay time is free from the drawbacks mentioned above and represents a self-referenced technique. This measurement can be performed either in time domain (time correlated single photon counting, TCSPC) or in frequency domain via determination of the fluorescence phase shift Φ (as $\tau = tan\Phi/2\pi f$). The group of Lakovicz have investigated several fluorescent indicators regarding their application in decay time measurements. Measurements of SNARFs in frequency domain showed change of calibration curves and apparent pK_a values on with different excitation and detection wavelength [48]. At the same time, this might provide an opportunity for fine-tuning of the dynamic range as well as introduce increased sensitivity to fluctuations in excitation source and other instrument parameters. Furthermore they proved that the xanthene dye Oregon green 514 and the rhodol dyes Cl-NERF and DM-NERF can be applied for decay time read-out with dynamic ranges between pH 3 and 6 with lifetimes of 2.56 ns at pH 3.06 and 4.12 ns at pH 5.49 for Oregon green 514 and 1.67 ns at pH 2.0 and 3.52 ns at pH 4.28 for the Cl-NERF dye[49]. A SNAFL-dextran conjugate indicator entrapped in the distal end of an optical fibre in aqueous solution showed very slow response times (t90∼180 min). Additionally, both SNARF and SNAFL dyes show strong overlap between emission of the protonated form and excitation of the deprotonated form, resulting in efficient FRET and compromising the pH calibration. This effect partly disabled compensation of concentration dependent effects like leaching and photobleaching through the otherwise self-referenced method of decay time read-out. Another obstacle is the measurements of such short lifetimes, especially with only small differences between the protonated and the deprotonated form. In biological samples, autofluorescence background will pose a serious problem to measurement of such short lifetimes. An overview of the mentioned dyes is given in figure 2.12.

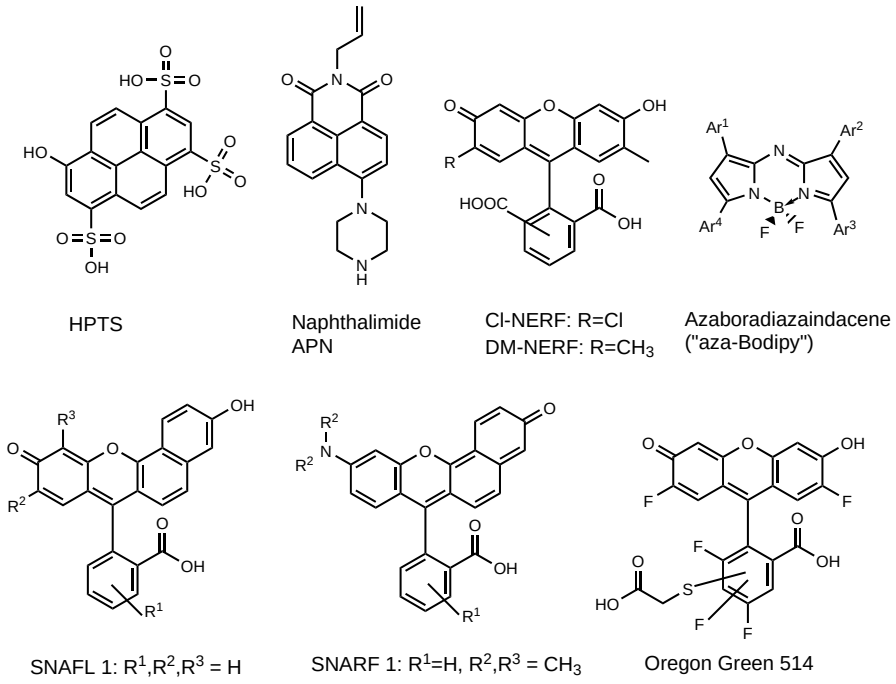

Figure 2.12: Overview of fluorescent pH indicators based on change in fluorescence emission properties (wavelength, intensity, lifetime) upon protonation/deprotonation

PET Based pH Indicators

A fluorescent decay time pH probe presented by Aigner et al. [50] relies on PET and therefore is not influenced by FRET. A perylene dye containing an alkylamine receptor which showed a decrease in decay time from 6.7 ns to 4.6 ns when going from pH 4.5 to pH 8 when the negatively-charged indicator was embedded in positively-charged Rl-100 particles. Evidently, the material shows a limited resolution. The general disadvantage of the above state-of-the-art probes is that the fluorescence decay times are rather short (particularly for the "quenched" state) which makes it very difficult to distinguish the signal of the probe from the fluorescence background. Therefore, probes with longer decay times are highly desirable. For example, a diethylaminomethylpyrene dye was developed featuring long decay times of 160 ns in its protonated form and 22 ns when deprotonated [51]. However, the short excitation wavelength and high leaching renders this dye unsuitable for practical applications. The same drawbacks can be observed with diaminomethylanthracene [52]. Acridine (UV excitation, blue emission) is also known for rather long decay times (31.6 ns protonated, 6.6 ns deprotonate) [53] and even though those high lifetime dynamics can be retained upon immobilisation in Nafion® 117 and cross-talk to chloride could be completely eliminated in this negatively charged environment, significant cross-talk to ionic strength posed a new problem in application of this indicator.

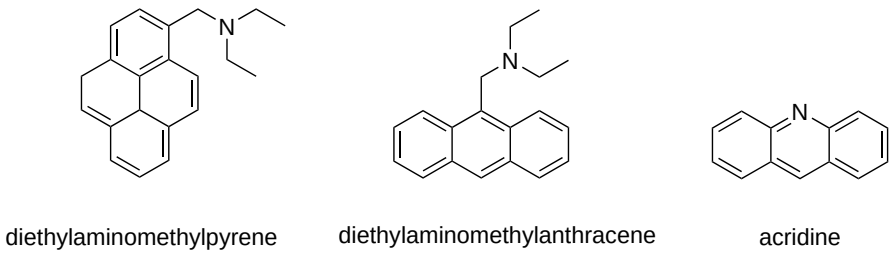

Figure 2.13: pH indicators employing photoinduced electron transfer as sensing mechanism

Quantum Dot pH Indicators

A different sensor concept explores the properties of quantum dots. They are long emitting, bright and photostable with fluorescence tunable over a wide spectral range. CdSe/ZnSQDs modified with mercaptopropionic acid showed pH sensitive emission at 535 nm with lifetimes ranging from 8.7 ns at pH 5 to 15.4 ns at pH 9 [54]. The long lifetimes made elimination of background interference possible and the sigmoidal behaviour renders them suitable for intracellular FLIM measurements for pH imaging. Other reports include Cu-doped CdZnS QDs with tunable NIR fluorescence, decay times reaching up to 1 μs and high pH sensitivity between pH 5.5 and 7.0 due to modification of the QD surface with carboxylic acid [55]. Also QD employing FRET for pH sensing have been reported [56]. Unfortunately, the quantum dots are known for their high toxicity and even if this is minimized by appropriate modifications use of toxic components during the preparation and disposal of such materials can represent a significant problem.

Metal Ligand pH Indicators

Metal-ligand complexes (e.g. those in figure 2.14) display very long lived fluorescence in the μs range, however, cross-talk to oxygen is usually proportional to decay time. Furthermore, only a few species do not suffer from severe dependency of the calibration on buffer composition and concentration [21]. When investigating the suitability of Ru(II) complexes for lifetime read-out [57], again oxygen dependence posed a problem even though a sigmoidal pH dependence with an apparent pK_a of 3.75 and protonated/deprotonated lifetimes of $\sim$1 μs and $\sim$3.3 μs could be observed. Another group found that immobilisation of a Ru(II) pH indicator in sol-gel glasses resulted in drastic decrease in intensity and lifetime between protonated and deprotonated form as well as strong dependence of response time on matrix composition [58]. As for other dyes, immobilisation of Ru(II) complexes in Nafion® membrane resulted in high cross-sensitivity to ionic strength, also the resulting response times were quite long (320 s), positive effects were a broad dynamic range and low cross-talk to oxygen. Immobilisation of another Ru(II) indicator in sol-gel strongly altered the acid-base behaviour of the dye (pK_a 5.8 vs. 2.7 in solution)[59] which can be explained by interaction of the matrix with the dye. However, even a pH insensitive dye showed limited response to pH in this matrix. Lanthanide complexes usually

do not show significant cross-talk to oxygen, investigation of Eu(III) and Tb(III) complexes showed significant decrease or increase of luminescence intensity when increasing the pH from 4 to 10 or 5 to 9 respectively [60]. Severe disadvantages are the excitation in the UV part of the spectrum, low luminescence brightness as well as moderate response times paired with conditioning of 28 days to ensure reproducible response.
Also Re(I) complexes have been investigated and long decay times (up to 1260 ns) of the acidic form was observed with no detectable luminescence in basic media [61]. They could be used in dual lifetime referenced measurements but excitation below 400 nm and low molar absorption coefficients pose serious limitations. It should also be mentioned that the decay time of the Ru(II) and lanthanide complexes is also strongly affected by temperature which introduces an additional cross-sensitivity.

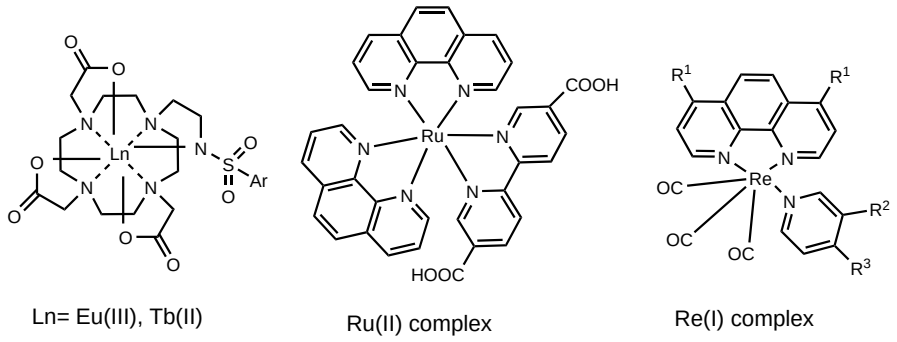

Figure 2.14: Examples of pH sensitive metal complexes

From the examples provided above it is evident, that state-of-the-art materials for optical pH sensing and imaging have many limitations since they do not combine the desirable properties. These properties include: (i) relatively long wavelength of absorption and emission; (ii) good luminescence brightness; (iii) good photostability; (iv) suitability for self-referenced lifetime read-out and (v) fluorescence decay times which are long enough to eliminate the autofluorescence from biological components and optics but short enough to avoid cross-sensitivity to oxygen. For this reason, a new class of potential pH indicators was investigated in this thesis, as will be discussed in the following section.

2.4 Triangulenium Dyes

Triangulenium dyes are constituted of highly stable carbenium ions that can be described as a triphenyl methylium ion with bridging hetero atoms in *ortho* positions to the central carbon atom that produce a rigid structure. They feature moderate absorption coefficients, excellent quantum yields and outstanding fluorescence lifetimes.
The first synthesis of a trioxotriangulenium dye, the simplest triangulenium bridged with oxygen atoms, was reported by Martin and Smith in 1963 [62]. The synthetic route involved the

synthesis of 2,6,2',6'-tetramethoxybenzophenone from *m*-dimethoxyphenol and the subsequent synthesis of tris(2,6-dimethoxyphenyl)carbinol by addition of 2,6-dimethoxyphenyllithium to the benzophenone intermediate. The triangulenium was formed by heating the tris(2,6-dimethoxyphenyl)carbinol in molten pyridinium chloride. They investigated the basicity of tris(2,6-dimethoxyphenyl)carbinol and 12c-hydroxy-4,8,12-trioxadibenzo[*c,d,m,n,*]pyrene (sesquixanthydrol). They found that conversion of the tris(2,6-dimethoxyphenyl)carbinol to the corresponding carbenium was irreversible for which reason the pK_{R+} value was only estimated to be at least 6.5. Upon addition of NaOH to an aqueous solution, they found quinonoid like infrared absorption bands, indicating that the nucleophilic attack takes place at the *ortho* position of the aryl rings instead of the central carbon, which seems to be too sterically shielded. The pK_{R+} of the trioxatriangulenium ($TOTA^+$) was found to be rather high, at 9.05. This hints at good stabilisation of the positive charge by delocalisation via mesomeric structures containing oxonium-like bonds (see figure 2.15).

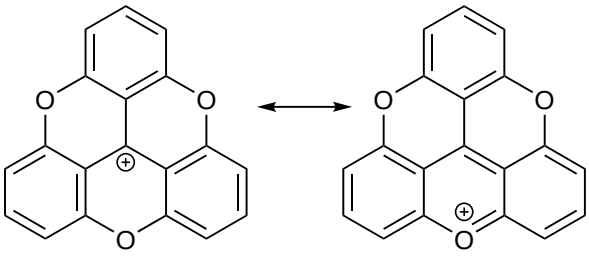

Figure 2.15: Mesomeric stabilisation of $TOTA^+$, oxonium-type bonds can occur at any oxygen atom, yielding at least 4 mesomeric structures

As could be expected from their cationic nature, triangulenes intercalate in DNA strands, preferably at G-C base pairs, and show DNA cleaving behaviour [63, 64].
Laursen and Krebs have reported synthesis not only of the trioxotriangulenium but also of triangulenium dyes in which one, two or all three oxygen bridges were substituted with nitrogen [11] (see figure 2.16). They determined that in absorption spectra the diazaoxatriangulenium ($DAOTA^+$) absorption maximum is most bathochromically shifted (560 nm) as compared to the $TOTA^+$ (430-480 nm, broad), followed by $ADOTA^+$ (azadioxatriangulenium, 540 nm) and $TATA^+$ (triazatriangulenium, 520 nm). The molar absorption coefficients found were around $15000\,L\,mol^{-1}\,cm^{-1}$ for $DAOTA^+$ and $TATA^+$ and around $9000\,L\,mol^{-1}\,cm^{-1}$ for $ADOTA^+$ and $TOTA^+$. In crystal structure analysis the triangulenium core proved to be coplanar with substituents of *N*-phenyl $ADOTA^+$ perpendicular to the coplanar system. This suggests that the phenyl substituent does not take part in charge delocalisation while the bridging nitrogen does take part in stabilisation of the conjugated system.

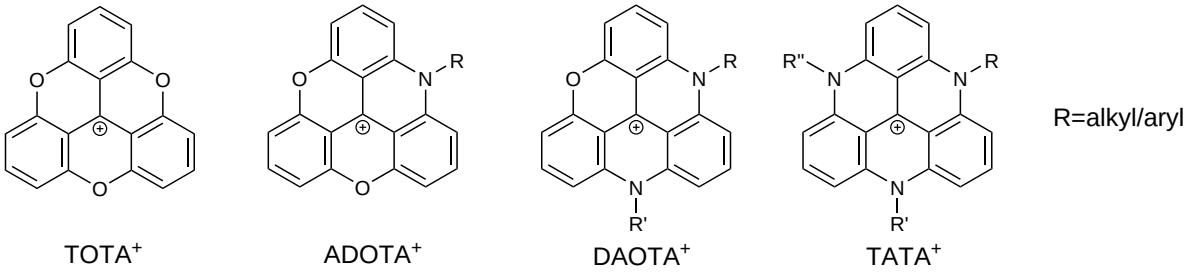

Figure 2.16: Overview of different triangulenes: $TOTA^+$=trioxatriangulenium, $ADOTA^+$=azadioxatriangulenium, $DAOTA^+$=diazaoxatriangulenium, $TATA^+$=triazatriangulenium

The addition of a dialkylamino group in *para* position at each phenyl ring (figure 2.17) results in an increase in cation stability similar to that achieved by exchanging the oxygen- with nitrogen-bridges [65]. The introduction of additional dialkylamino groups hampers the synthesis of the respective tris(dialkylamino)-azadioxatriangulenium (A-$ADOTA^+$) dye since the electron donating nature of the amino groups reduces the tendency towards nucleophilic substitution at the *ortho* positions. The synthesis of a A-$DAOTA^+$ could not be achieved at all because the acridinium structure has an even stronger electron donating character. While the molar absorption coefficients are increased by modifications with dialkylamino groups in *para* position, significant blue shift could also be observed.

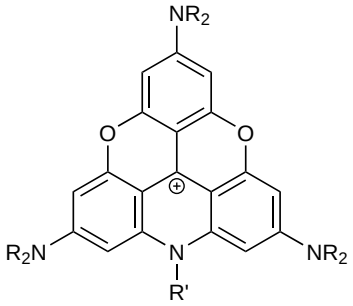

Figure 2.17: Tris(dialkylamino)-azadioxatriangulenium (A-$ADOTA^+$)

When introducing hydroxy groups in the *para* positions, a pH sensitive dye can be synthesised, able to serve as ratiometric pH indicator. While in a DMSO:H_2O mixture, four different forms and their corresponding absorption/emission spectra could be observed (figure 2.18), in aqueous solution only the cation, the neutral form and the dianion were detected [13]. The pK_a values are 3.7 and 6.7 for the protonation of the cationic form and for the formation of the dianion respectively.

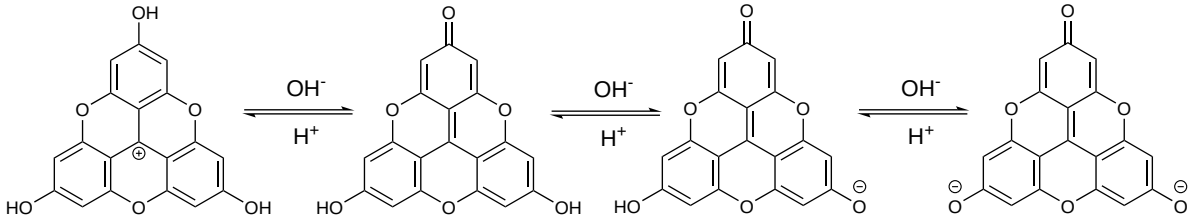

Figure 2.18: Different protonation steps of tris(hydroxy)trioxotriangulenium (H-TOTA$^+$) in DMSO with 20 mol% H_2O[13]

Again a blue shift in absorption/emission spectra was observed upon introduction of the three *p*-hydroxy groups, the absorption maxima of all forms being below 500 nm (H-TOTA$^+$ λ_{max}=416 nm, H-TOTA^0 λ_{max}=477 nm, H-TOTA$^-$ λ_{max}=485 nm, H-TOTA^{2-} λ_{max}=451 nm). No matter if the triangulenium dyes were substituted with amino- or hydroxy-groups, the quantum yields were high with 0.64 in A-ADOTA$^+$ [65] and up to 0.87 in H-TOTA$^-$ [13]. While the lifetimes were reported to be up to 21 ns and 20 ns in ADOTA$^+$ and DAOTA$^+$ respectively [66], modification with *p*-hydroxy groups lead to a significant decrease in lifetime to $\leq$4.3 ns at the most [13].

The long fluorescence decay time of ADOTA$^+$ and DAOTA$^+$ dyes have been exploited in the past for time-gated intracellular measurements, effectively eliminating the cellular autofluorescence [12, 66]. The long lifetimes also enabled measurement of intra-protein motions and rotational correlation times in proteins by synthesising conjugates via modification of ADOTA$^+$ or DAOTA$^+$ with butyric acid and subsequent esterification of the butyric acid residue with proteins such as avidin, streptavidin and IgG [66]. Protein conjugates displayed slight bathochromic shifts (4-10 nm) and partial PET-quenching of the triangulenium emission e.g. by indole moieties in tryptophan and phenol groups in tyrosine amino acids.
ADOTA$^+$ or DAOTA$^+$ labelled with hexadecyl chains were used to study the motions of fatty acids in DOPC vesicles by time-gated measurements [66]. A bathochromic shift of 5-12 nm in the absorption and emission of the dyes that was observed is probably due to counter ion effects and oriented dipoles of DOPC.
In other studies [12], time-gated measurement of cellular tissue stained with IgG labelled ADOTA$^+$ led to a fivefold improvement in signal-to-background ratio and an elimination of 96 % of the autofluorescence. FLIM images were constructed 2.5, 10, 15 and 20 ns after irradiation with a pulsed laser. After 20 ns the autofluorescence signal had been almost entirely extinguished. The ADOTA$^+$ dyes used for this experiment have been synthesised similar as in the above example by esterification of a butyric acid ADOTA$^+$ derivative with hydroxysuccinimide and labelling the obtained active ester with IgG under bicarbonate buffer conditions. Other linkers than butyric acid have also been used for creating active NHS (*N*-hydroxysuccinimide) esters of ADOTA$^+$ without significant change in the favourable long fluorescence lifetime or

high quantum yields (see figure 2.19).

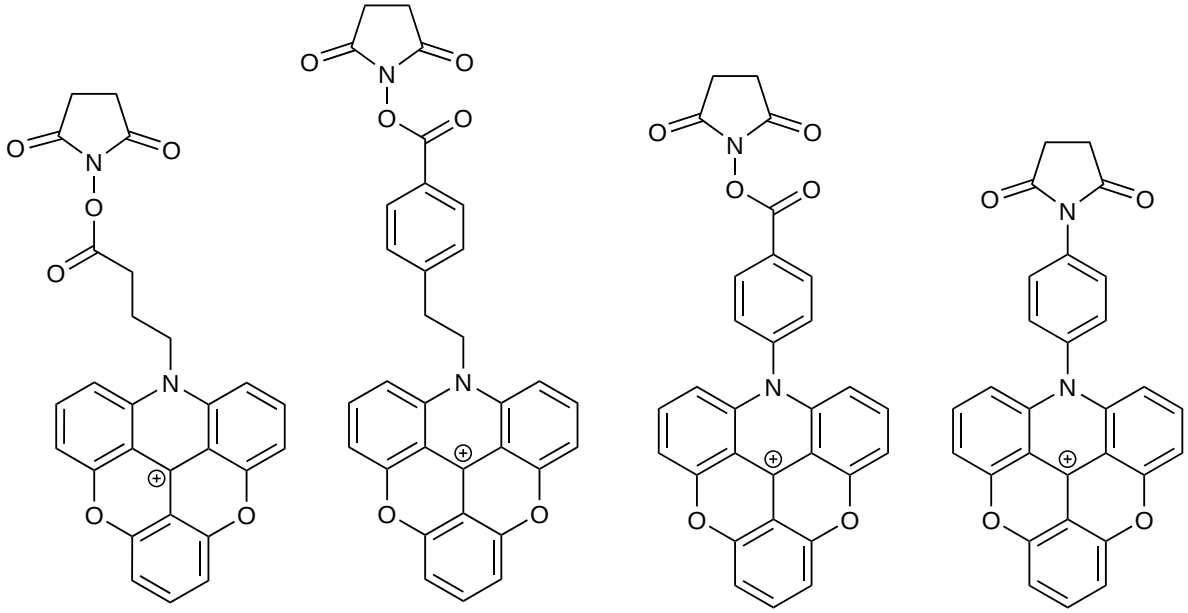

Figure 2.19: Different linkers reported for active NHS esters of ADOTA$^+$ [12, 67]

In a more recent report, intracellular imaging and pH sensitive fluorescence of diazaoxatriangulenes have been combined in one application, namely the staining of late endosomes with a pH sensitive DAOTA probe [68]. A DAOTA containing a basic nitrogen in the triangulenium core was synthesised by using an excess of hydrazine for creating the second nitrogen bridge (the first being equipped with a hexadecyl-chain, see figure 2.20). The resulting dye featured inferior quantum yields and fluorescence lifetime as compared to regular DAOTA$^+$ dyes where both nitrogen bridges carry an alkyl or aryl residue. The lifetime was reported to be in the range of 6.5-7.8 ns in CTAB nanoparticles, quantum yields were around 14-16 %. Even so, in chloroform, lifetimes of the protonated form ranges up to 15 ns with a quantum yield of 0.42. The deprotonated form has a lifetime in chloroform of 11.7 ns and a quantum yield of 0.34. Those values are close to those obtained previously for other DAOTA$^+$ dyes. The pK_a values strongly depended on the nature of the nanoparticles and the substituent at the second nitrogen bridge. In CTAB particles, pK_a values were 7.3, 7.8 and 8.4 for a hexadecyl-, phenyl- or propyl-substituted DAOTA respectively. In pluronic F-127 environment, a decrease in pK_a from hexadecyl- to propyl-substituted DAOTA of 9.5, 9.3 and 8.5 was observed.

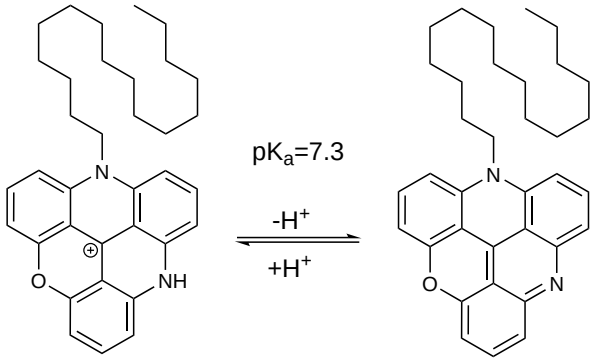

Figure 2.20: pH sensitive DAOTA$^+$ containing a basic nitrogen in the triangulenium core structure in CTAB nanoparticles [68]

In the past triangulenium dyes have been investigated from different angles, including the influence of substitution at the phenyl moieties or at the bridging nitrogen atoms, staining of cellular components, labeling of proteins and time-gated FLIM measurements. Their especially long fluorescence lifetime, high quantum yield and absorption/emission in the red part of the spectrum make them an excellent platform for sensing applications in tissues and biological samples. The pH sensitive triangulenes synthesised so far suffer severe drawbacks in terms of lifetime and quantum yield (especially in tris(dialkylamino)trioxatriangulenium [65]), also the pK$_a$ value could not be adjusted for that system. The DAOTA$^+$ dyes containing a basic nitrogen in the triangulenium core lost their favourable lifetimes and quantum yields upon immobilisation and the pK$_a$ could only be adjusted in a small range by change of substituents. So far, no attempts have been reported to exploit the favourable properties of triangulenium dyes for versatile pH sensing applications. This could be realised by equipping triangulenium dyes with PET groups, which would allow to tune the pK$_a$ value by changing the PET substituent and therefore adapt to a wide number of analytical problems. Probes which allow pH sensing via fluorescence lifetime are scarce and only a few organic indicators are known that display lifetimes comparable to those of triangulenium dyes. They present a promising candidate for self-referenced, decay time based pH sensing with increased signal quality due to autofluorescence background-elimination. With the advancement in FLIM technology, high measurement frequencies can already easily be achieved, enabling FLIM measurement of samples with decay times around 10 ns.

3 Materials and Methods

3.1 Chemicals

Unless otherwise indicated, all chemicals were used as purchased.

Table 3.1: List of used chemicals

Chemical	Supplier	CAS-Number
1,3-Dimethoxybenzene	Acros Organics	151-10-0
Bromobenzene	Acros Organics	108-86-1
Lithium	Acros Organics	7439-93-2
n-Butylamin	Sigma Aldrich	109-73-9
n-Dodecylamin	Fluka	124-22-1
1,6-Hexamethylendiamin	Fluka	124-09-4
4-Bromoaniline	Sigma Aldrich	106-40-1
2,6-Diisopropylaniline	Acros Organics	24544-04-5
N-(n-Butyl)ethylenediamine	ABCR	19522-69-1
4-(3-Aminopropyl)-morpholin	TCI	123-00-2
Potassiumhexafluorophosphate	TCI	17084-13-8
Tetrafluoroboronic Acid (50wt%)	Acros Organics	16872-11-0
Pyridine Hydrochloride	Sigma Aldrich	628-13-7
Pyridine	Sigma Aldrich	110-86-1
p-hydroxybenzylamine	Sigma Aldrich	696-60-6
3,5-Dichloro-4-hydroxyaniline	AB	5930-28-9
3-Chloro-4-hydroxxyaniline	TCI	3964-52-1
Sulfurylchloride	Sigma Aldrich	7791-25-5
HCl konz.	Roth	7647-01-0
Acetic Acid 100 %	Roth	64-19-8
2-(*N*-Morpholino)-ethanesulfonic acid (MES)	Roth	4432-31-9
3-Cyclohexylamino-1-propanesulfonic acid (CAPS)	Roth	1135-40-6
Tris(hydroxymethyl)aminomethane (TRIS)	Roth	77-86-1
Phosphoric acid 85 %	Merck	7664-38-2
Poly-(*N*-vinylpyrrolidone-co-styrene)	Sigma Aldrich	25086-29-7
Fluorescent Red	Kremer Pigments	

Continued on next page

Table 3.1 – continued from previous page

Chemical	Supplier	CAS-Number
Rhodamine 101	Fluka	64339-18-0
Macrolex®Fluorescent Red G	TER Chemicals	78985-45-2
RL-100 Polymer	Eudragit	
PMMA-MA 9:1	Polysciences	

3.2 Solvents

Water free solvents were obtained by drying over 4 Å molecular sieve.

Diethylether: was bought from *VWR Chemicals* and dried before use
Dichloromethane: was bought from *VWR Chemicals* and used as received
Dichloromethane, 100 %: was bought from *Roth* and used as received
Ethanol: was bought from *VWR Chemicals* and used as received
Ethylacetate: was bought from *VWR Chemicals* and used as received
Methanol: was bought from *VWR Chemicals* and used as received
Cyclohexane: was bought from *VWR Chemicals* and used as received
Tetrahydrofuran: was bought from *VWR Chemicals* and used as received
Tetrehydrofuran, unstabilised: was bought from *Roth* and used as received
Acetonitrile, HPLC grade: was bought from *Roth* and used as received
***N*-Methyl-2-pyrrolidone:** was bought from *Sigma Aldrich* and stored over 4 Å molecular sieve

NMR Solvents

All deuterated solvents for NMR spectroscopy were purchased from *VWR Chemicals*.
Chloroform D: +0.03 % TMS, water content < 0.01 %, 99.80 % D
Methylene chloride D2: water content < 0.01 %, 99.80 % D
Methanol D4: water content < 0.03 %, 99.80 % D
Dimethyl sulfoxide D6: +0.03 % TMS, water content < 0.02 %, 99.80 % D

3.3 Chromatography

3.3.1 Thin Layer Chromatography

For thin layer chromatography, normal phase silica gel plates from *Merck* ($silicagel 60 F_{254}$ aluminium sheets 20x20) as well as reverse phase silica gel plates from *Merck* ($silicagel 60 RP -$

$18F_{254}s$ aluminium sheets 20x20) were used. As detection methods UV – detection as well as ninhydrin staining with subsequent developing by hot air stream were used. The UV – detection was carried out at $\lambda = 254$ and 366 nm.

3.3.2 Flash Column Chromatography

For a stationary phase in preparative flash column chromatography silica gel from *Acros Organics* (silica gel, for chromatography 0.035 – 0.070 mm, 60 Å, nitrogen flushed) and Aluminium Oxide from *Merck* (Aluminium Oxide, 90 neutral, activity I)was used. The amount of stationary phase used, depending on the specific separation problem, was in general the 100 fold of the amount of crude product. Column diameter was chosen to give a filling level between 15 and 25 cm. Fraction size and eluent was chosen depending on the separation problem, typically an eluent was chosen so that the to-be-isolated compound's R_f value was < 0.2.

3.4 Photophysical Characterisation

3.4.1 Absorption Spectra

Absorption spectra were measured on a *Varian Cary 50* UV-VIS spectrometer in 10 mm precision cuvettes by *Hellma Analytics* (Type 100-OS and 104-OS). Spectra were baseline corrected using the corresponding solvent. Molar absorption coefficients were determined by preparing a stock solution of the dye in either unstabilized THF or EtOH abs. and diluting to receive an absorption between 0.05 and 0.1. Subsequently the molar absorption coefficient was calculated using Lambert-Beers law:

$$A(\lambda) = \cdot c \cdot l \cdot \varepsilon(\lambda) \tag{3.1}$$

Where A is the absorption, l the thickness of the measured solution (in this thesis always 1 cm), c the concentration of the dye solution in $mol \cdot L^{-1}$ and ε the molar absorption coefficient in $L \cdot mol^{-1}cm^{-1}$.

3.4.2 Excitation and Emission Spectra

Excitation and emission spectra were measured on a *Hitachi-F-700* fluorescence spectrophotometer or on a *FluoroLog®3* spectrofluorometer by *Horiba Scientific* equipped with a *R2658* photomultiplier by *Hamamazu* using 10 mm fluorescence cuvettes from *Hellma Analytics* (Type 100-QS).

3.4.3 Fluorescence Lifetime

Fluorescence decay times were measured on a *FluoroLog®3* spectrofluorometer by *Horiba Scientific*. Excitation was performd with a *NanoLED* (λ= 453 nm)controlled by a *Delta Hub*

module. The solutions measured were prepared so that their absorption was around 0.05, correction of prompt fluorescence was conducted using a suspension of poly(*N*-vinylpyrrolidone-*co*-styrole) in water. Processing of the data was performed using *DAS-6 Analysis* software.

3.4.4 Quantum Yield

Absolute Quantum Yield

Absolute quantum yields were determined with the *FluoroLog®3* spectrofluorometer equipped with a *Quanta-ϕ* integrating sphere. "Excitation" spectra were recorded with a neutral density 10 % Transmission filter (Actual transmission at excitation λ (520 nm) = 10.2 % (figure 9.51)).

Relative Quantum Yield

For determination of relative quantum yields, emission spectra of dye solutions with an absorption of approximately 0.05 at 520 nm were recorded on the *FluoroLog®3* spectrofluorometer and integrated. As a reference of known quantum yield, Fluorescent red 94720 from *Kremer Pigmente* (Φ=0.96 [69]) was used. Relative quantum yields were calculated according to 3.2[70].

$$\Phi_x = \Phi_R \cdot \frac{B_R}{B_x} \cdot \frac{E_x}{E_R} \cdot \frac{n_x^2}{n_R^2} \tag{3.2}$$

Where B is the fraction of incident light absorbed and correlates to the absorption A as follows: $B = (1 - 10^{-A})$. Φ is the quantum yield, E the integrated area under the corrected emission spectrum and n is the refractive index of the reference solution. Subscripts x and R refer to the investigated compound and the reference compound, respectively.

3.4.5 pH Calibration

Fluorescence Intensity Calibration

Measurement of pH dependence of fluorescence intensity was performed on *FLUOstar Optima* from *BMG Labtech*. 96 well F-bottom polystyrene clear microtiterplates from *Greiner®* were used for fluorescence intensity measurements. For excitation and emission, bandpass filters with 485 nm and 610 nm maximal transmission respectively, were used. The measurements were conducted at 25°C.

Fluorescence Decay Time Calibration

To determine the pH dependence of the fluorescence decay time, the sensor layers were placed in a buffer filled fluorescence cuvette in an angle of 45 degrees to both excitation source and detector. Prompt was measured with the same settings as in section 3.4.3.
Decay time pH calibration in solution was conducted in a mixture of ethanolic dyes solution and buffer 1+1. Measurement temperature was set using a *Julabo F12 - ED* refrigerated & heating

circulator combined with a *Cary SPV - 1X0 Single Cell Peltier Accessory* peltier element from *Varian* for fine tuning of the temperature.

3.4.6 Photostability

Photobleaching behaviour was investigated by illuminating an ethanolic solution of the dye under investigation with an array of twelve high power LEDs (*LT-2031*) form *LED-TECH.DE*. The emission maximum for illumination was 528 nm and the applied voltage and current were 39 V and 900 mA respectively, the light was focused onto the center of the test solution via a glass lens. Absorption spectra of the dye solution were acquired every 5 minutes and the intensity of the LED was determined at the same intervals using a *LI-250A Light Meter* from *LI-COR Bieosciences*.

3.5 Leaching Tests

To investigate leaching of the dyes from the hydrogel matices, the absorption of the sensor layer at 560 nm was continuously measured with a *Varian Cary 50 conc.* UV-VIS spectrometer while the foil was immersed in a flow cell with a buffer flow speed of approx. 10 mL/h. In regular time intervals the buffer was changed from a low to a higher pH value and back. For this purpose the flow was increased and the cell was first rinsed with deionised water before the next buffer was introduced to the system. This way the leaching behaviour of both, the protonated and deprotonated form could be monitored.

3.6 Nanoparticle Preparation

Nanoparticles were prepared by dissolving the polymer and dye in the respective solvent, so that the concentration of polymer in the solvent was 2 mg/mL. Precipitation of nanoparticles was achieved by addition of the five- to sixfold volume of distilled water to the polymer/dye solution. The organic solvent was evaporated and the dispersion concentrated to a concentration of about 100 mg/100 mL H_2O.[71, 72]

3.7 Structural and Chemical Characterization

3.7.1 Nuclear Magnetic Resonance Spectroscopy

1H, Cosy, APT and HSQC NMR spectra were recorded on a Bruker AVANCE III equipped with an autosampler (300.36 MHz-1H-NMR, 75.53 MHz-13C-NMR). The chemical shifts were reported using the residual signal of the used solvent as an internal standard. All of the given APT NMR spectra were proton decoupled. For data analysis MNova from *Mesrtelab Resarch* was used.

The measured signals were reported as follows: chemical shift in ppm (parts per million), multiplicity, coupling constant J in Hz, number of protons.

3.7.2 High Resolution Mass Spectrometry with MALDI-TOF

Mass spectrometry was performed in a positive reflector on a *Micromass TofSpec 2E Time-of-Flight Mass Spectrometer* (Bruker Ultraflex Extreme)by the group of Prof. Robert Saf at the Institute for Chemistry and Technology of Materials at the TU Graz. External calibration was performed with poly(ethyleneglycol) standards in a suitable mass range. As matrix either dithranol or α-cyano-4-hydrocinnamic acid were used. Data analysis was conducted with *MassLynx™V4.1* software from *Waters*.

4 Experimental

4.1 Synthesis

The synthetic work consisted of two main parts. The first constituted of the synthesis of tris-(2,6-dimethoxyphenyl)methanol via 2,2',6,6'-tetramethoxybenzophenone as educt for further reactions according to literature reports [62, 73]. This first step was identical for the synthesis of all dyes and performed in bigger batches. The educt was then via substitution/ring closing transformed to different fluorescent triangulenium dyes based on the reports of Laursen et al. [11, 65, 74]

4.1.1 Synthesis of 2,2',6,6'-Tetramethoxybenzophenone

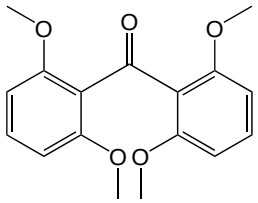

(a)

Figure 4.1: Structure of 2,2',6,6'-tetramethoxybenzophenone

3.1 g Li (450 mmol) were added to a 250 mL Schlenk flask containing 100 mL dry Et_2O. 21 mL bromobenzene (0.46 eq., 207 mmol) were added in three turns using an Ar flushed syringe. Strong heat development and yellow colouring of the liquid phase was observed. When all Li metal had reacted, 19 mL 1,3-dimethoxybenzene (66 mmol) were slowly added with an Ar flushed syringe. After the heat development had stopped, the reaction was stirred overnight at room temperature. After 16 h CO_2 was passed through the reaction mixture upon which a white precipitate formed. The reaction mixture was then hydrolyzed by addition of 50 mL of H_2O and filtered. ^{1}H NMR spectroscopy of the 2,2',6,6'-tetramethoxybenzophenone intermediate was performed and showed that the product was sufficiently clean to use for further synthesis without recrystallization.

Yield: 12.9 g, 59 %

^{1}H NMR(300 MHz, $CDCl_3$): $\delta = 7.42 - 7.13$ (m, 3 H, arom. C-H), 6.55 (d, $J = 8.4$ Hz, 4 H, arom. C-H), 3.71 (s, 12 H, O-CH_3)
See figure 9.1 on page 95

4.1.2 Synthesis of Tris(2,6-dimethoxyphenyl)methanol

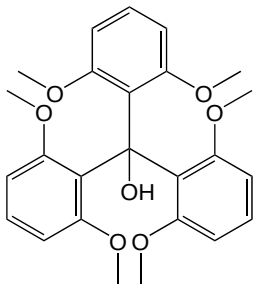

(b)

Figure 4.2: Structure of tris(2,6-dimethoxyphenyl)methanol

To convert 2,2',6,6'-tetramethoxybenzophenone (**(a)**) to tris(2,6-dimethoxyphenyl)carbinol (**(b)**), at first phenyllithium in 40 mL Et_2O was again produced (0.775 g = 111 mmol Li; 4.8 mL = 0.41 eq. = 46 mmol bromobenzene) and 1,3-dimethoxybenzene (4.6 mL, 0.31 eq., 35 mmol) was added and the reaction mixture stirred overnight, after which 5.016 g (0.15 eq., 17 mmol) of intermediate **(a)** was dissolved in 50 mL hot toluene and added to the reaction mixture under Ar. The mixture was refluxed for two days and then poured into 150 mL H_2O. The organic phase was extracted using DCM and the solvent was evaporated. The oily black product was dissolved in warm toluene and precipitated by addition of CH. The precipitate was separated by filtration and the filtrate was concentrated and the procedure repeated twice more so that the product was precipitated and separated by filtration from the mother liquor three times. The resulting grey-black solid is soluble in EtOH and turns intense purple upon acidification. Yield: 3.52 g, 47;%

^{1}H NMR (300 MHz, $CDCl_3$): $\delta = 7.04$ (t, $J = 8.2$ Hz, 3 H, arom. C-H), 6.49 (d, $J = 8.2$ Hz, 6 H, arom. C-H), 3.44 (s, 17 H, O-CH_3)
See figure 9.3 on page 96
APT-NMR (76 MHz, $CDCl_3$): $\delta = 158.71$, 127.43, 126.33, 106.99, 106.23, 77.16, 56.43
See figure 9.5 on page 97

4.1.3 Synthesis of TOTA$^+$

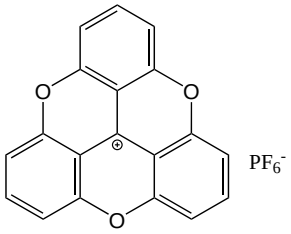

Figure 4.3: Structures of tiroxotriangulenium

The synthesis of the TOTA$^+$PF$_6^-$ dye was conducted similar to the description in [75]. 236.9 mg (0.54 mmol) of intermediate **(b)** were dissolved in 4 mL of pyridine and added to a 25 mL vial containing approximately 4 g molten pyridine hydrochloride. The mixture was heated to 180°C and stirred until the colour turned red. Due to the high melting point solvent (PyHCl), TLC reaction control was challenging. After the TLC showed no residue of the purple intermediate **(b)**, the heating was removed and the cooled mixture and rinsed from the vial with water and precipitated by pouring into 25 mL of a 0.2 M aqueous KPF_6 solution (ca. 10 eq.). The yellow precipitate was separated by filtration and washed with CH before it was dried under vacuum in a drying cabinet.

Yield: 123 mg, 53 %

^{1}H NMR (300 MHz, DMSO-d_6): $\delta = 8.56$ (t, $J = 8.5$ Hz, 3 H), 7.97 (d, $J = 8.5$ Hz, 6 H)
See figure 9.7 on page 98
APT-NMR (76 MHz, $CDCl_3$): $\delta = 152.99$, 143.49, 112.49, 106.29, 39.52
See figure 9.9 on page 99

4.1.4 Synthesis of *N*-Butyl ADOTA$^+$ (Dye (1))

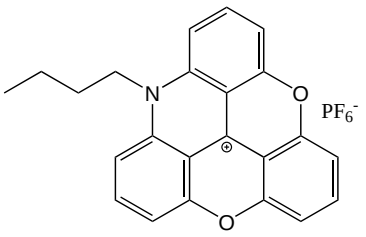

Figure 4.4: Structure of *N*-Butyl ADOTA$^+$ PF$_6^-$

The synthesis procedure as described in [11] was experimentally tested by producing an azadioxatriangulenium dye substituted with a butyl chain. For this purpose, 100 mg (0.23 mmol) of **(b)**

were dissolved in 5 mL EtOH and 85 µL aqueous HBF_4 (50 wt%, 3 eq., 0.68 mmol). The tris(2,6-dimethoxyphenyl)carbenium intermediate was precipitated from the intense purple solution by addition of 10 mL CH and the precipitate was collected by filtration, upon which it appeared green-gold glittering. It was dissolved in ca. 15 mL acetonitrile and 60 µL *N*-butylamine (2.7 eq., 0.61 mmol) were added. The solution immediately turned bright red. The reaction was stirred at room temperature overnight. When no purple tris(2,6-dimethoxyphenyl)carbenium was detected by TLC anymore, the reaction solution was poured into 25 mL 0.2 M aqueous KPF_6 and the red precipitate was filtered off.
The precipitate was dissolved in a few millilitres pyridine and added to a 25 mL vial containing ca. 2 g molten PyHCl and then heated to 180°C for ca 1 h. After cooling the mixture was again dispersed in H_2O and precipitated by adding it to ca. 25 mL 0.2 M KPF_6 solution. The red precipitate was filtered off and dried. Even when still hot, the $ADOTA^+$ dye showed fluorescence when illuminating with 366 nm UV light.

Yield: 63 mg, 57 %

^{1}H NMR (300 MHz, DMSO-d_6): $\delta = 8.40$ (t, $J = 8.5$ Hz, 2 H, arom. C-H), 8.16 (t, $J = 8.5$ Hz, 1 H, arom. C-H), 8.04 (d, $J = 9.0$ Hz, 2H, arom. C-H), 7.63 (dd, $J = 20.2$, 8.3 Hz, 4 H, arom. C-H), 4.85 (t, $J = 7.7$ Hz, 2 H, N-CH_2), 1.91 – 1.80 (m, 3 H, aliphat. CH_2), 1.58 (q, $J = 7.4$ Hz, 2 H, aliphat. CH_2), 1.00 (t, $J = 7.3$ Hz, 3 H, CH_3)
See figure 9.11 on page 100
APT-NMR (76 MHz, $CDCl_3$): $\delta = 152.50$, 151.72, 140.72, 139.98, 139.65, 111.47, 110.57, 109.07, 108.58, 47.89, 39.52, 28.53, 19.23, 13.73
See figure 9.13 on page 101

4.1.5 Synthesis of *N*-Butyl $ADOTA^+$ from $TOTA^+$

To explore the possibility of exchanging the oxygen bridges in $TOTA^+$ with primary amines, 319.5 mg $TOTA^+$ (0.045 mmol) were dissolved in 3 mL NMP and 300 µL *N*-butylamine (3.0 mmol, 66 eq.) was added. The reaction was stirred overnight at 150°C under nitrogen. Then the reaction mixture was poured into 10 mL 0.2 M KPF_6 and the red precipitate collected by filtration.

Yield: 191 mg, 53 %

4.1.6 Synthesis of Di(*N*-dodecyl) DAOTA$^+$ (Dye (2))

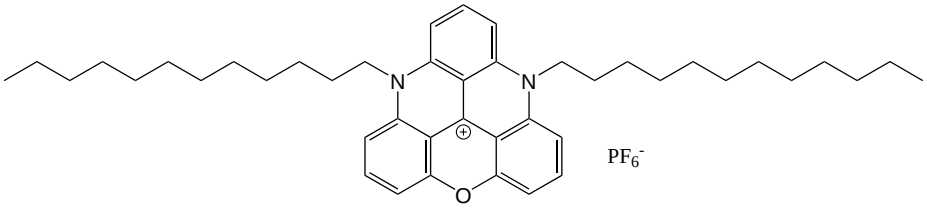

Figure 4.5: Structure of Di-*N*-dodecyl DAOTA$^+$

101.0 mg (0.23 mmol) of intermediate **(b)** were dissolved in 10 mL EtOH, acidified with 85 µL 50 wt.% $HBF_{4aq.}$ and precipitated by addition of 20 mL CH. The tris(2,6-dimethoxyphenyl)carbenium intermediate was separated by filtration, dissolved in 8 mL NMP and added to a Schlenk tube under Ar. 985 mg (23 eq., 5.31 mmol) of dodecylamine were dissolved in 6 mL NMP and added to the Schlenk tube which was heated to 180°C. The reaction turned red almost immediately. Reaction control was conducted with TLC (eluant: DCM+MeOH 75+5) on silica. When only one greenish-blue spot could be detected, the reaction mixture was cooled to room temperature and poured into 25 mL 0.2 M aqueous KPF_6 solution. The precipitate was collected by filtration and the filtrate extracted with DCM. The solvent in the organic phase was removed on the rotary evaporator and the extracted DAOTA$^+$ dried together with the precipitate in a vacuum drying cabinet.

Yield: 96 mg, 55 %

^{1}H NMR (300 MHz, $CDCl_3$): $\delta = 8.25$ (t, $J = 8.5$ Hz, 1 H, aromat. C-H), 8.04 (t, $J = 8.5$ Hz, 2 H, aromat. C-H), 7.38 (dd, $J = 18.5$, 8.7 Hz, 5 H, aromat. C-H), 7.30 – 7.18 (m, 52 H, aromat. C-H, $CHCl_3$), 4.59 – 4.34 (m, 3 H, N-CH_2), 1.99 – 1.82 (m, 3 H, aliphat. CH_2), 1.65 – 1.52 (m, 4 H, aliphat. CH_2), 1.43 (s, 2 H, aliphat. CH_2), 1.26 (s, 57 H, aliphat. CH_2, H-grease), 0.87 (t, $J = 6.0$ Hz, 16 H, CH_3, H-grease)
See figure 9.15 on page 102
MALDI-TOF: *m/z*: [M$^+$] calculated: 619.46 found: 619.47
See figure 9.40 on page 116

4.1.7 Attempted Synthesis of Di-*N*-(2,6-diisopropylphenyl) DAOTA$^+$

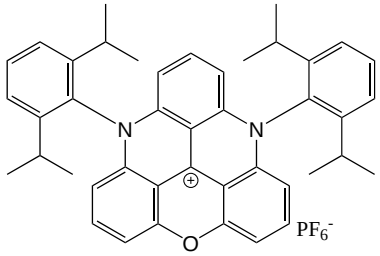

Figure 4.6: Structure of Di-*N*-(2,6-diisopropylphenyl) DAOTA$^+$

101.0 mg (0.23 mmol) of **(b)** were dissolved in 10 mL EtOH, acidified with 85 µL 50 wt.% $HBF_{4aq.}$ and precipitated by addition of 20 mL CH. The tris(2,6-dimethoxyphenyl)carbenium intermediate was collected by filtration, dissolved in 8 mL NMP and added to a Schlenk tube under Ar. 1 mL of 2,6-diisopropylaniline (23 eq., 5.30 mmol) were added and the reaction mixture heated to 150°C and stirred overnight. When TLC showed first degradation products while conversion was still incomplete, the reaction was precipitated in 25 mL 0.2 M aqueous KPF_6 and the intermediate separated by filtration and dissolved in a few millilitres of pyridine before adding it to 3 g molten PyHCl. After stirring for 1 h at 180°C the reaction product was precipitated again as usual in 25 mL 0.2 M aqueous KPF_6. The precipitate was separated via filtration and dried under vacuum.
TLC and NMR showed that the reaction had been unsuccessful and no di- or even mono-substituted triangulenium dye could be synthesised, but only TOTA$^+$ and degradation products were found.

4.1.8 Attempted Synthesis of *N*-dodecyl-*N*-(4-bromophenyl) DAOTA$^+$

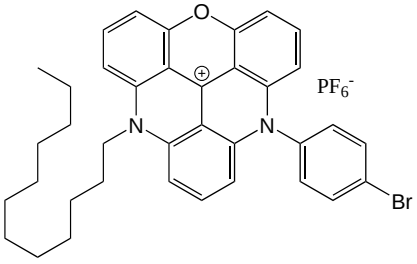

Figure 4.7: Structure of *N*-(4-Bromophenyl)-*N*-dodecyl DAOTA

The tris(2,6-dimethoxyphenyl)carbenium intermediate was synthesised as usual by acidifying an EtOH solution of 64.1 mg (0.15 mmol) **(b)** with 50 µL 50 wt.% $HBF_{4aq.}$ and precipitating

with CH. It was then dissolved in 5 mL NMP and 57 mg 4-bromoaniline were added (2.3 eq., 0.33 mmol). The reaction mixture was heated to 60°C under Ar and stirred overnight.
When TLCs (on silica in EOAc+CH 1+2) showed no further conversion of the educts but beginning of degradation, 234.7 mg dodecylamine (8.7 eq., 1.27 mmol) were added and the reaction heated to 150°C overnight. Then the deep-red solution was precipitated in 20 mL of 0.2 M aqueous KPF_6 and filtered off. The red solid was then dissolved in 3 mL pyridine and added to 3 g molten PyHCl. The melt was heated to 180°C for one hour and after cooling precipitated in 20 mL of 0.2 M aqueous KPF_6. The solid was reddish-brown with some black, insoluble granulates (probably decomposed bromoaniline). Illumination with UV ligth (366 nm) showed no fluorescence of a solution of the product in acetone. TLC showed many different components, none of which displayed fluorescence under UV illumination, therefore it can be concluded that the desired product was not formed.

4.1.9 Attempted Synthesis of *N*-Dodecyl-*N*-(4-bromophenyl) DAOTA$^+$ from TOTA$^+$

As an alternative route it was attempted to synthesize the dodecyl- and bromophenyl-disubstituted DAOTA$^+$ by exchanging the oxygen bridges in completely ring closed TOTA$^+$ dyes with the respective amines. For this purpose, 51.1 mg TOTA$^+$PF$_6^-$ (0.12 mmol)were dissolved in NMP and after addition of 27.4 mg 4-bromoaniline (1.4 eq., 0.16 mmol) the reaction mixture was heated to 180°C. When TLC on silica showed orange spots at $R_f = 0.07$ (EOAc+CH 2+1), 304.8 mg dodecylamine (14 eq., 1.64 mmol) were added and the reaction was stirred overnight at 120°C.
The next morning the reaction mixture was poured into 15 mL of 0.2 M aqueous KPF_6 and the precipitate separated by filtration. A solution of the product in acetone showed no fluorescence, TLC revealed many different components, non of which were fluorescent under UV illumination. Therefore it can be concluded, that this reaction pathway is no viable alternative for synthesis of hetero-substituted DAOTA$^+$ dyes.

4.1.10 Synthesis of *N*-(6-Aminohexyl)-*N*-dodecyl DAOTA$^+$ (Dye (3))

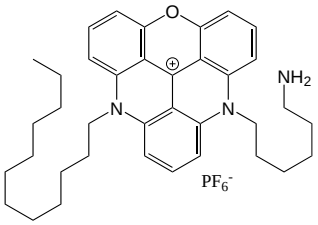

Figure 4.8: Structure of *N*-(Aminohexyl)-*N*-dodecyl DAOTA$^+$

103 mg of intermediate **(b)** (0.23 mmol) were dissolved in 10 mL EtOH, acidified with 85 µL 50 wt.% $HBF_{4aq.}$ and precipitated by addition of 20 mL CH. The precipitate was dissolved in a few millilitres acetonitrile and 86.7 mg dodecylamine (2 eq., 0.47 mmol) were added upon which the reaction mixture turned orange-red immediately. The reaction was stirred overnight at room temperature and then precipitated in 25 mL 0.2 M aqueous KPF_6. The filtrate was concentrated on a rotary evaporator to precipitate remaining acridinium and filtered again. Then the nitrogen bridged intermediate was dissolved in 6 mL NMP in a Schlenk tube under Ar and 271.9 mg hexamethylenediamine (10 eq., 2.34 mmol) were added. The reaction mixture was stirred at 100°C overnight. The solution turned green soon after adding the second amine and an absorption spectrum showed presence of the doubly nitrogen bridged intermediate. The reaction was again precipitated in 25 mL 0.2 M aqueous KPF_6 solution. The green-blue solid was dissolved in 3 mL pyridine and added to a vial containing 3 g molten PyHCl, which was then heated to 180°C for 1 h. The cooled, red reaction product in solid PyHCl was dissolved in H_2O and precipitated in 0.2 M aqueous KPF_6. TLC showed a product mixture, containing also Di-*N*-dodecyl $DAOTA^+$ and $TOTA^+$.
The product was purified by flash column chromatography on silica using a eluent mixture of DCM and MeOH (1-10 %). The product fraction was then dissolved in clean DCM and precipitated by addition of CH. A light green solution (doubly nitrogen bridged intermediate) was separated from the red precipitate via centrifugation. This was repeated several times until the solution remained colourless. The product was again dissolved in clean DCM and extracted with 0.001 M HCl in order to remove excess amines that could not be separated via column chromatography. Afterwards the organic phase was dried over Na_2SO_4. The red product showed quenching of fluorescence when its solution was basified. As can be seen from the mass spectrum, apart from the desired product also significant amounts of di-*N*-dodecyl $DAOTA^+$ (m/z=620.45) and another yet unidentified side product with a mass of m/z =690.47 are present.

Crude yield: 73 mg, 45 %

^{1}H NMR (300 MHz, $CDCl_3$): $\delta = 8.34$ (t, $J = 7.0$ Hz, 4 H), 8.07 (t, $J = 7.5$ Hz, 5 H), 7.97 (t, $J = 8.0$ Hz, 8 H), 7.71 – 7.46 (m, 12 H), 6.99 (t, $J = 7.6$ Hz, 15 H), 4.39 (d, $J = 39.5$ Hz, 2 H), 3.16 (s, 13 H), 1.83 (d, $J = 52.0$ Hz, 34 H), 1.55 (s, 1 H), 1.21 (s, 62 H), 0.84 (t, $J = 6.1$ Hz, 33 H)
See figure 9.17 on page 103
MALDI-TOF: m/z: [M^+] calculated: 550.38 found: 550.40, 620.45, 690.47
See figure 9.42 on page 118

4.1.11 Attempted Synthesis of *N*-(3-Morpholinopropyl)-*N*-dodecyl DAOTA$^+$ and *N*-(*N*-Butylethyleneamine)-*N*-dodecyl DAOTA$^+$

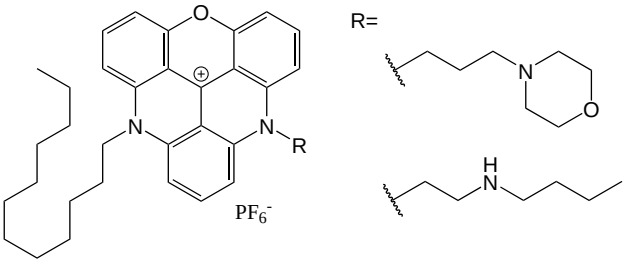

Figure 4.9: Structure of *N*-(3-Morpholinopropyl)-*N*-dodecyl DAOTA$^+$ and *N*-(*N*-Butylethyleneamine)-*N*-dodecyl DAOTA$^+$

Analogously to previous syntheses, tris(2,6-dimethoxyphenyl)carbenium intermediate was prepared from 305.2 mg **(b)** (0.69 mmol). The dodecylamine-substituted intermediate was synthesised by adding 282 mg (2 eq., 1.52 mmol) of dodecylamine to tris(2,6-dimethoxyphenyl)carbenium dissolved in acetonitrile (40 mL). As expected, colour change from deep purple to orange-red occurred immediately. After three hours no tris(2,6-dimethoxyphenyl)carbenium could be detected on the TLC anymore so the dodecylamine-substituted intermediate was precipitated from the solution by pouring into 50 mL aqueous KPF_6 (0.2 M). The nitrogen-bridged, dodecyl chain bearing intermediate was dissolved in 16 mL NMP and the solution distributed to 2 different Schlenk tubes under Ar. To one solution, 485 µL of *N*-butylethylenediamine (10 eq., 3.49 mmol) and to the other 505 µL of *N*-3-aminopropylmorpholine (10 eq., 3.47 mmol) were added. After 1 h of stirring at 80°C only little conversion had occurred, so another 200 µL portion of each amine were added to the corresponding reaction. After another hour both reactions were quenched by pouring into 25 mL of 0.2 M aqueous KPF_6. The respective precipitates were dissolved in few millilitres of pyridine and transferred to vials containing 4 g molten PyHCl each. After stirring at 180°C for about one hour, the product was again washed from the vials with H_2O and precipitated in aqueous KPF_6.
Because TLC showed major impurities and product spots could not clearly be identified, both reaction products were purified twice with flash column chromatography and afterwards fat was removed by dissolving in clean DCM and precipitating with CH several times.

NMR was not conclusive, when changing the pH fluorescence intensity did not change significantly. MS analysis showed that in fact no PET-group-modified DAOTA was synthesised but *N*-dodecyl ADOTA$^+$.
MALDI-TOF:
Morpholino-DAOTA: *m/z*: [M$^+$] calculated: 578.37 found: 452.23 (*N*-dodecyl ADOTA)
See figure 9.48 on page 125
Butyl-DAOTA: *m/z*: [M$^+$] calculated: 550.38 found: 452.27 (*N*-dodecyl ADOTA)

See figure 9.49 on page 126

4.1.12 Alternative Approach to Synthesising *N*-(3-Morpholinopropyl)-*N*-dodecyl DAOTA$^+$

The synthesis of a DAOTA$^+$ substituted with a morpholino PET group was attempted in reverse order, first substituting with *N*-3-aminopropylmorpholine and then with the dodecylamine. For the reaction 207.7 mg of intermediate **(b)** (0.47 mmol) were acidified with 170 µL of 50 wt.% aqueous HBF_4 and the tris(2,6-dimethoxyphenyl)carbenium precipitated from the ethanolic solution with CH. The tris(2,6-dimethoxyphenyl)carbenium was dissolved in acetonitrile and 70 µL of *N*-3-aminopropylmorpholine (1 eq., 0.48 mmol) were added. When the colour did not change from purple to red, 70 µL *N*-3-aminopropylmorpholine were added twice more (3 eq. in total) until the solution had a deep orange-red colour. It was precipitated as usual in 50 mL 0.2 M aqueous KPF_6 solution and the intermediate collected by filtration. The nitrogen bridged, propylmorpholino-group bearing intermediate was dissolved in a few millilitres of NMP in a Schlenk tube under N_2 and 936.1 mg dodecylamine (11 eq., 5.05 mmol) were added, then it was stirred at 95°C until TLC showed no more conversion. The product was precipitated again, dissolved in a few millilitres of pyridine, added to a few grams of molten PyHCl and stirred at 180°C for 1 h before it was precipitated again. Purification was done with three consecutive flash column chromatographies, first on silica then twice on AlOx, followed by multiple precipitations of the dye from DCM by addition of CH. ^{1}H-NMR and MS showed clean *N*-(3-Morpholinopropyl)-*N*-dodecyl DAOTA$^+$

Yield: 34 mg, 10 %

^{1}H NMR (300 MHz, CD_2Cl_2): $\delta = 8.28$ (t, 1H, aromat. C-H), 8.09 (t, 2H, aromat. C-H), 7.84 (d, $J = 4.7$ Hz, 1H, aromat. C-H), 7.78 – 7.67 (m, 1H, aromat. C-H), 7.49 (d, $J = 8.3$ Hz, 1H, aromat. C-H), 7.40 (d, $J = 7.6$ Hz, 1H, aromat. C-H), 7.27 (d, $J = 4.3$ Hz, 2H, aromat. C-H), 4.73 (s, 2H, N-CH_2), 4.59 – 4.39 (m, 2H, N-CH_2), 3.77 (s, 3H, morpholino N-CH_2), 3.70 – 3.48 (m, 3H, propyl N-CH_2), 2.65 (d, $J = 35.1$ Hz, 4H, morpholino N-CH_2), 2.13 (d, $J = 10.5$ Hz, 2H, propyl CH_2), 1.93 (s, 2H, aliphat. CH_2), 1.61 (s, 2H, aliphat. CH_2), 1.42 (s, 3H, aliphat. CH_2), 1.26 (s, 10H, aliphat. CH_2), 0.86 (d, $J = 6.7$ Hz, 3H, CH_3)
See figure 9.26 on page 108
APT-NMR (76 MHz, CD_2Cl_2): $\delta = 153.16$, 141.63, 141.30, 140.54, 140.39, 140.14, 139.28, 112.01, 110.23, 109.59, 109.29, 107.99, 107.02, 106.35, 100.54, 67.25, 54.00, 48.94, 46.93, 32.45, 30.10, 29.87, 27.30, 26.26, 23.22, 14.42, 8.53
See figure 9.28 on page 109
MALDI-TOF: *m/z*: [M$^+$] calculated: 578.37 found: 578.25
See figure 9.47 on page 123

4.1.13 Synthesis of 3-Chloro-4-hydroxybenzylamine

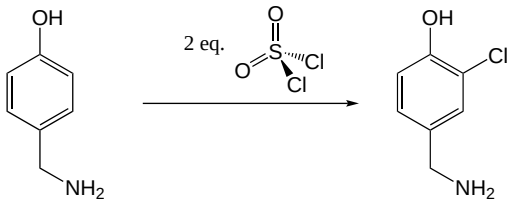

Figure 4.10: Synthesis of 3-Chloro-4-hydroxybenzylamine

3-Chloro-4-hydroxybenzylamine was synthesised according to [76]. 291 mg (2.35 mmol) of 4-hydroxybenzylamine were dissolved in 0.5 mL DMF, 4,583 mL acetic acid and 0.417 mL HCl conc. so that HCl was 1 M in acetic acid. After 441 µL (2 eq., 5.46 mmol) sulfuryl chloride were added, the reaction mixture was stirred for 2 h at room temperature, during which a white precipitate formed. This was separated via centrifugation, washed thrice with 5 mL acetic acid and once with clean DCM (5 mL).

Yield: 204 mg, 63 %

^{1}H NMR (300 MHz, CD_2Cl_2): $\delta = 7.45$ (d, $J = 2.2$ Hz, 1H, *p*-Cl aromat. C-H), 7.24 (dd, $J = 8.4$, 2.2 Hz, 1H, aromat. C-H), 6.97 (d, $J = 8.3$ Hz, 1H, *p*-OH aromat. C-H), 4.01 (s, 2H, CH_2)
See figure 9.30 on page 110

4.1.14 Attempted Snthesis of *N*-3-Chloro-4-hydroxybenzyl-*N*-dodecyl DAOTA$^+$

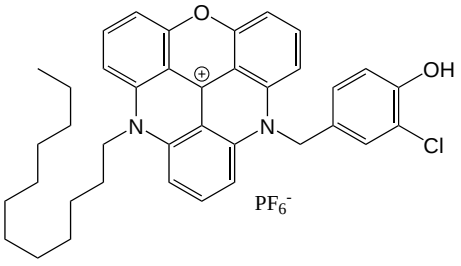

Figure 4.11: Structure of *N*-3-Chloro-4-hydroxybenzyl*N*-dodecyl DAOTA$^+$

Analogously to the procedure in 4.1.12, intermediate **(b)** (332.3 mg, 0.76 mmol) was converted to tris(2,6-dimethoxyphenyl)carbenium by adding 3 eq. (255 µL) aqueous HBF_4 (50 wt.%),

precipitated from EtOH with CH. The tris(2,6-dimethoxyphenyl)carbenium was dissolved in acetonitrile together with 1 eq. (119.1 mg, 0.76 mmol) 3-chloro-4-hydroxybenzylamine and stirred at room temperature until no purple intermediate could be detected by TLC anymore. After a precipitation step with 0.2 M KPF_6 the 3-chloro-4-hydroxybenzyl bearing, nitrogen-bridged intermediateb was dissolved in NMP and 1 eq. dodecylamine (142.4 mg, 0.77 mmol) was added. Stirring at 80°C was followed by another precipitation step. The oxygen bridge was formed by heating to 180°C for 1 h in molten PyHCl followed by a last precipitation step.
The desired substitution with 3-chloro-4-hydroxybenzylamine could not be achieved. Even adding catalytic amounts of base (TEA or pyridine) in the first substitution step did not result in higher conversion. MS showed that only the di-*N*-dodecyl $DAOTA^+$ could be formed (figure 9.50, page 127).

4.1.15 Synthesis of *N*-(3,5-Dichloro-4-hydroxyphenyl)-*N*-dodecyl DAOTA (Dye (4))

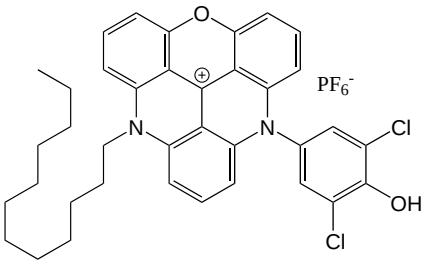

Figure 4.12: Structure of *N*-3,5-Dichloro-4-hydroxybenzyl*N*-dodecyl $DAOTA^+$

Synthesis was performed analogously to previous procedures. 1.25 g **(b)** (2.84 mmol) were acidified with 3 eq. 50 wt.% aqueous HBF_4 (1 mL, 16.1 mmol). The once nitrogen bridged intermediate was synthesised with 508.4 mg 3,5-dichloro-4-hydroxyaniline (1 eq., 2.86 mmol), a few drops of pyridine were added as non-nucleophilic, basic catalyst and after the usual precipitation step, doubly nitrogen bridged intermediate was synthesised by stirring at 95°C under Ar with 2.73 g dodecylamine (5 eq., 14.7 mmol). The precipitated intermediate was dissolved in molten PyHCl and stirred at 180°C for 1 h and the final dye precipitated again in aqueous KPF_6. The product was purified with two flash column chromatographies and then fat was removed by precipitation from clean DCM with CH and separation via centrifugation.

Yield: 97 mg, 5 %

^{1}H NMR (300 MHz, CD_3OD): $\delta = 8.08$ (td, $J = 8.4$, 5.5 Hz, 2 H, aromat. C-H), 7.91 – 7.79 (m, 1 H, aromat. C-H), 7.59 (d, $J = 8.9$ Hz, 1 H, aromat. C-H), 7.46 (d, $J = 8.6$ Hz, 1 H, aromat.

C-H), 7.27 (d, $J = 8.2$ Hz, 1 H, aromat. C-H), 7.20 (d, $J = 13.6$ Hz, 3 H, 1 H: triangulenium aromat. C-H, 2 H: substituent aromat. C-H), 6.84 (d, $J = 8.6$ Hz, 2 H, aromat. C-H), 4.58 – 4.41 (m, 2 H, N-CH_2), 1.92 (p, $J = 8.1$, 7.6 Hz, 2 H, aliphat. CH_2), 1.62 (p, $J = 7.2$ Hz, 2 H, aliphat. CH_2), 1.46 (dq, $J = 11.6$, 6.1, 5.3 Hz, 2 H, aliphat. CH_2), 1.31 (d, $J = 16.4$ Hz, 16 H, aliphat. CH_2), 0.95 – 0.81 (m, 3 H, CH_3)
See figure 9.32 on page 111
APT-NMR (76 MHz, CD_3OD): $\delta = 145.10$, 143.64, 142.04, 140.82, 140.18, 139.53, 128.27, 127.89, 112.17, 110.63, 109.95, 109.05, 107.30, 64.72, 49.00, 33.34, 31.03, 30.72, 27.91, 27.20, 24.00, 14.71
See figure 9.34 on page 112
MALDI-TOF: m/z: [M^+] calculated: 611.22 found: 611.12
See figure 9.43 on page 119

4.1.16 Synthesis of *N*-(3-Chloro-4-hydroxyphenyl)-*N*-dodecyl DAOTA$^+$ (Dye (5))

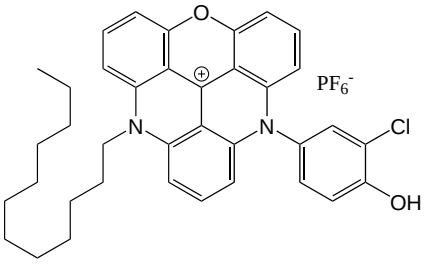

Figure 4.13: Structure of *N*-3-Chloro-4-hydroxybenzyl*N*-dodecyl DAOTA$^+$

Synthesis was performed analogulously to 4.1.15. 430.45 mg **(b)**, 3 eq. HBF_4, 148.1 mg 3-chloro-4-hydroxyaniline (1 eq.) and 942.2 mg dodecylamine (5 eq.) were used for the reaction. Separation of residual doubly nitrogen-bridged intermediate proved to be especially challenging. In emission spectra, very efficient energy transfer could be observed between the final dye ($\lambda_{em^{max}} = 595$ nm) and the intermediate in the product mixture ($\lambda_{abs^{max}} = 610$ nm, $\lambda_{em^{max}} = 660$ nm)(see figure 9.52 on page 128). Purification was achieved by flash column chromatography, multiple times on both silica and AlOx as well as multiple precipitations from clean DCM with CH to remove fat.
Yield: 32 mg, 4 %

^{1}H NMR (300 MHz, CD_2Cl_2): $\delta = 8.13$ (t, $J = 8.5$ Hz, 1H, aromat. C-H), 8.04 (t, $J = 8.6$ Hz, 1 H, aromat. C-H), 7.97 – 7.81 (m, 2H, 1 H: triangulenium aromat. C-H, 1 H: substituent *p*-OH aromat. C-H), 7.48 (d, $J = 8.8$ Hz, 1 H, aromat. C-H), 7.43 – 7.27 (m, 4 H, 3 H: triangulenium

aromat. C-H, 1 H: substituent *p*-Cl aromat. C-H), 7.19 – 7.07 (m, 1 H, substituent aromat.C-H), 6.87 – 6.73 (m, 2 H, aromat. C-H), 4.51 (t, $J = 8.3$ Hz, 2 H, N-CH_2), 2.00 (p, $J = 7.5$ Hz, 2 H, aliphat. CH_2), 1.71 – 1.54 (m, 2 H, aliphat. CH_2), 1.45 (s, 2 H, aliphat. CH_2), 1.40 – 1.11 (m, 14 H, aliphat. CH_2), 0.88 (t, $J = 6.5$ Hz, 3 H, CH_3).
See figure 9.36 on page 113
APT-NMR (76 MHz, CD_2Cl_2): $\delta = 145.10$, 143.64, 142.04, 140.82, 140.18, 139.53, 128.27, 127.89, 112.17, 110.63, 109.95, 109.05, 107.30, 64.72, 49.00, 33.34, 31.03, 30.72, 27.91, 27.20, 24.00, 14.71
See figure 9.38 on page 114
MALDI-TOF: *m/z*: [M^+] calculated: 577.26 found: 577.25
See figure 9.45 on page 121

4.1.17 Overview of Successfully Synthesised Dyes

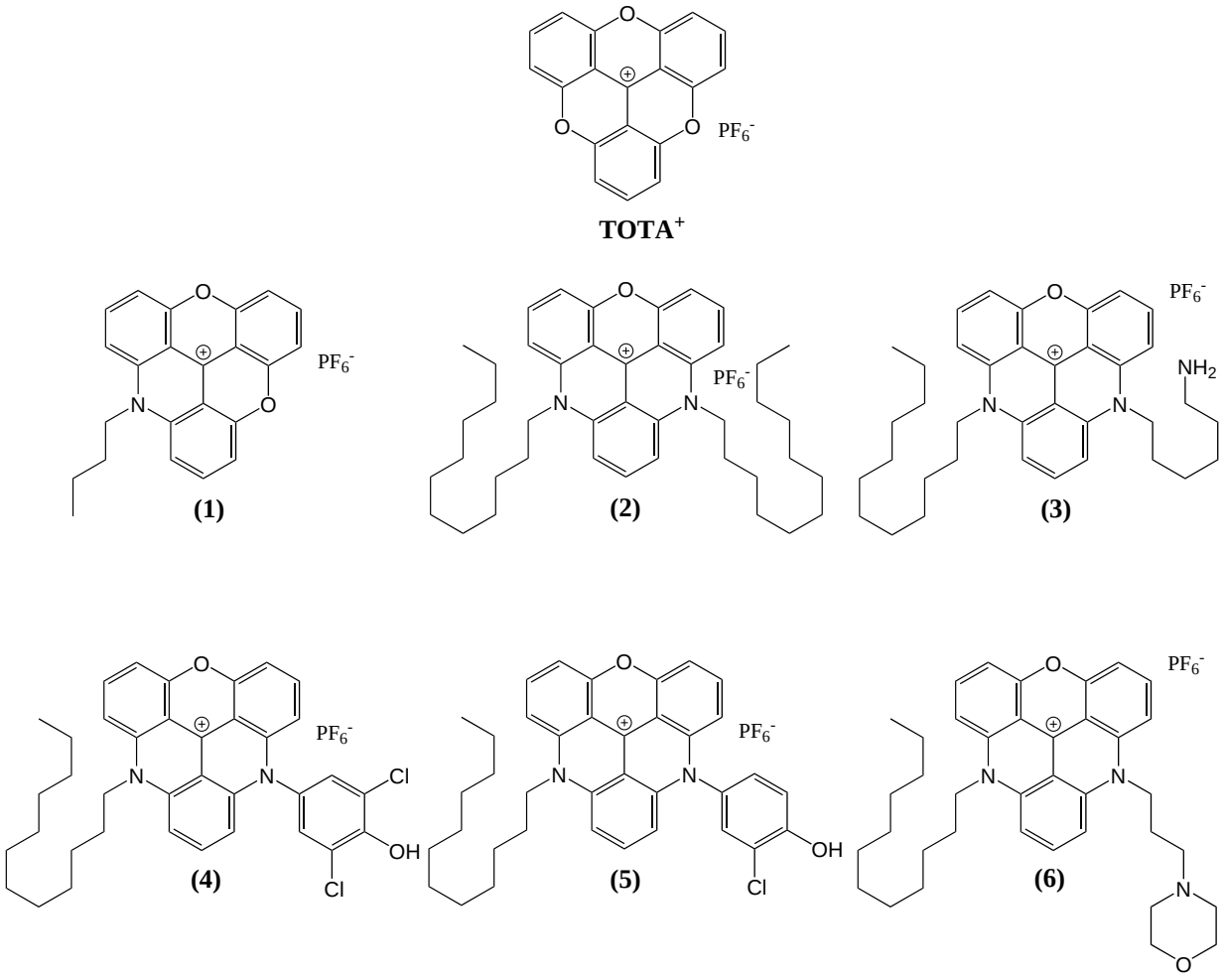

Figure 4.14: Overview of synthesized dyes

4.2 Preparation of Sensor Layers

4.2.1 Preparation of 5 wt.% Layers of Dye (2) and (4) in D4

A stock of 1.00 g D4 in 9.011 g EtOH H_2O (9+1) was prepared. 5.1 mg of dye **(2)** and **(4)** were added to 1.022 and 0.994 g of the cocktails, respectively. Homogeneous distribution was achieved by ultrasonication. The cocktail was knife coated onto Mylar® with film thicknesses of 25.4 µm and 76.2 µm (1 and 3 mil).

4.2.2 Preparation of 1 wt.% Sensor Layers of dye (4), (5) and (6) in D4, D1 and pHEMA

Table 4.1: Weighed portions of 1 wt.% dye/polymer sensing layers of dyes **(4), (5)** and **(6)** in [mg]

	dye	D4	solvent	dye	D1	solvent	dye	pHEMA	solvent
(4)	0.57	60.4	540.4	0.58	62.1	539.9	0.59	60.8	540.3
(5)	0.63	57.0	515.7	0.40	52.4	445.5	0.57	61.0	545.8
(6)	0.69	66.6	603.0	0.50	52.4	445.5	0.66	61.5	545.4

As solvent a mixture of EtOH and H_2O 9+1 was used. Again dissolution and homogenization was facilitated by ultrasonication. Knife coating was performed with a 76.2 µm (3 mil) knife on a Mylar® foil.

4.3 Determination of Chloride Dependence

To exclude dynamic quenching of fluorescence by halide ions as it is known for acridine dyes [38], excitation and emission spectra of planar optodes of dyes **(2)** and **(4)** (5 wt.% in D4, 1 mil thickness) were recorded in buffers of different chloride concentration but constant ionic strength. For this purpose, three buffer solutions with 20 mM concentration of MES buffer and 100 mM concentration of Na-salt were prepared. The used NaCl concentrations were 0, 80 and 100 mM the ionic strength was set to 100 mM by adding the difference in $NaNO_3$.

4.4 pH Calibrations

The pH dependence of fluorescence intensity of all PET dyes was investigated for sensor layers with 1 wt.% dye in D4, D1 and pHEMA and in solution. Dye **(4)** was also investigated in sensor layers containing 5 wt.% dye in D4. The pH dependence of fluorescence decay time was investigated for dyes **(4), (5)** and **(6)** at 1 wt.% concentration in D4, D1 and pHEMA. Dyes **(4)** and**(6)** were measured at 25°C in D4, D1 and pHEMA, dye **(5)** at 15, 25 and 37°C . In addition, fluorescence lifetime of dye **(5)** was also determined in solution (1+1 buffer and EtOH solution of dye) at 25°C.

4.4.1 Buffer Preparation

Fluorescence intensity calibration was performed at four ionic strengths, 20, 50, 150 and 500 mM with a constant buffer concentration of 10 mM and varying concentrations of NaCl to fit the target ionic strength. Depending on the expected apparent pK_a value of the dyes, different pH values were used as measurement points and intervals were smaller close to the expected transition range. Dye **(4)** was measured at pH 3, 3.5, 4, 4.5, 5, 5.5, 5.9, 6.3, 6.7, 7.1, 7.5, 8 and

9. Dyes **(5)** and **(6)** were measured at pH 4, 5, 6, 6.5, 7, 7.5, 7.8, 8.1, 8.4, 8.7, 9, 9.5, 10 and 11. Buffers for calibration points at pH 10 and 11 were prepared with 10 mM CAPS buffer and NaCl for setting the ionic strength to the desired values. All other buffers consisted of 3.33 mM acetic acid, 3.33 mM phosphoric acid and 3.33 mM TRIS buffer and the corresponding amount of NaCl setting the ionic strength to the desired values (20, 50, 150 and 500 mM).
Fluorescence decay time calibration was carried out at the same pH values as mentioned above using buffers with an ionic strength of 150 mM. Furthermore, pH dependence of fluorescence decay time of dye **(5)** was also measured at different buffer concentrations. For this purpose, buffers with 10 mM and 16.67 mM concentration of acetate, phosphate and TRIS each were prepared for pH values 4, 5, 6, 6.5, 7, 7.5, 8, 8.5 and 9. Calibration points for pH 10 and 11 were provided by buffers with 30 and 50 mM CAPS. Again total ionic strength of the buffers was adjusted to 150 mM by addition of NaCl.

4.4.2 Preparation of Microtiterplates for Fluorescence-Intensity pH Calibration

Setup of Microtiterplates with Sensing Layers

96-well polystyrene clear microtiterplates with F-bottom from Greiner® were used for simultaneous read-out of multiple sensing spots at different conditions at a time. For this purpose, circular parts of the sensing layers were punched out using a circular stamping tool 6 mm in diameter. The sensing layer spots were fixed at the bottoms of the wells with a spot of vacuum grease. The setup of the microtiterplates is illustrated in figure 4.15.

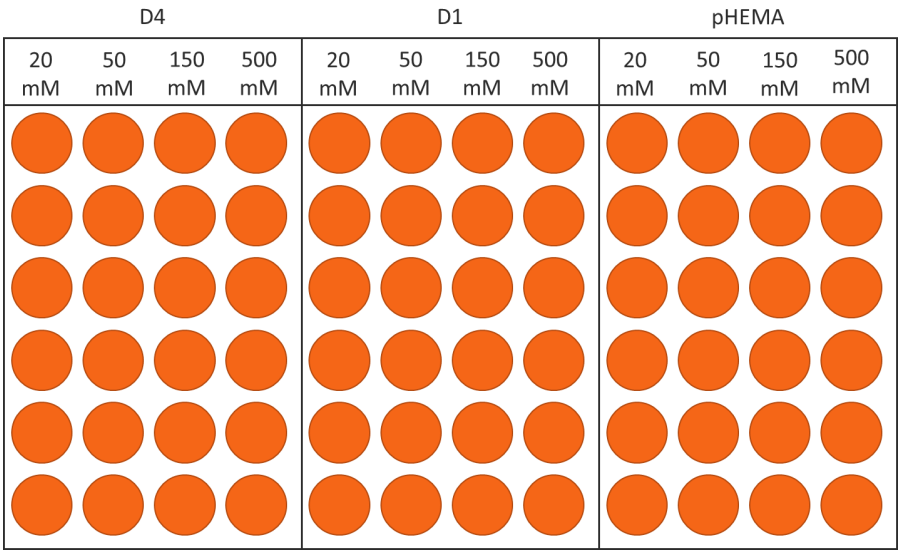

Figure 4.15: Setup of microtiterplates, fluorescence intensity of one dye was measured at one pH value in three matrices and at four different ionic strengths at six sensing spots each

Measurement of Dyes in Solution with Microtiterplates

To calibrate the dyes in solution, buffer with a concentration of 20 mM and ionic strengths of 40, 100, 300 and 1000 mM was mixed 1+1 (150 µL each) with an EtOH solution of the dye. The measurement solution contained 10 mM buffer and an ionic strength of 20, 50, 150 and 500 mM respectively. The dye concentration was adapted to set the absorption to 0.1 in the measurement solution.

4.5 Nanoparticles

4.5.1 Preparation of Nanoparticles

Preparation of nanoparticles was conduucted according to [71, 72]. Nanoparticles of dyes **(4)** were prepared in RL-100, those of dye **(5)** in RL-100 as well as in PMMA-MA (9:1) polymer. Dye concentration was always 0.75 wt.% with respect to the polymer. Dye **(4)** (1.21 mg) and 161.5 mg of RL-100 polymer were dissolved in 80 mL Acetone. Under vigorous stirring, 480 mL H_2O were added rapidly to achieve nanoparticle formation. For dissolving dye **(5)** (0.98 mg) and RL-100 polymer (129.6;mg), 65 mL acetone were used while for dissolution of 0.80 mg dye **(5)** and 107.0 mg PMMA-MA, 53 mL of an Acetone-THF mixture were used (ratio 55:45). Precipitation of the nanoparticles from the solution was achieved by fast addition of 300 mL H_2O under vigorous stirring.
The organic solvents were removed on a rotary evaporator and the aqueous dispersion concentrated to final concentrations of 1.44 mg/mL (dye **(4)** in RL-100), 1.3 mg/mL (dye **(5)** in RL-100) and 1.0 mg/mL (dye **(5)** inPMMA-MA).

4.5.2 pH Calibration of Nanoparticles

Fluorescence intensity and decay time of the nanoparticles was investigated in dependence of pH. For calibration of dye **(5)**, buffer solutions with concentrations of 6.66 mM phosphoric acid, acetic acid and TRIS buffer each were prepared and their ionic strength set to 300 mM with NaCl. The buffer solution was mixed 1+1 with the nanoparticle dispersions and emission spectra and decay time were recorded at room temperature. RL-100 particles were investigated at ten different pH values between pH 3 and pH 9 while for investigation of PMMA-MA particles, ten measurement points in the range of pH 5 to pH 13 were used. The pH range for calibration of dye **(4)** nanoparticles was from pH 2 to pH 6. Buffers in the lower pH range (< pH5) contained acetic acid and phosphoric acid in a concentration of 10 mM each and were set to a total ionic strength of 300 mM with NaCl. The buffers for the higher pH values were the same as used in calibration of RL-100 nanoparticles of dye **(5)**. All buffers were mixed 1+1 with the nanoparticle dispersions for the measurements.

4.6 Photostability

Photobleaching behaviour of dye **(5)** in ethanol was investigated in comparison with Macrolex®Fluorescent Red G and Rhodamine 101. The solutions were prepared so that the absorption at the illumination wavelength (528 nm) was approximately at 0.3. Every five minutes the absorption of the measurement solution and the illumination intensity were measured. The light intensities for each measurement were averaged and are given in table 4.2.

Table 4.2: Average light intensities (measured as photon flux) during photostability measurements of dye **(5)**, Macrolex® Fluorescent Red G and rhodamine 101

Dye	Average photon flux[$\mu mol\, s^{-1}\, m^{-2}$]
MonoCl DAOTA$^+$	11703
Macrolex® Fluorescent Red G	9110
Rhodamine 101	8404

4.7 Leaching Tests

Leaching of dye **(4)** from sensor layers with 1 wt.% dye in D4 and pHEMA was investigated. 10 mM buffers of acetate and phosphate with pH 4 and 6.5, respectively, were used. The ionic strength of both buffers was set to 150 mM by adding 140 mM NaCl. The flow set was 10 mL/h, during buffer change the flow was increased twenty-fold for about 1 min.
When investigating the D4 sensor layer, at first the buffer was changed every 30 minutes. A slight decrease in absorption could be observed when going from an acidic to near-neutral pH. After two hours, the measurement was continued overnight while cycling the acetate buffer. In the morning the buffer was changed again and the phosphate buffer cycled two more hours.
For the pHEMA sensor layer, the buffers were changed every hour for four hours.

5 Results and Discussion

The three succssfully synthesised dyes containing PET groups (**(4), (5)** and **(6)**) were investigated closer as well as the dye substituted with two dodecyl chains (dye **(2)**), to confirm that the photophysical characteristics (absorption coefficient, lifetime, quantum yield) are not gravely changed by introduction of the PET group.

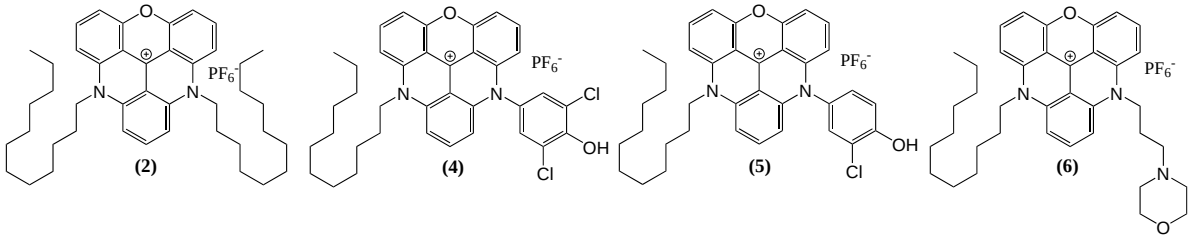

Figure 5.1: Dyes that were investigated with regard to their photophysical properties

The dyes were designed with a dodecyl chain for better solubility and a PET group for pH sensitivity. The different phenolic PET groups were introduced to obtain dyes with different pK_a, low with the dichloro-substituent (dye **(4)**) and higher with the monochloro-substituent (dye **(5)**). It was hoped that the amine PET group, would not only show a pK_a value slightly above the physiological range but also only partial quenching of fluorescence. The attempt to synthesise a dye where the 3-chloro-4-hydroxyphenol substituent is linked to the triangulenium core via a CH_2 spacer was aimed at obtaining a dye where the phenolic PET group is decoupled from the conjugated system.

5.1 Synthetic Considerations

The aim of this thesis was to synthesise new triangulenium dyes equipped with different pH sensitive PET groups. The general synthetic route was similar to the one reported in [11]. Because of the longer wavelength of the absorption maximum of $DAOTA^+$ dyes, they were preferred over $ADOTA^+$ or $TATA^+$ dyes. One of the nitrogen bridges was then functionalised with a PET group, the other nitrogen bridge was substituted with a dodecyl chain to increase the solubility of the dye in organic solvents. Because the solubility in many organic solvents was still low, polar solvents such as acetonitrile and NMP were used for synthesis. NMP was only used where elevated temperatures were required because it usually complicated purification by causing

the fractions in flash column chromatography to slur and thereby diminishing separation quality.

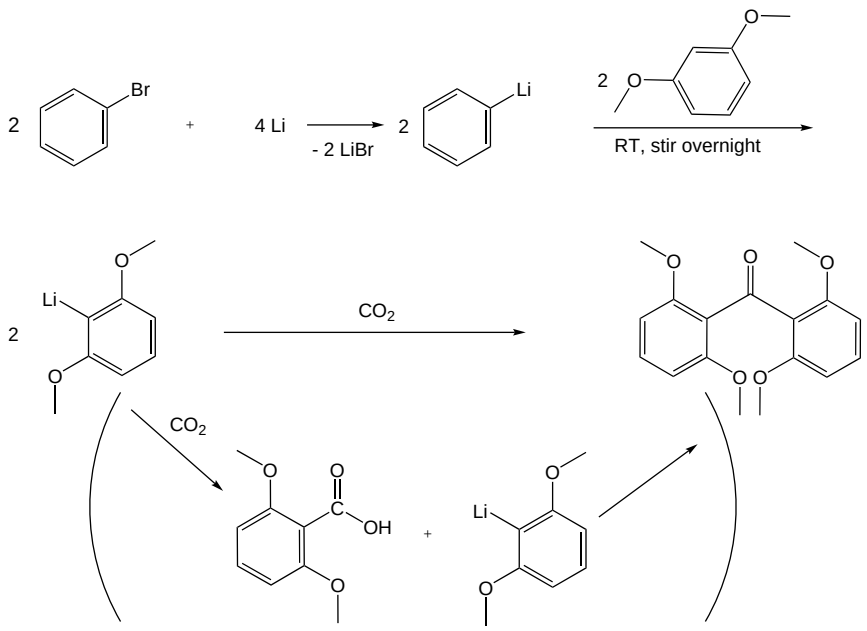

Figure 5.2: Synthesis of 2,2',6,6'-tetramethoxybenzophenone from 1,3-dimethoxybenzene and phenyllithium

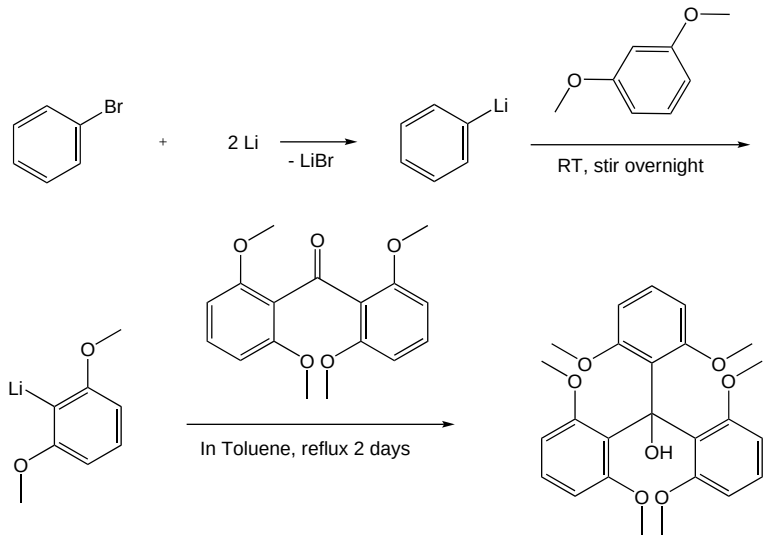

Figure 5.3: Synthesis of tris(2,6-dimethoxyphenyl)methanol from 1,3-dimethoxybenzene and 2,2',6,6'-Tetramethoxybenzophenone

The tris(2,6-dimethoxyphenol)methanol serves as educt for synthesis of $TOTA^+$, $ADOTA^+$ and $DAOTA^+$ dyes. Synthesis of educt **(b)** was conducted according to Wittig and Pockels and Martin et al. [62, 73]. The reactions were performed under argon in a Schlenk tube. The

following substitution-ring closing reactions were executed similar to procedures described by Krebs, Laursen et al. [11, 75] with modifications as demanded by the synthetic problem.
The synthesis from tris-(2,6-dimethoxyphenyl)methanol occurred in all cases via subsequent $S_{N^{Ar}}$ reactions, in which the methoxy groups were substituted with corresponding nucleophiles (here: primary amines) leading to ring closure. The last step is the thermally catalyzed intramolecular oxygen ring closure at 180°C in molten PyHCl following an Olah-Svoboda mechanism [77] Due to the increase in size of the planar system with each ring closing step, the positive charge becomes more delocalized, decreasing the electrophilicity of the electrophile carbon and therefore also the tendency towards nucleophilic substitution. For this reason, while the first nitrogen bridge will usually form easily when stirring the carbenium with a primary amine at room temperature, the second nucleophilic substitution has to be carried out at elevated temperatures. When the reaction velocity was very slow, a few drops of TEA or pyridine were added as a non nucleophilic base to catalyse the elimination step.

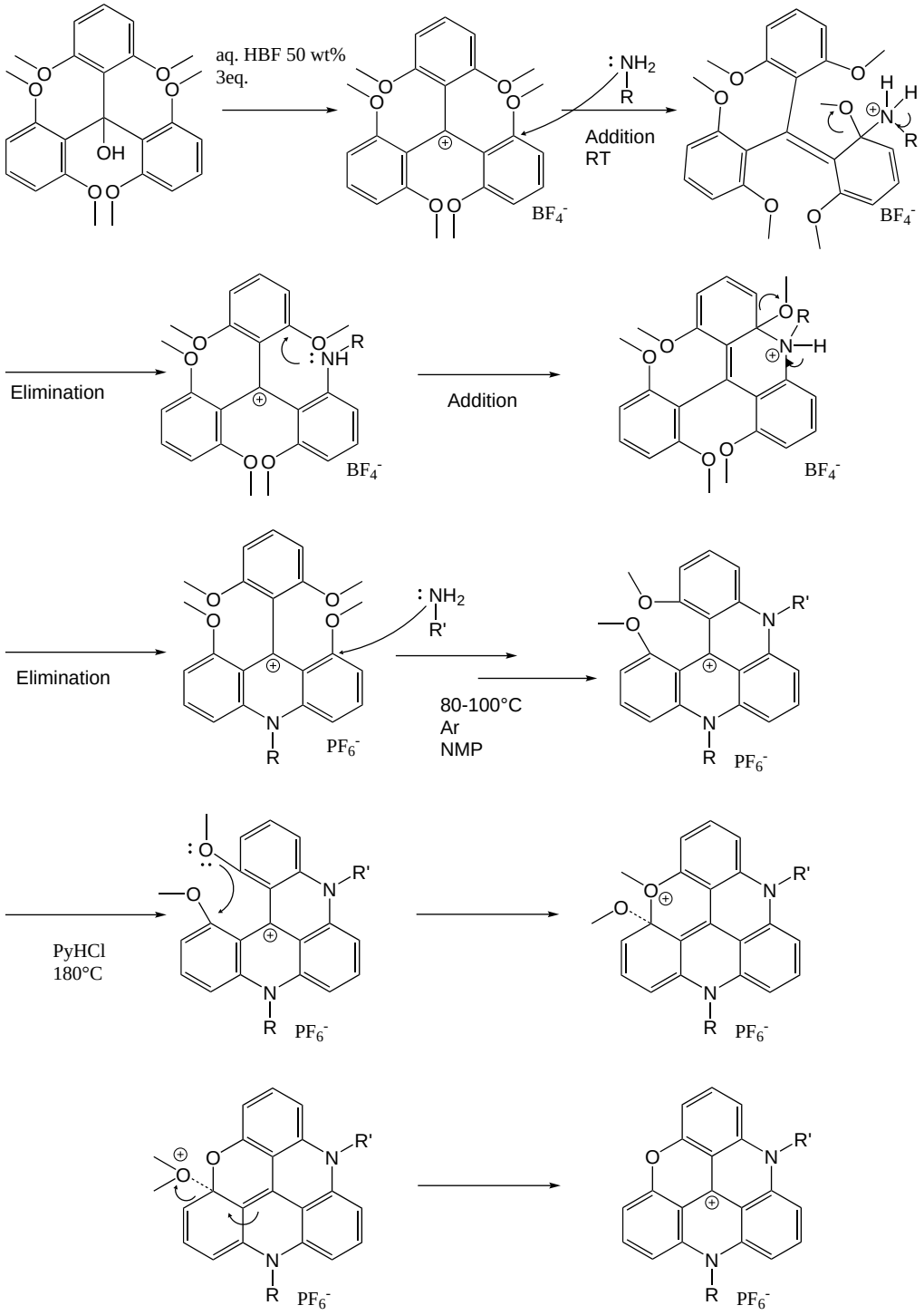

Figure 5.4: Detailed reaction scheme portraying the single steps of the reaction from the tris(2,6-dimethoxy)methanol educt to the final DAOTA$^+$ dye

Due to the decrease in reactivity with each step, substitution with a less nucleophilic amine was conducted first, and the more reactive amine (usually dodecylamine) was introduced second.

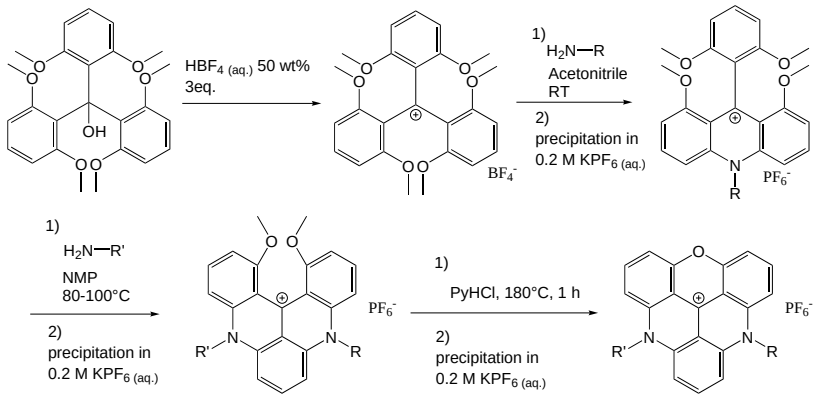

Figure 5.5: General reaction scheme of DAOTA$^+$ Synthesis where H_2N-R is less nucleophilic than H_2N-R'

The extent of this influence becomes apparent during synthesis of the the morpholino DAOTA$^+$ (section 4.1.11 and 4.1.12), when substitution of the dodecyl-substituted, nitrogen bridged intermediate with 3-morpholinopropylamine would not yield the desired product but when changing the order of synthesis steps, dye **(6)** could successfully be synthesised.

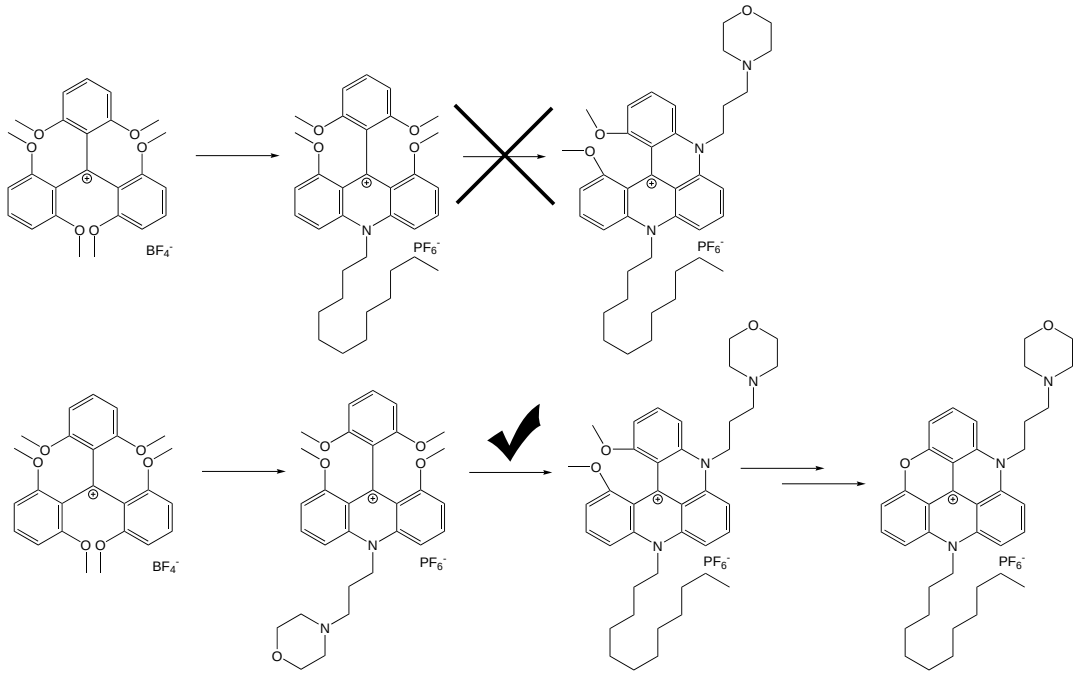

Figure 5.6: Unsuccessful and successful synthetic route to dye **(6)**

The reason for the unsuccessful synthesis of the diisopropylphenyl substituted DAOTA$^+$ (section 4.1.7) is probably the sterical hindrance of the aniline due to the two isopropyl groups in ortho position to the amino group. The aniline has to undergo two S_{NAr} reactions, to create one nitrogen bridge. While the first S_{NAr} reaction migth still take place, the second one would

have to overcome not only the steric hindrance of the two diisopropylphenyl groups but it is further hindered by the attached triarylcarbenium residue, rendering the nitrogen atom too sterically crowded for another nucleophilic attack as is illustrated in figure 5.7.

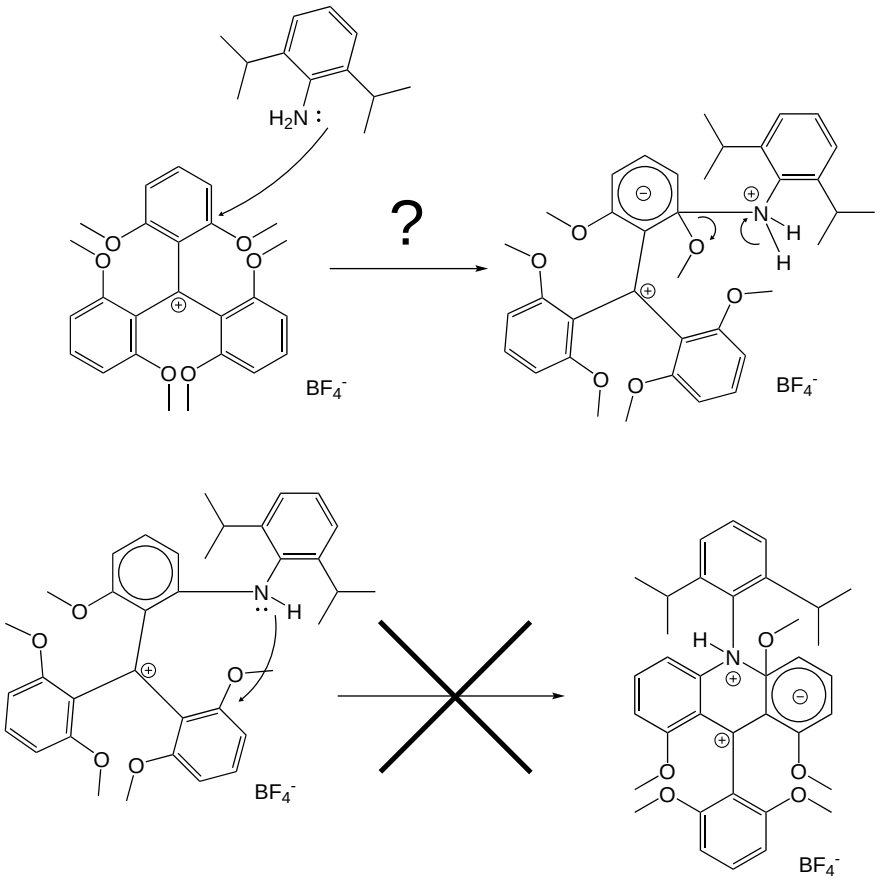

Figure 5.7: Sterical hindrance ocurring when trying to substitute the carbenium precursor with 2,6-diisopropylaniline

The problems in synthesis of *N*-(4-bromophenyl)-*N*-dodecyl DAOTA$^+$ are most likely due to the low electrophilicity of the *p*-bromoaniline due to the electron withdrawing bromine substituent. It has to be kept in mind that a single amine has to undergo two nucleophilic substitutions for one successful ring closing reaction. The amine becomes less nucleophilic by addition of the positively charged carbenium compound in the first $S_{N^{Ar}}$ reaction which, additionally to higher steric hindrance, hampers the second $S_{N^{Ar}}$ reaction. For this reason the nucleophilicity of *p*-bromoaniline is apparently insufficient for successful substitution and ring closing. Hammershoj et al. reported successful substitution with *p*-bromoaniline only under base catalysis with NaH [78], this procedure was not attempted during this thesis.

5.2 Dye Characterisation

5.2.1 Photophysical Properties

The quantum yields were acquired in presence of 3 μL TFA/2.5 mL solution to assure acidic conditions and "on" state of the dyes. The molar absorption coefficients were determined according to Lambert Beer's law (2.4), the relative quantum yields according to equation 3.2 with Fluorescent Red as a reference dye. For dye **(2)** and **(4)** THF was chosen as a solvent, dyes **(5)** and **(6)** were less soluble in THF, so ethanol was used as solvent instead. Fluorescence lifetimes were determined via time correlated single photon counting and a Boltzmann fit was used to obtain a sigmoidal decay curve.

Table 5.1: Molar absorption coefficients, quantum yields and lifetimes of dyes **(2)** (didodecyl), **(4)** (dichloro), **(5)** (monochloro) and **(6)** (morpholino)

	$\lambda_{abs}max$ [nm]	$\lambda_{em}max$ [nm]	ε [$L\,mol^{-1}\,cm^{-1}$]	Φ_{abs} [%]	Φ_{rel} [%]	Φ_{mean} [%]	τ [ns]
(2) in THF	558	588	-	78	69	73	19.8
(4) in THF	561	588	14200	90	75	82	17.8
(4) in EtOH	562	589	13800	45	80	63	17.3
(5) in EtOH	562	590	10600	55	63	59	17.7
(6) in EtOH	559	589	9800	47	49	48	19.0

In table 5.1 it can be seen that the quantum yields of dye **(4)** are different in THF and EtOH. The absolute quantum yield of dye **(4)** (dicloro DAOTA$^+$) is decreased in an ethanol solution as compared to a THF solution. Also the quantum yield of fluorescent red, which was used as a reference, decreased from 96 % in $CHCl_3$ [69] to 92 % and 69 % in THF and EtOH respectively (determined experimentally). It is likely that dyes **(5)** and **(6)** will also have higher quantum yields (and therefore higher brightness) in THF. As can be seen in figure 5.8 the absorption coefficients slightly decrease from dye **(4)** (dichloro DAOTA$^+$) to dye **(6)** (morpholino DAOTA$^+$). Combined with the trend observed for the quantum yields this results in a higher fluorescence brightness for dye **(4)** while dye **(6)** has the lowest brightness. This is not necessarily true, however, since even a small contamination e.g. with fat could explain the observed trends just as well.

The overall shape of absorption and emission spectra is very similar for all DAOTA$^+$ dyes. Depending on the substituent and solvent, small shifts (few nm) to higher or lower wavelengths are possible. They have a maximum absorption band at about 560 nm and an emission band at around 590 nm. When changing the solution pH from acidic to basic, the absorption spectra change slightly. In case of the dichloro dye ((**4**) in THF, it seems as if aggregation occurs at high pH. Both the mono-and dichloro dye ((**4**) and **(5)**) show a bathochromis shift of a few nanometers when basifying the solution. While dye **(4)** shows increase in absorption at high pH, absorption of dye **(5)** decreases slightly. Emission of all dyes is quenched completely in very

basic solution. In only moderately basic environment (around pH 10), dye **(6)** is not completely quenched yet, while the other two show no detectable fluorescence anymore.
In all dyes, the characteristic and desired long lifetimes of up to almost 20 ns could be observed. These long lifetimes were the main reason for choosing triangulenium dyes for the design of new pH indicators, so retaining this characteristic feature upon PET-functionalisation is an important success.

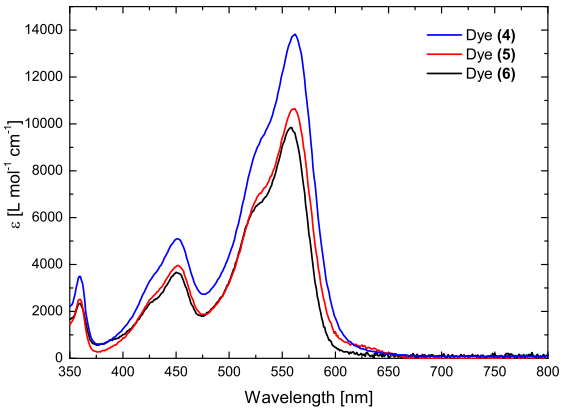

(a) Absorption coefficients in EtOH

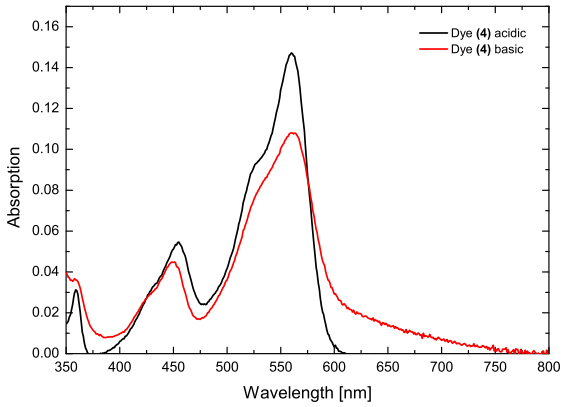

(b) Dye **(4)** in THF

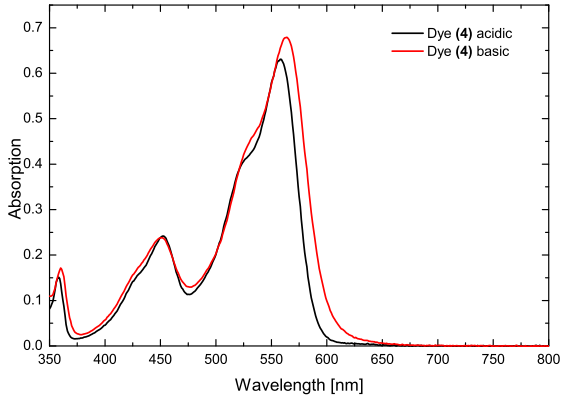

(c) Dye **(4)** in EtOH

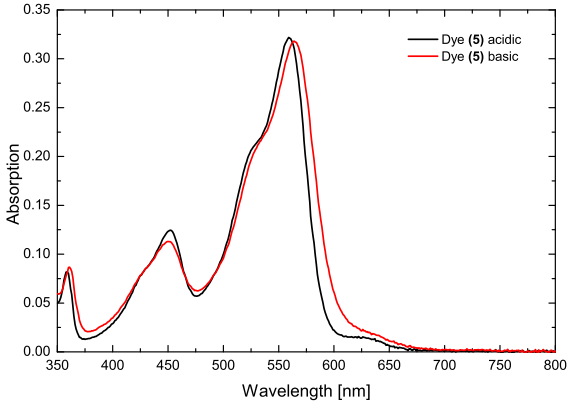

(d) Dye **(5)** in EtOH

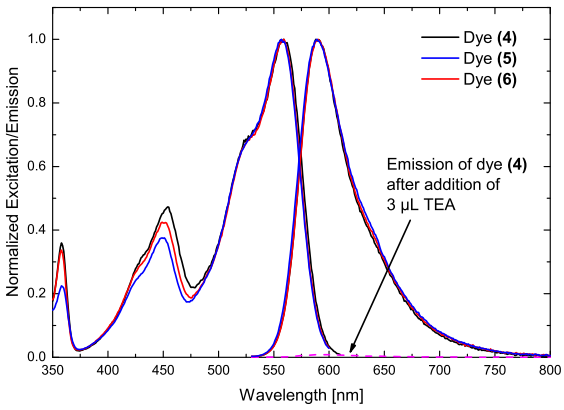

(e) Dyes **(4)**, **(5)** and **(6)** in EtOH

Figure 5.8: (a) Absorption spectra of dyes **(4)**, **(5)** and **(6)**, (b)-(d) influence of pH on absorption spectra of dye **(4)**; (e) **(5)** and excitation and emission spectra of dyes **(4)**, **(5)** and **(6)**

As can be seen in figure 5.8(e), the stokes shift between absorption and emission maximum is around 30 nm for all dyes. If the dyes are excited in the peak at 450 nm, an even bigger stokes shift of ∼130,nm can be achieved.

5.2.2 Photostability

Dye **(5)** showed moderate decrease in maximum absorption after illumination for an hour with a high power LED. While Macrolex® Fluorescent Red G showed almost no change in maximum absorption, the photobleaching of rhodamine 101 was significantly more pronounced. The behaviour of the mono-chloro-DAOTA$^+$ dye **(5)** is in between those of both reference dyes as can be seen in figure 5.9.

It has to be kept in mind that the average light intensity, measured as photon flux, was highest during illumination of dye **(5)** (11700 $\mu mols^{-1}m^{-2}$ or 2650 Wm^{-2}), while during illumination of the reference dyes it was slightly lower (9100 $\mu mols^{-1}m^{-2}$ or 2060 Wm^{-2} for Macrolex® Red and 8400 $\mu mols^{-1}m^{-2}$ or 1900 $Wm^{-2}$for rhodamine 101). Considering this, if measured at the same light intensity, the photostability of dye **(5)** would be even closer to that of Macrolex® Red. Even so, a decrease by less than four percent over one hour high intensity illumination indicates a excellent photostability for most applications (e.g. FLIM od intracellular measurements).

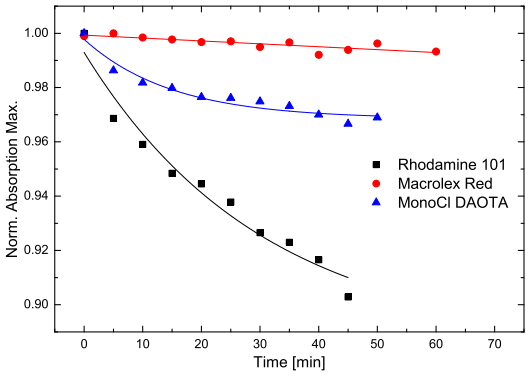

Figure 5.9: Decrease in absorption maximum of reference dyes and dye **(5)** during photostability measurement

5.3 Planar Optodes

Planar optodes of the pH sensitive dyes immobilised in different hydrogels (D4, D1 and pHEMA) were prepared and investigated to simulate real sensing applications. For such sensing layers, the stability of the dye in the hydrogel, i.e. the leaching behaviour of the dye is an important parameter. This was investigated by measuring the absorption of a sensing layer while constantly cycling a buffeer solution through the test cell. Furthermore the cross sensitivity to chloride had to be investigated, which was done by measuring the emission of the sensing layers in different buffers with constant ionic strength but varying chloride concentration which was adapted by using different portions of NaCl and $NaNO_3$. The main interest of this thesis id the pH sensitivity of the PET modified triangulenium dyes. For this reason, calibrations were done under different conditions and in buffers with varying ionic strengths. Both the fluorescence intensity and the lifetime were investigated for those calibrations. Upon immobilisation, absorption and emission spectra of the dyes did not change and quenching of fluorescence upon addition of base was still given.

5.3.1 Leaching Tests

Dye (4) 1 wt.% in D4

The protonated form of the dye, which is positively charged, was expected to be less stable in a hydrophobic matrix and has therefore higher leaching potential, the long period of overnight measurement was performed in the buffer of lower pH. It can be argued that the deprotonated form, although overall neutrally charged, is more polar because it is actually in a zwitterionic state. This would mean that actually the deprotonated form has higher leaching potential. Either way there does not appear to be a significant leaching of any of the two forms.

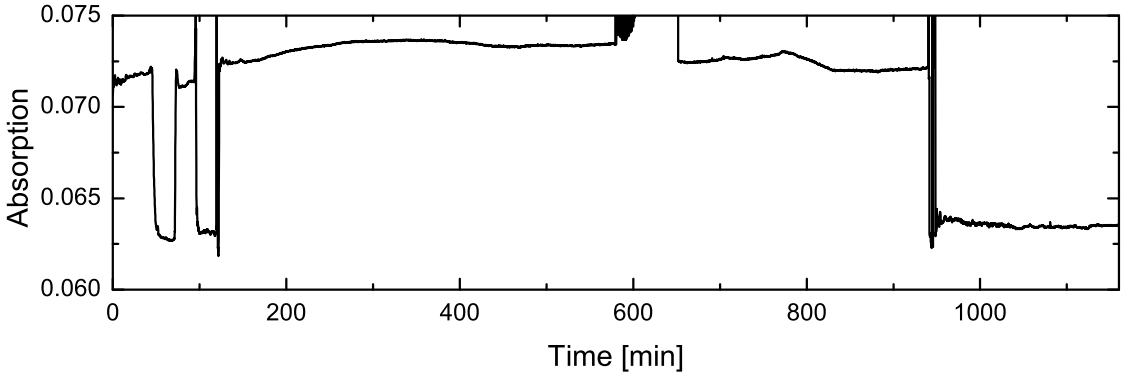

Figure 5.10: Leaching experiment of dye **(4)** 1 wt.% in D4, absorption measured at 560 nm in Phosphate buffer, pH 6.5 (lower absorption) and in acetate buffer, pH 4 (higher absorption)

The peaks seen in figure 5.10 can be attributed to turbulences and possibly air bubbles occuring during buffer change. The big distortion around 600 min is probably also due to entrapped air at some point during the overnight measurement.

Table 5.2: Change in Absorption behaviour during leaching experiment of 1 wt.% dye **(4)** in D4

	Start value	End value	Mean	Std. dev.	Max. value	Min. value
pH 4	0.071	0.072	0.073	$6.6 \cdot 10^{-4}$	0.073	0.071
pH 6.5	0.063	0.064	0.063	$2.3 \cdot 10^{-4}$	0.063	0.063

As can be seen in table 5.2, even though the absorption varies slightly over the measurement duration, the change is not significant. Therefore, it can be concluded that no detectable leaching has taken place over the duration of the experiment.

Dye (4) 1 wt.% in pHEMA

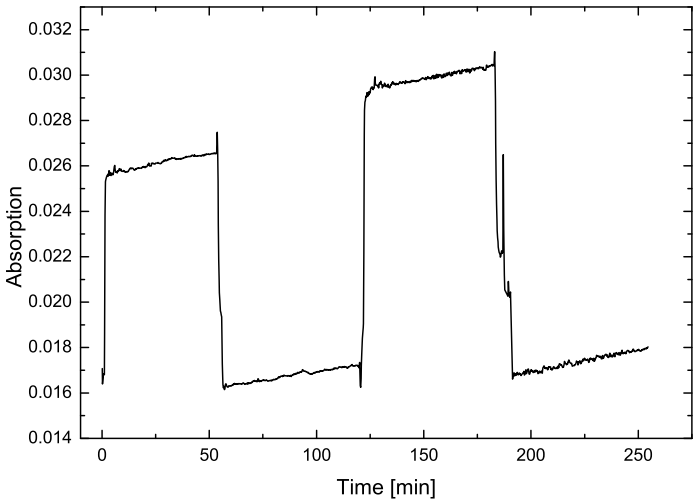

Figure 5.11: Leaching experiment of dye **(4)** 1 wt.% in pHEMA, absorption measured at 560 nm, in Phosphate buffer, pH 6.5 (lower absorption) and in acetate buffer, pH 4 (higher absorption)

Again some peaks can be seen at times of buffer change that are probably due to entrapped air (Figure 5.11). The rather big differences in absorption between acidic and basic conditions might be due to aggregation/disaggregation under those conditions. This might also explain the constant drift observed. Altogether, the absorption of the pHEMA sensing layers is very low compared to that in D4, further supporting this theory.

5.3.2 Chloride Cross Sensitivity

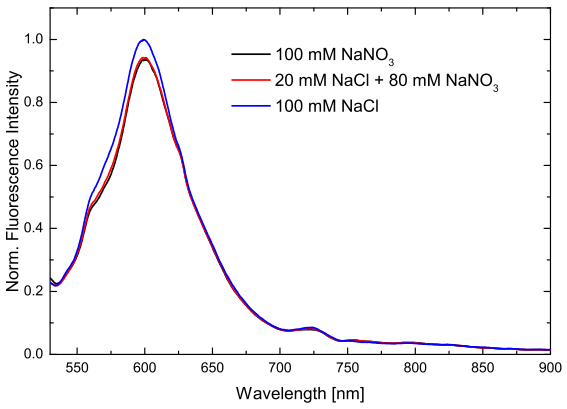

(a) Didodecyl DAOTA$^+$

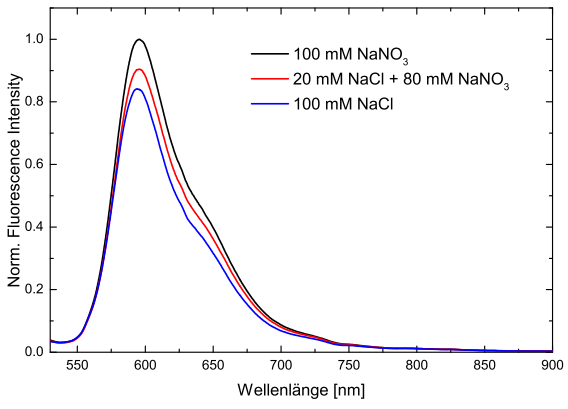

(b) Dichloro DAOTA$^+$

Figure 5.12: Determination of Chloride cross sensitivity of Dye **(2)** (left) and **(4)** (right) immobilised in D4 hydrogel (5 wt.%dye, 1 Mil layer thickness) in a MES buffer

As can be seen in figure 5.12, chloride ion concentration only has a small impact on the emission of the triangulenium dyes. The di-*N*-dodecyl DAOTA$^+$ (dye **(2)**) does not seem to undergo dynamic quenching through chloride ions.There is a small decrease in emission intensity of dye **(4)** by 16 % when going from a chloride free solution to a chloride concentration of 100 mM. Applying the Stern-Volmer equation (2.17), this results in a Stern-Volmer constant of $1.9\,\mathrm{M}^{-1}$. For comparison, the dynamic quenching constant of acridine with chloride ions is $9.5\,\mathrm{M}^{-1}$ [79], four times higher than the quenching constant of the dye at hand, lucigenin quenching is even efficient enough to enable chloride sensing, the quenching constant is $174\,\mathrm{M}^{-1}$ [80]. It is also interesting, that only dye **(4)** exhibits this decrease in fluorescence and dye **(2)**, which lacks a pH sensitive PET group does not. Maybe dye **(2)** is less affected by changes in chloride concentration due to location in the more hydrophobic domains of the D4 hydrogel. Dye **(4)** on the other hand is more hydrophilic, since it has only one hydrophobic dodecyl chain. This could lead to location in the more polar domains and therefore result in higher influence of chloride on dye**(4)**.
For further investigation of the dye the slight chloride dependence was neglected in a first approximation characterisation.

5.3.3 pH Calibrations

Fluorescence Intensity pH Calibration

Data obtained by fluorescence intensity pH calibration was evaluated by applying a sigmoidal Boltzmann fit as described in equaiton 5.1.

$$y = A_2 + \frac{A_1 - A_2}{1 + e^{\left(\frac{x - x_0}{d_x}\right)}} \tag{5.1}$$

A_1 is the initial, A_2 the final value, $x_[0]$ denotes the curve's center while d_x is a constant relating to the curve's slope. The spectra were normalised with regard to the highest intensity value among all conditions (pH, ionic strength) for one sensing environment (D4, D1, pHEMA, solution).

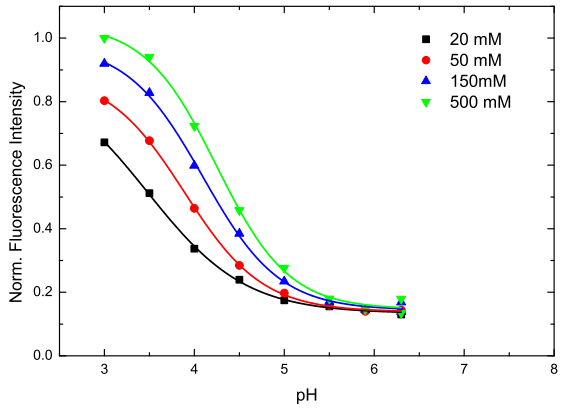

(a) 5 wt% of dye **(4)** in D4

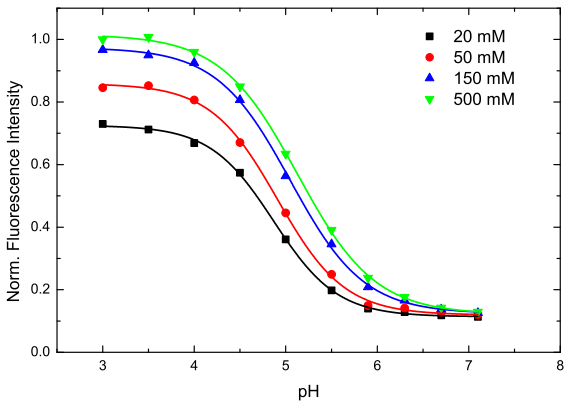

(b) 1 wt% of dye **(4)** in D4

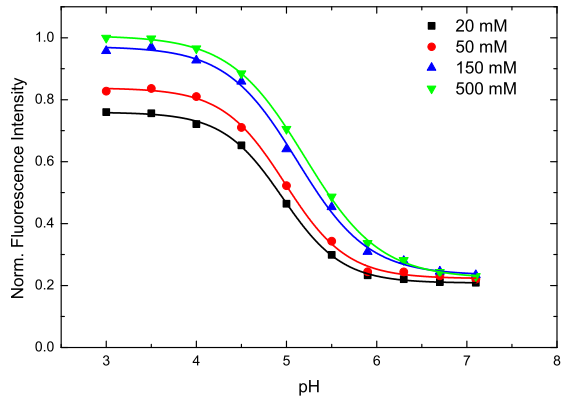

(c) 1 wt% of dye **(4)** in D1

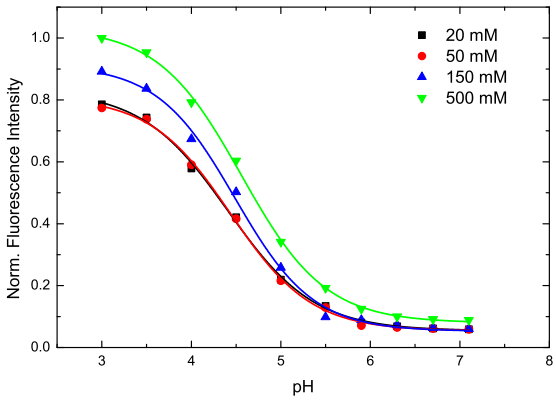

(d) 1 wt% of dye **(4)** in pHEMA

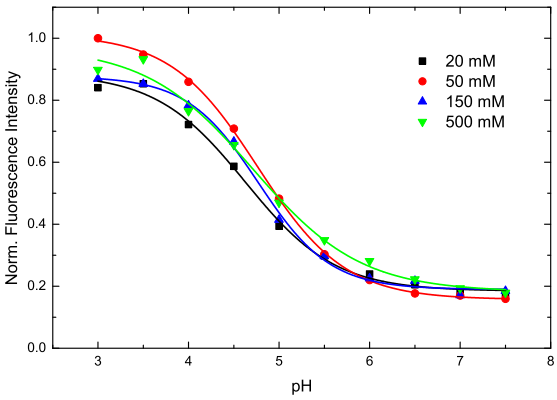

(e) 5 wt% of dye **(4)** in solution (A=0.1)

Figure 5.13: Fluorescence Intensity pH Calibration of Dye **(4)** 5 wt.% in D4 (a), 1 wt.% in D4, D1 and pHEMA (b, c, d) and in a solution with an absorbance of 0.1(e); buffer concentration 10 mM, ionic strengths of 20, 50, 150 and 500 mM adjusted with NaCl, excitation 485 nm, emission 610 nm

Figure 5.13 shows the fluorescence intensity pH calibration of dye **(4)** in solution and sensing layers at constant buffer concentration of 10 mM and four different ionic strengths (20, 50, 150

and 500 mM), set by addition of NaCl.
As can be seen in figures 5.13, the fluorescence intensity decreases in a sigmoidal way with increasing pH. In all cases the fluorescence intensity was greater at higher ionic strengths at low pH values while it was almost the same at high pH values. In solution on the other hand,this trend was not be observed. The residual signal strength at basic pH values is probably scattered light from the excitation source in the microplate reader, since in emission spectra measured at the fluorometer, no residual fluorescence intensity was observed (figure 5.8).

Table 5.3: Apparent pK_a values of dye **(4)** in solution and sensing layers obtained by fluorescence intensity calibration

	20 mM	50 mM	150 mM	500 mM
5 wt.% in D4	3.48	3.89	4.09	4.25
1 wt.% in D4	4.87	4.91	5.05	5.13
1 wt.% in D1	4.96	4.98	5.12	5.20
1 wt.% in pHEMA	4.41	4.44	4.49	4.56
solution	4.63	4.76	4.77	4.72

As can be seen in table 5.3, the ionic strength dependence of the apparent pK_a values is lower in pHEMA when compared to the more hydrophobic D1 and D4 matrices. In solution a trend of increasing pK_a higher ionic strength can be observed for ionic strengths of 20 - 150 mM. The deviation of the pK_a obtained by calibation in 500 mM buffer may be explained by dynamic chloride quenching surpassing the effect of ionic strength. In sensing layers, the increase in fluorescence intensity at high ionic strength of the measurement solution overcomes the slight decrease due to dynamic quenching by chloride as observed in section 5.3.2. For this reason it can be assumed that the cross talk to chloride is negligible in sensing layers, especially compared to the influence of ionic strength. In sensing layers the apparent pK_a rises with increasing ionic strength. The reason for this trend is that at higher ion concentration, a more polar environment is provided for the dye immobilised in the matrix. The positively charged, protonated form of the dye is better stabilised and the apparent pK_a increased.

To further investigate the trend of increasing fluorescence intensity with increasing ionic strength, fluorescence intensity was recorded at three pH values (3.5, 5 and 6.7) and all four ionic strengths with three sensor spots. The results shown in figure 5.14 indicate that the intensity difference is most likely due to some systematic trend within the sensing spots due to the measurement setup (figure 4.15) than to a difference in ionic strength. The biggest difference with this method was seen at pH 5, which is within the transition range of the dye and has influence on the pK_a of the dye as discussed above. The initial and final fluorescence intensities should remain approximately the same at all ionic strengths.

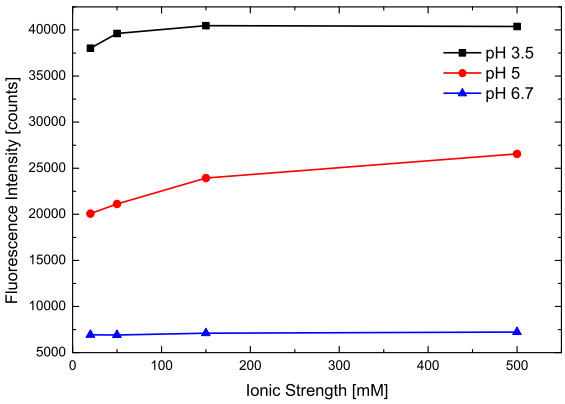

(a) a) 1 wt.% of dye **(4)** in D4

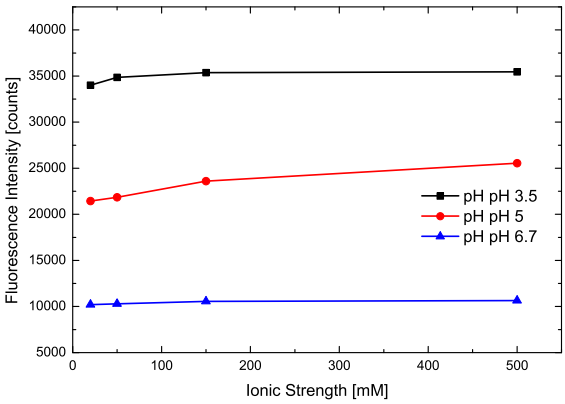

(b) 1 wt.% of dye **(4)** in D1

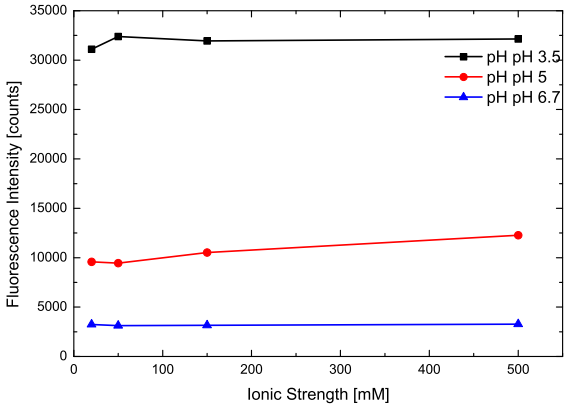

(c) 1 wt.% of dye **(4)** in pHEMA

Figure 5.14: Influence of ionic strength on the fluorescence intensity of sensing spots

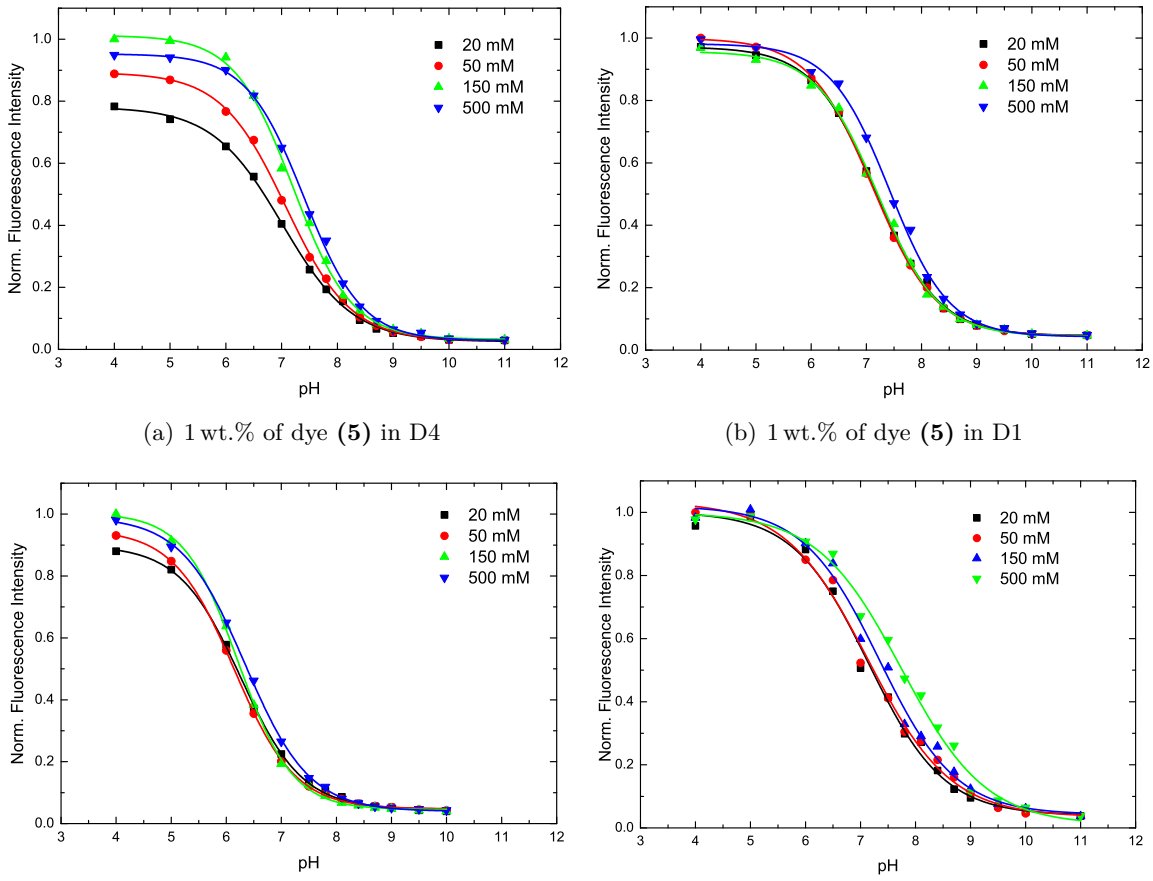

(a) 1 wt.% of dye **(5)** in D4

(b) 1 wt.% of dye **(5)** in D1

(c) 1 wt.% of dye **(5)** in pHEMA

(d) 1 wt.% of dye **(5)** in solution

Figure 5.15: Fluorescence Intensity pH Calibration of Dye **(5)** 1 wt.% in D4, D1 and pHEMA (a, b, c) and in a solution with an absorbance of 0.1(d); buffer concentration 10 mM, ionic strength 20, 50, 150 and 500 mM adjusted with NaCl, excitation 485 nm, emission 610 nm

With dye **(5)** the difference in fluorescence intensity of the protonated dye in different ionic strengths is significantly less pronounced, up to the point where in pHEMA there is hardly any difference at all and in D1 only the apparent pK_a at 500 mM ionic strength is significantly different from the other determined pK_a values. Also the background in this case is much lower than with dye **(4)**. As with dye **(4)**, the pK_a values in pHEMA are the lowest while those in D1 and D4 are rather similar and the values in solution are scattered statistically. The reason for this statistic scattering could be that here the values are determined by the concentration of the solution and therefore by the volumes of dye stock solution and buffer transferred to the microtiterplate. As such low concentrations and volumes are used, even small deviations can visibly influence the resulting fluorescence intensity.

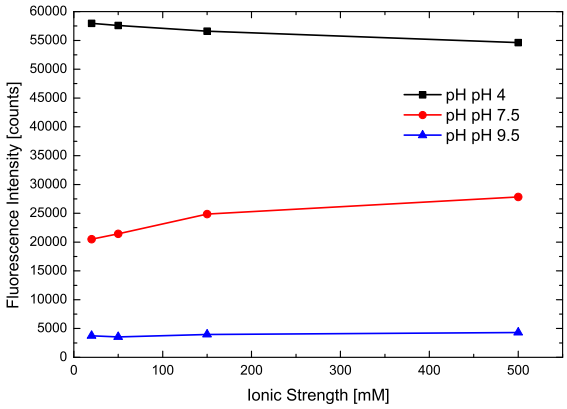

Figure 5.16: Influence of ionic strength on the fluorescence intensity of sensing spots

Table 5.4: Apparent pK_a values of dye **(5)** in solution and sensing layers obtained by fluorescence intensity calibration

	20 mM	50 mM	150 mM	500 mM
1 wt.% in D4	7.01	7.08	7.21	7.40
1 wt.% in D1	7.17	7.11	7.20	7.42
1 wt.% in pHEMA	6.26	6.14	6.21	6.34
solution	7.15	7.13	7.35	7.74

As expected, the pK_a values of dye **(5)** were significantly higher than those of dye **(4)**. The dyes are very similar in structure, only one chlorine atom missing in dye **(5)** as compared to **(4)**. Since this chlorine atom is located in *para* position to the PET group however, its influence on the acidity of the hydroxy group is rather big.
A different issue is, that the pH determination of buffers with 500 mM ionic strength is not that reliable any more due to limitations of the pH electrode.

Again, the influence of ionic strength on three sensing spots was investigated at three pH values, this time only in D4 sensing layer (see figure 5.16). The results were similar as with dye **(4)**, the fluorescence intensity at low and high pH values being almost constant through all ionic strengths while a difference could be observed at transition range pH, corresponding to shift in pK_a with ionic strength.

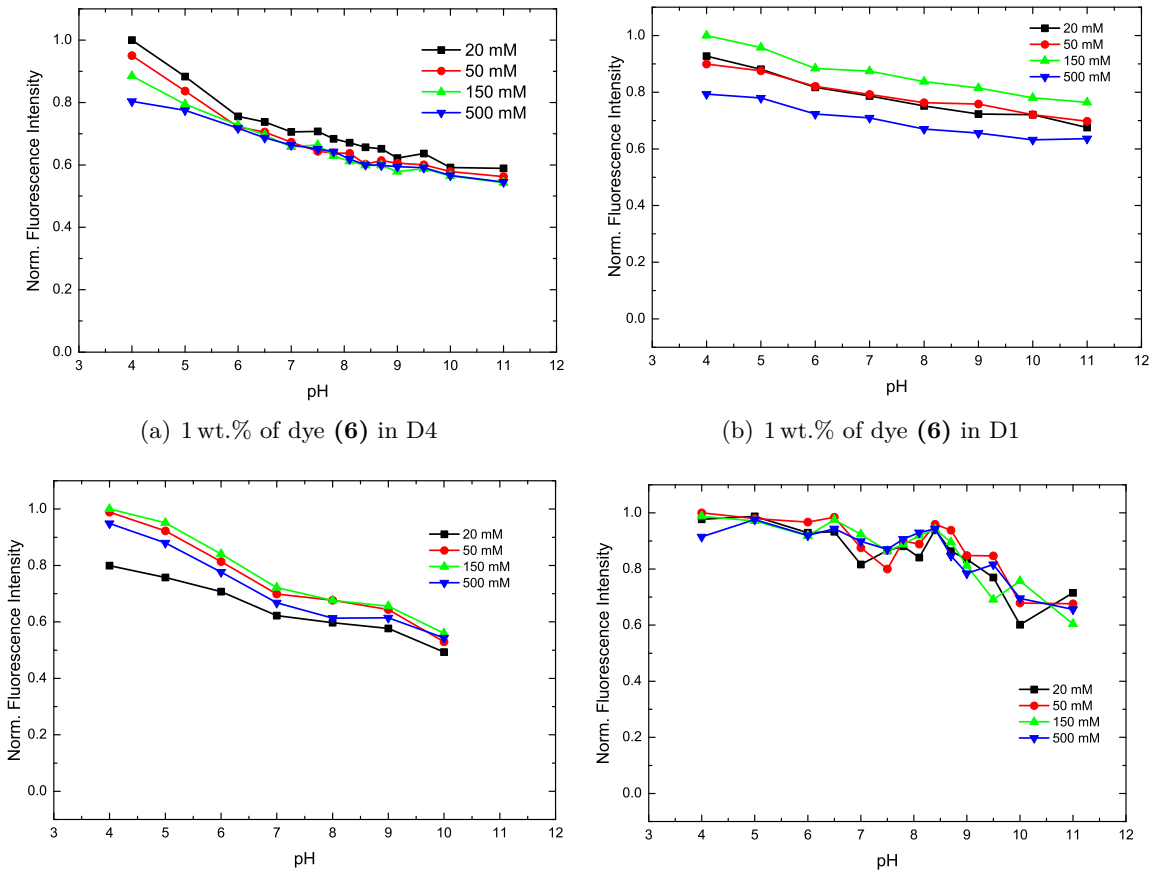

(a) 1 wt.% of dye **(6)** in D4

(b) 1 wt.% of dye **(6)** in D1

(c) 1 wt.% of dye **(6)** in pHEMA

(d) 1 wt.% of dye **(6)** in solution

Figure 5.17: Fluorescence Intensity pH Calibration of Dye **(6)** 1 wt.% in D4, D1 and pHEMA (a, b, c) and in a solution with an absorbance of 0.1(d); buffer concentration 10 mM, ionic strength 20, 50, 150 and 500 mM adapted with NaCl

Calibration of dye **(6)** did not yield evaluable curves. While fluorescence intensity dropped under 20 % in case of dye **(4)** and even under 10 % for dye **(5)**, the decrease in fluorescence intensity of dye **(6)** was less than 50 %. The real problem however, is the lack of an inflection point or inflection area from which an apparent pK_a value could be determined. The most unreliable data are in this case provided by the attempt to calibrate the dye in solution.

Fluorescence Decay Time pH Calibration

Fluorescence decay time is a much more favourable measurement parameter for optical sensing than fluorescence intensity. While in fluorescence intensity measurements the signal is influenced for example by fluctuations in the excitation light source, the sensitivity of the detector and dye loss due to leaching or photobleaching, fluorescence decay time measurements are essentially self-referenced. In pH sensing not many indicators exist that enable measurement of decay time in dependence of pH. Therefore, while fluorescence intensity measurement works fine

with pH sensitive DAOTA$^+$ dyes, determination of change in decay time with pH is much more interesting for possible sensing applications. The fluorescence decay curves deviated from monoexponential behaviour at higher pH values. For this reason, two methods of evaluation were applied. Since the curves could still be fitted biexponentially in good correlation, the average lifetime was calculated from the lifetimes and relative amplitudes of both lifetime components.

$$\tau_{mean} = \tau_{short} \cdot A_{short} + \tau_{long} \cdot A_{long} \tag{5.2}$$

Where A is the relative amplitude and τ the lifetime of the respective lifetime component, the subscripts determine if it refers to the long- or short-lifetime component.
The other method applied was chosen with possible applications in time gated fluorescence microscopy in mind. The first 1.5 ns after the maximum of the decay curve were cut off, after which the remaining curve could be fitted monoexponentially.
Dye **(6)** did not yield viable pH calibration curves since the lifetime did not change significantly with pH. The respective figure 9.53 can be found in chapter 9.

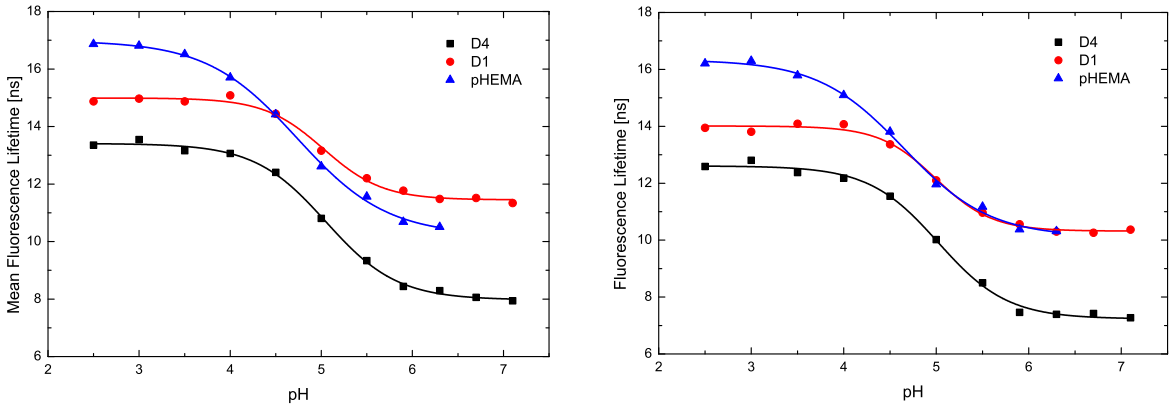

(a) Dye **(4)** biexponential fit

(b) Dye **(4)** monoexponential fit

Figure 5.18: Fluorescence lifetime pH calibration of dye **(4)** in D4, D1 and pHEMA fitted biexponentially (a) and monoexponentially (b); excitation at 485 nm, detection at 590 nm, buffer concentration 10 mM, ionic strength 150 mM adjusted with NaCl

Table 5.5: Apparent pK_a values of dye **(4)** in sensing layers obtained by fluorescence decay time calibration

	1 wt.% in D4	1 wt.% in D1	1 wt.% in pHEMA
Biexponential	5.05	5.02	4.73
Monoexponential	5.02	4.99	4.65

The apparent pK_a values obtained by fluorescence decay time calibration fit well with those obtained by fluorescence intensity calibration at the same ionic strength of 150 mM (see table

5.3). The apparent difference in decay times in figure 5.18 (a) and (b) is due to the data evaluation method.

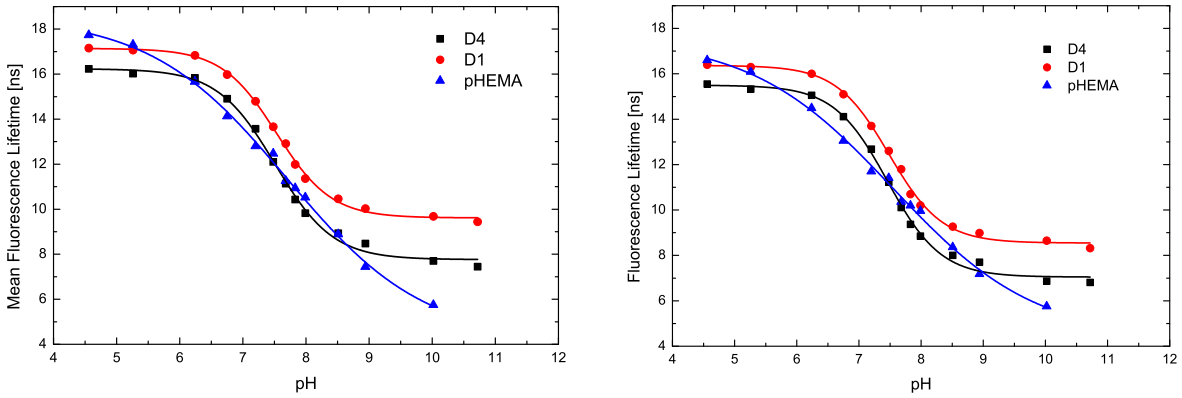

(a) Dye **(5)** biexponential fit

(b) Dye **(5)** monoexponential fit

Figure 5.19: Fluorescence lifetime pH calibration of dye **(5)** in D4, D1 and pHEMA fitted biexponentially (a) and monoexponentially (b); excitation at 485 nm, detection at 590 nm, buffer concentration 10 mM, ionic strength 150 mM adjusted with NaCl

Table 5.6: Apparent pK_a values of dye **(5)** in sensing layers obtained by fluorescence decay time calibration

	1 wt.% in D4	1 wt.% in D1	1 wt.% in pHEMA
Biexponential	7.51	7.53	7.70
Monoexponential	7.46	7.48	7.55

The apparent pK_a values obtained for dye **(5)** through fluorescence decay time calibration are between 0.2 and 0.3 pH units higher than those obtained by fluorescence intensity calibration. The difference between the values for the dye in pHEMA are even bigger. However the fluorescence decay time calibration in pHEMA is probably not reliable for dye **(5)** because the resulting curves are not really sigmoidal and the inflection point can only be approximated.

When measuring in solution, however, no decrease in lifetime with increasing pH can be observed, as seen in figure 5.20. Why that is the case cannot be said with certainty. A theory explaining the difference in lifetime behaviour between solution and matrix is excited state proton exchange, which will be further discussed in section 5.3.3.

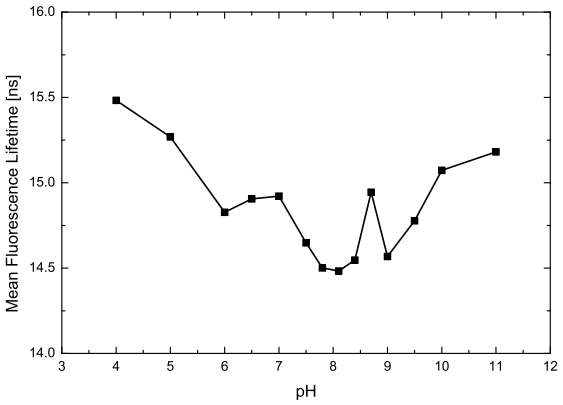

Figure 5.20: Fluorescence decay time pH calibration of dye**(5)** in solution with an absorbance of 0.1

Excited State Proton Exchange - Influence of Temperature and Buffer Concentration on Fluorescence Decay Calibration

It is striking that the fluorescence lifetime does not change with pH when the dye is in solution, but very much so, when the dye is immobilised in a polymer matrix. If PET is efficient, as seems to be the case when regarding figure 5.8, the dye is non-emissive in it's deprotonated state and lifetime is only determined by the protonated form, which displays a continuously long lifetime. The fact that in immobilisation matrices lifetime does decline with increasing pH is very beneficial for pH sensing applications. However, to be able to reliably predict sensing properties it is important to understand the reason for this different behaviour in solution as compared to sensing layers. A theory explaining the change in lifetime, especially the existence of two fractions of which one has a long and one a short lifetime, is excited state proton exchange. If the protonation/deprotonation kinetics in the excited state are within the timescale of the fluorescence lifetime, meaning $K_d^* \approx K_{de-ex}$ in figure 5.21. The dye would be excited in it's protonated form and a certain fraction would be deprotonated before it can undergo radiative relaxation. Orellana et al. reported this mechanism with Ru(II) complexes [21]. They distinguished between two limiting siutations: *fast* and *slow* proton exchange (with respect to decay rates). The fact that dyes **(4)** and **(5)** showed two lifetime components that depended

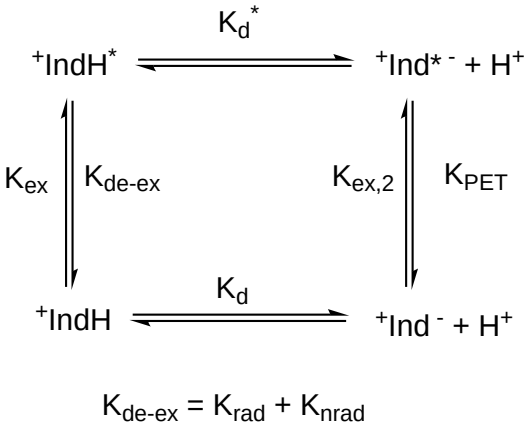

Figure 5.21: Excitation, proton exchange and de-excitation processes and their corresponding velocity constants

on pH as well as changing proportions of those components depending on pH indicates an intermediate between both limiting situations.
To determine, if excited state proton exchange does actually happen, pH dependence of fluorescence lifetime of dye **(5)** 1 wt.% in D4 was investigated at different temperatures and different buffer concentrations. The results were fitted biexponentially and the average fluorescence lifetimes are displayed in figure 5.22.

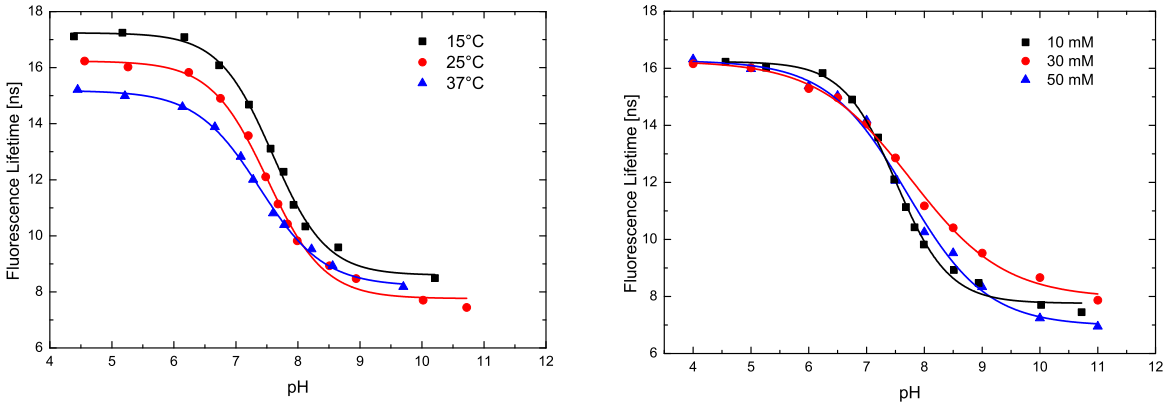

(a) Temperature dependence

(b) Buffer dependence

Figure 5.22: (a) Temperature and (b) buffer dependence of the pH calibration of dye **(5)** 1 wt.% in D4;
temperature dependence determined in 10 mM buffer with ionic strength of 150 mM adjusted with NaCl; buffer dependence determined in buffers with concentrations of 10, 30 and 50 mM and overall ionic strength of 150 mM adjusted with NaCl at 25°C

Table 5.7: pK'$_a$ dependence of 1 wt.% dye **(5)** in D4 on temperature and buffer concentration

Temperature	**15°C**	**25°C**	**37°C**
pK$_a$	7.59	7.51	7.39
Buffer Concentration	**10 mM**	**30 mM**	**50 mM**
pK$_a$	7.51	7.77	7.70

The apparent pK$_a$ decreases with increasing temperature as does the maximum fluorescence lifetime. Both of these phenomena would be expected even without excited state proton exchange. On the one hand pK'$_a$ values generally decrease when the temperature is increased, on the other hand de-excitation processes are faster at higher temperatures. With excited state proton exchange those phenomena would be amplified. From the data presented in figure 5.22 alone it cannot be determined for certain, if excited state deprotonation takes place. If excite state proton exchange takes place, deprotonation will be facilitated by buffer anions like phosphate

and higher buffer concentration will lead to a shift in pK'$_a$ values. When changing the buffer concentration, no clear trend concerning the pH calibration can be detected. Also there are still two lifetime components which change with pH as do their respective preexponential factors.

Change in fluorescence lifetime with pH only occurs when the dye is immobilised in a hydrogel matrix or in nanoparticles. This behaviour is not easy to explain by excited state proton exchange. If excited state deprotonation takes place, the behaviour of the dye in hydrogel would present an intermediate case between the two limiting cases of very fast/very slow proton exchange where two lifetime domains can be observed that change with pH as does their respective preexponential factor. A possible explanation for lack of excited state proton exchange in solution considers the effect of dye immobilisation on conformational change of the dye. In solution, the dye molecules, more precisely the PET group can freely rotate around the N-C bond. It could be more or less coplanar with the triangulenium structure, leading to different degrees of conjugation, but because of constant conformational change due to high mobility, the overall structure would be an average between all possible configurations. Immobilisation in a polymer matrix leads to a significant decrease in mobility. In consequence, a certain share of the dye would be present in a configuration very beneficial for excited state deprotonation. This share will then be subject to excited state proton exchange equilibrium and be represented by the short lifetime component in the decay curves.

5.4 Nanoparticles

For measurements in tissues nanoparticles are a powerful tool. Positively charged nanoparticles like from RL-100 polymer even penetrate cell walls thus enabling intracellular measurements. For this reason, nanoparticles were prepared of dyes **(4)** and **(5)** in RL-100 and PMMA-MA (only dye **(5)**). The alternative matrix, PMMA-MA was chosen to compare the behaviour of the dye in differently charged environments (RL-100 positive, PMMA-MA negative). Furthermore, it was expected that the pK'$_a$ decreases in positively charged RL-100 particles and increases in negatively charged PMMA-MA particles. This prediction was based on the fact that the protonated dyes are positively charged, a state that is unfavourable in the positive environment of RL-100 but very favourable in the negative PMMA-MA particles, influencing protonation equilibria .

Fluorescence Intensity Calibration of Nanoparticles

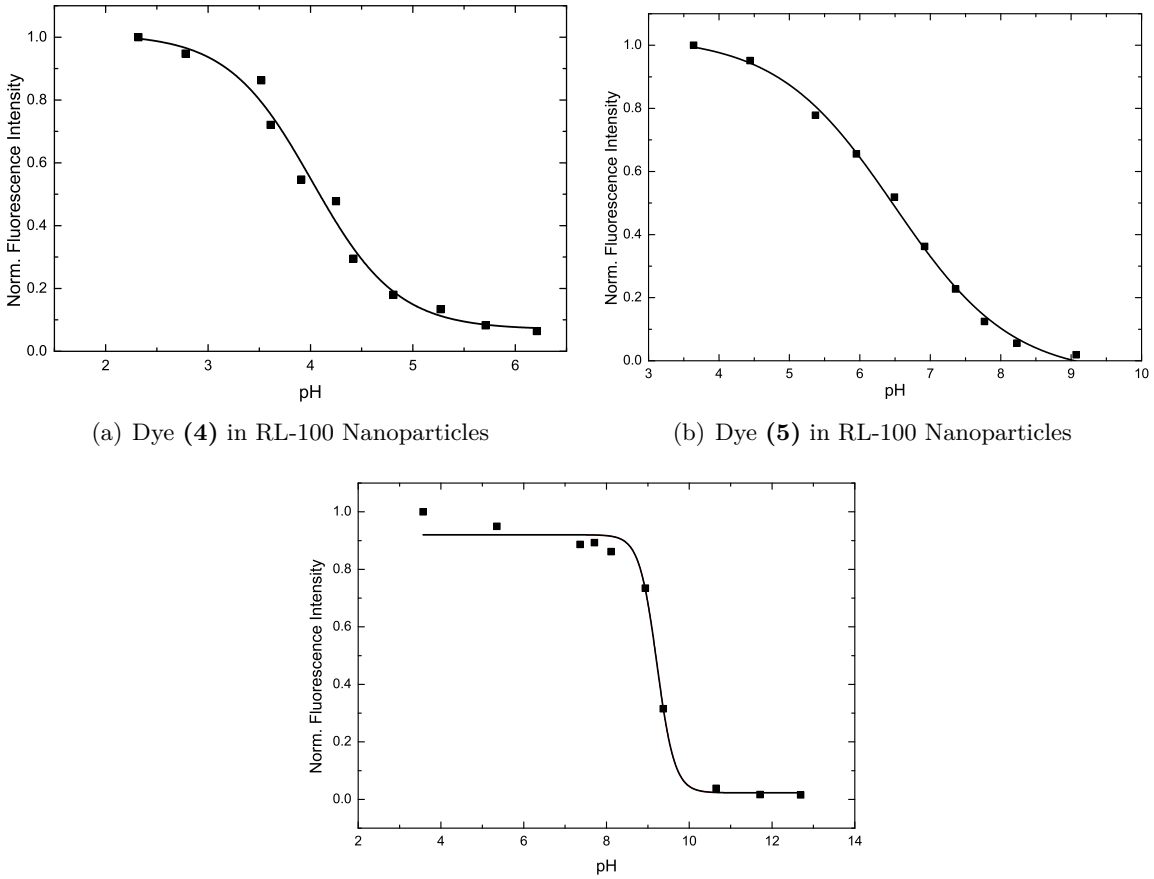

(a) Dye **(4)** in RL-100 Nanoparticles

(b) Dye **(5)** in RL-100 Nanoparticles

(c) Dye **(5)** in PMMA-MA Nanoparticles

Figure 5.23: Fluorescence intensity pH calibration of dyes **(4)** 0.75 wt.% in RL-100 and **(5)** 0.75 wt.% in RL-100 and PMMA-MA nanoparticles; buffer concentration 10 mM, ionic strength 150 mM adjusted with NaCl

Table 5.8: Apparent pK_a values of dyes **(4)** and **(5)** in RL-100 and PMMA-MA nanoparticle dispersions obtained by fluorescence intensity calibration

	Dye **(4)** in RL-100	Dye **(5)** in RL-100	Dye **(5)** in PMMA-MA
pK'_a	4.02	6.48	9.22

As expected, the pK_a of dyes **(4)** **(5)** was shifted to lower values in the positively charged RL-100 particles and that of dye **(5)** to higher values in the negatively charged PMMA-MA environment. With dye **(5)**, the correlation for the sigmoidal fit was much better in case of the RL-100 particles. It has to be considered, that at such high pH values as in the PMMA-MA calibration, OH^- attack at the central carbon can also lead to quenching of fluorescence by distortion of the planarity of the triangulenium system as was also reported for $TOTA^+$ [62]. Such a rapid

change and narrow transition range may also hint at aggregation of the nanoparticles in basic environment. This theory is supported by the fact that after several hours of resting, a cloudy precipitate could be observed in the nanoparticle-buffer-dispersions.

Fluorescence Decay Time Calibration of Nanoparticles

As usual, decay time was fitted two ways: monoexponentially while cutting off the first 1.5 ns of the decay curve and biexponentially. The resulting calibration curves are very similar in both methods, the resulting lifetimes in monoexponential fitting being slightly shorter due to the data evaluation strategy.

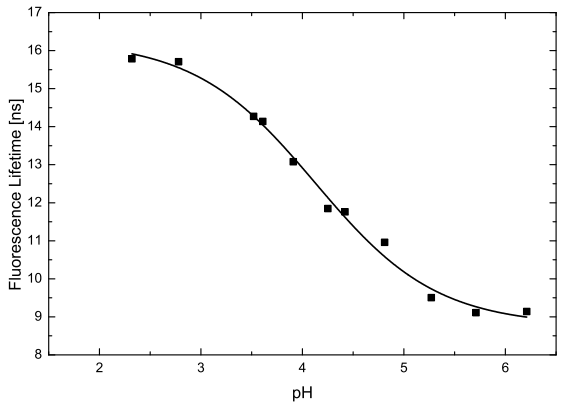

(a) Dye **(4)** in RL-100 Nanoparticles, monoexponential fit

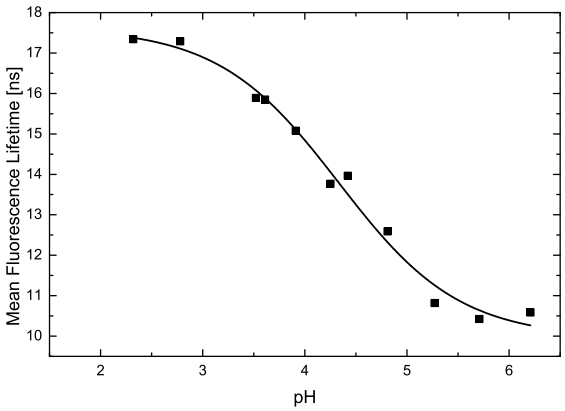

(b) Dye **(4)** in RL-100 Nanoparticles, biexponential fit

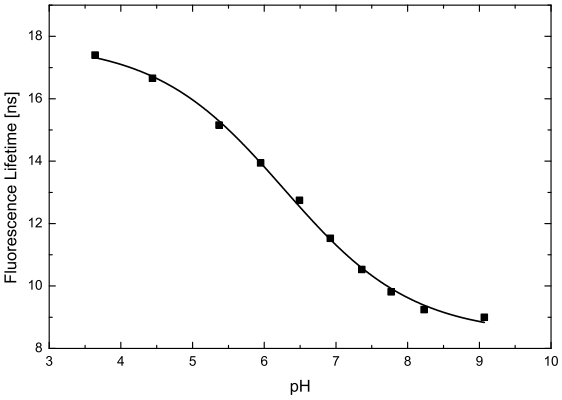

(c) Dye **(5)** in RL-100 Nanoparticles, monoexponential fit

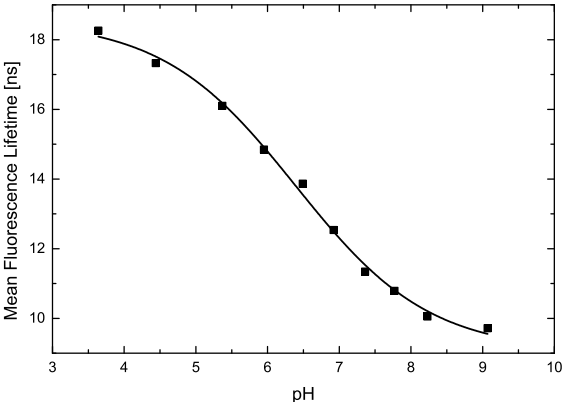

(d) Dye **(5)** in RL-100 Nanoparticles, biexponential fit

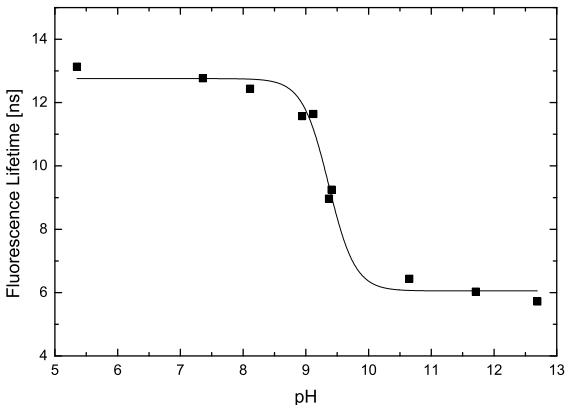

(e) Dye **(5)** in PMMA-MA Nanoparticles, monoexponential fit

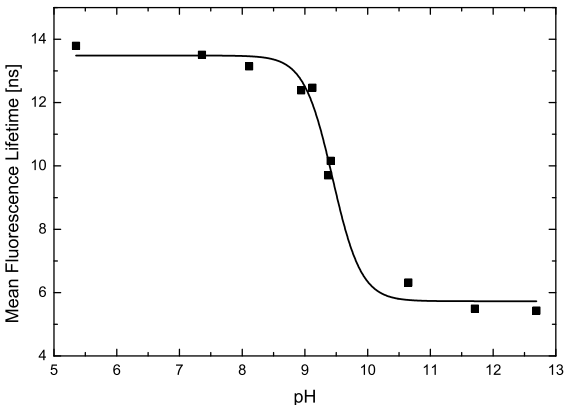

(f) Dye **(5)** in PMMA-MA Nanoparticles, biexponential fit

Figure 5.24: Fluorescence decay time pH calibration of dye **(4)** 0.75 wt.% in RL-100 and dye **(5)** 0.75 wt.% in RL-100 and PMMA-MA nanoparticles; buffer concentration 10 mM, ionic strength 150 mM adjusted with NaCl

Table 5.9: Apparent pK_a values of dyes **(4)** and **(5)** in RL-100 and PMMA-MA nanoparticles layers obtained via fluorescence decay time measurement

	Dye **(4)** in RL-100	Dye **(5)** in RL-100	Dye **(5)** in PMMA-MA
monoexponential	4.13	6.27	9.36
biexponential	4.33	6.39	9.44
intensity calibration	4.02	6.48	9.22

Again, calibration curves of dye **(4)** in PMMA-MA display a very narrow transition range explained probably by nanoparticle aggregation. As in all cases before, the pK_a values for the biexponential fit are slightly higher, which may also be due to the data evaluation method. Since this trend is consistent, calibrations should not be compromised by it.
The fact that significant pH dependent change in decay time can be achieved in nanoparticles further qualifies the $DAOTA^+$ dyes for possible applications in FLIM measurements. The mono- and dichloro $DAOTA^+$ dyes in RL-100 complement each other in terms of dynamic pH range, together covering an area from pH 3 to almost pH 8. In this area, both the physiological pH range as well as pH range typical for more acidic cell components like lysosomes are covered.[81]

6 Conclusion and Outlook

In this thesis a new class of pH indicator dyes based on diazaoxatriangulenes was synthesised and characterised. The PET-group-modified DAOTA$^+$ dyes retained the favourable long fluorescence lifetimes known for non-pH-sensitive triangulenes while displaying excellent brightness and long-wavelength excitation/emission. The stability of the dyes in sensing layers proved to be good, just as the photostability, which much better than that of rhodamine 101 and similar to the extremely photostable Marolex® Fluorescent Red G. Design of nanoparticles of RL-100 and PMMA-MA was successful. Furthermore, pH calibration could be conducted not only by measuring fluorescence intensity but also fluorescence decay time showed pH dependent behaviour for dye immobilised in sensing layers and in nanoparticles. Altogether these properties might make PET-functionalized DAOTA$^+$ dyes promising candidates for lifetime-based pH sensing and thereby provide a powerful tool for optical pH sensing in biological samples, even for intracellular measurements. As triangulenium dyes have already been used in time gated detection of cellular components [12] , time gated pH sensing is the next logical step in application of pH sensitive DAOTA$^+$ dyes. Also the excitation and emission in the red part of the spectrum is favourable for biological applications due to lack of absorption/autofluorescence of cell components in this region.
The success in designing nanoparticles containing DAOTA$^+$ dyes **(4)** and **(5)** is a promising step towards intracellular- and FLIM measurements. For this purpose, the cell permeability and biocompatibility have to be studied closely. If it can be affirmed that nanoparticles containing pH sensitive DAOTA$^+$ dyes are biocompatible, pH sensing in living cells would be possible with comparable ease of instrumentation and without the need of external referencing.
While it could be proven, that different phenol-moieties can be used to tune the apparent pK_a value of the indicator, an amine based PET group (dye **(6)**) showed insufficient PET efficiency for use as a pH indicator. It is likely that other amine-containing PET groups will not yield sufficient quenching either.

For future research it will be of immense importance to verify if the change of decay time with pH when immobilizing the dye in a hydrogel matrix is due to excited state proton exchange. For this a further investigation of the influence of buffer type on the decay time could be employed by calibrating in different buffers so as to prove or disprove the excited state proton exchange theory.
A different approach at pH sensing based on DAOTA$^+$ dyes is employing the FRET principle. For this application the dye would be equipped with a linker, for example as in dye **(3)**. The primary

amine linker can then be coupled with a carboxylic acid residue of e.g. a triphenylmethane dye, which will act as an energy acceptor, the absorption of its deprotonated form overlapping with the $DAOTA^+$ emission. Thus emission will be quenched when the triphenylmethane dye is deprotonated. The pK_a of such a diade can be easily tuned via choosing a triphenylmethane dye with appropriate substituents.
Dye **(3)** could also be used for covalent coupling with a polymer matrix or onto a solid support such as silica beads. In this case coupling of the final dye to e.g. a crosslinked polymer might be challenging due to the low solubility of the dye in many solvents as well as the steric hindrance the rigid triangulenium structure poses. If on the other hand the coupling process is conducted with an intermediate product (e.g. the quinolinacridinium), the polymer has to be stable under the drastic reaction conditions of the last ring closing step. For this purpose, covalent linking to organically modified silicate beads should pose a viable alternative, since they are likely to withstand the conditions applied during the oxygen-ring closing reaction.

7 References

1. Dobson, G. P., Yamamoto, E. & Hochachka, P. W. Phosphofructokinase control in muscle: nature and reversal of pH-dependent ATP inhibition. *American Journal of Physiology - Regulatory, Integrative and Comparative Physiology* **250,** R71 (Jan. 1, 1986).
2. Winslow, R. M., Samaja, M., Winslow, N. J., Rossi-Bernardi, L. & Shrager, R. I. Simulation of continuous blood O2 equilibrium curve over physiological pH, DPG, and Pco2 range. *Journal of Applied Physiology* **54,** 524 (Feb. 1, 1983).
3. Schindler, D. W. Effects of acid rain on freshwater ecosystems. *Science(Washington),* 149–157 (1988).
4. Caldeira, K. & Wickett, M. E. Oceanography: Anthropogenic carbon and ocean pH. *Nature* **425,** 365–365 (Sept. 25, 2003).
5. Kleypas, J. A. Geochemical Consequences of Increased Atmospheric Carbon Dioxide on Coral Reefs. *Science* **284,** 118–120 (Apr. 2, 1999).
6. Riebesell, U., Zondervan, I., Rost, B., Tortell, P. D., Zeebe, R. E. & Morel, F. M. M. Reduced calcification of marine plankton in response to increased atmospheric CO2. *Nature* **407,** 364–367 (Sept. 21, 2000).
7. McDonagh, C., Burke, C. S. & MacCraith, B. D. Optical Chemical Sensors. *Chemical Reviews* **108,** 400–422 (Feb. 2008).
8. Mohr, G. J. & Wolfbeis, O. S. Optical sensors for a wide pH range based on azo dyes immobilized on a novel support. *Analytica Chimica Acta* **292,** 41–48 (June 1994).
9. Han, J. & Burgess, K. Fluorescent Indicators for Intracellular pH. *Chemical Reviews* **110,** 2709–2728 (May 12, 2010).
10. Ghisla, S., Massey, V., Lhoste, J.-M. & Mayhew, S. G. Fluorescence and optical characteristics of reduced flavines and flavoproteins. *Biochemistry* **13,** 589–597 (Jan. 1974).
11. Laursen, B. W. & Krebs, F. C. Synthesis, Structure, and Properties of Azatriangulenium Salts. *Chemistry - A European Journal* **7,** 1773 –1783 (Mar. 23, 2001).
12. Rich, R. M., Stankowska, D. L., Maliwal, B. P., Sørensen, T. J., Laursen, B. W., Krishnamoorthy, R. R., Gryczynski, Z., Borejdo, J., Gryczynski, I. & Fudala, R. Elimination of autofluorescence background from fluorescence tissue images by use of time-gated detection and the AzaDiOxaTriAngulenium (ADOTA) fluorophore. *Analytical and Bioanalytical Chemistry* **405,** 2065–2075 (Feb. 2013).

13. Westerlund, F., Hildebrandt, C., Sørensen, T. & Laursen, B. Trihydroxytrioxatriangulene-An Extended Fluorescein and a Ratiometric pH Sensor. *Chemistry - A European Journal* **16,** 2992–2996 (Mar. 8, 2010).

14. Lakowicz, J. R. *Principles of fluorescence spectroscopy* 3rd ed. 954 pp. (Springer, New York, 2006).

15. Valeur, B. & Wiley InterScience (Online service). *Molecular fluorescence: principles and applications* OCLC: 53986221 (Wiley-VCH, New York, 2001).

16. Jablonski, A. Über den Mechanismus der Photolumineszenz von Farbstoffphosphoren. *Zeitschrift für Physik* **94,** 38–46 (Jan. 1935).

17. Mueller, B. J. *Covalent Linkage of pi-Extended Pt(II)-Porphyrins to Silicone Matrices A Convenient Way to Obtain Optical Trace Oxygen Sensors* Master Thesis (TU Graz, Graz, Feb. 2014). 130 pp.

18. Kasha, M. Characterization of electronic transitions in complex molecules. *Discussions of the Faraday Society* **9,** 14 (1950).

19. Stokes, G. On the Change of Refrangibility of Light. *Philosophical Transactions of the Royal Society of London* **142,** 463–562 (1852).

20. Ireland, J. & Wyatt, P. in *Advances in Physical Organic Chemistry* 131–221 (Elsevier, 1976).

21. Tormo, L., Bustamante, N., Colmenarejo, G. & Orellana, G. Can Luminescent Ru(II) Polypyridyl Dyes Measure pH Directly? *Analytical Chemistry* **82,** 5195–5204 (June 15, 2010).

22. Gründler, P. *Chemische Sensoren: eine Einführung für Naturwissenschaftler und Ingenieure ; mit 27 Tabellen* Softcover. OCLC: 820457027. 295 pp. (Springer, Berlin, 2012).

23. Wolfbeis, O. S. Chemical sensors - survey and trends. *Fresenius' Journal of Analytical Chemistry* **337,** 522–527 (1990).

24. Hulanicki, A., Glab, S. & Ingman, F. Chemical sensors: definitions and classification. *Pure and Applied Chemistry* **63.** doi:10.1351/pac199163091247 (Jan. 1, 1991).

25. Eggins, B. R. *Chemical sensors and biosensors* 273 pp. (J. Wiley, Chichester ; Hoboken, NJ, 2002).

26. Wolfbeis, O. S. Fiber-Optic Chemical Sensors and Biosensors. *Analytical Chemistry* **80,** 4269–4283 (June 2008).

27. Amao, Y. Probes and Polymers for Optical Sensing of Oxygen. *Microchimica Acta* **143,** 1–12 (Sept. 1, 2003).

28. Wolfbeis, O. S. Materials for fluorescence-based optical chemical sensors. *Journal of Materials Chemistry* **15,** 2657 (2005).

29. Buenger, D., Topuz, F. & Groll, J. Hydrogels in sensing applications. *Progress in Polymer Science* **37,** 1678–1719 (Dec. 2012).

30. Passos, M. F., Dias, D. R. C., Bastos, G. N. T., Jardini, A. L., Benatti, A. C. B., Dias, C. G.B. T. & Maciel Filho, R. pHEMA hydrogels: Synthesis, kinetics and in vitro tests. *Journal of Thermal Analysis and Calorimetry* **125,** 361–368 (July 2016).

31. Silvestri, B., Luciani, G., Costantini, A., Tescione, F., Branda, F. & Pezzella, A. In-situ sol-gel synthesis and characterization of bioactive pHEMA/SiO 2 blend hybrids. *Journal of Biomedical Materials Research Part B: Applied Biomaterials* **89B,** 369–378 (May 2009).

32. Davis, P. A., Huang, S. L., Nicolais, L. & Ambrosio, L. in *High Performance Biomaterials* 343–368 (Technomic, 1991).

33. Kirkbright, G. F., Narayanaswamy, R. & Welti, N. A. Fibre-optic pH probe based on the use of an immobilised colorimetric indicator. *The Analyst* **109,** 1025 (1984).

34. Edmonds, T. & Ross, I. Low-cost Fibre Optic Chemical Sensors. *Analytical Proceedings,* 206–207 (July 1985).

35. Peterson, J. I., Goldstein, S. R. & Fitzgerald, R. V. Fiber Optic pH Probe for Physiological Use. *Analytical Chemistry,* 864–869 (1980).

36. Offenbacher, H., Wolfbeis, O. S. & Fürlinger, E. Fluorescence optical sensors for continuous determination of near-neutral pH values. *Sensors and Actuators* **9,** 73–84 (Feb. 1986).

37. Whitaker, J. E., Haugland, R. P. & Prendergast, F. G. Spectral and photophysical studies of benzo[c]xanthene dyes: Dual emission pH sensors. *Analytical Biochemistry* **194,** 330–344 (May 1991).

38. Wolfbeis, O. S., Fürlinger, E., Kroneis, H. & Marsoner, H. Fluorimetric analysis: 1. Untersuchung von Fluorescenzindicatoren zur Messung von pH-Werten im Neutralbereich. *Fresenius' Zeitschrift für Analytische Chemie* **314,** 119–124 (1983).

39. Zhujun, Z. & Seitz, W. A fluorescence sensor for quantifying pH in the range from 6.5 to 8.5. *Analytica Chimica Acta* **160,** 47–55 (1984).

40. Niu, C.-G., Zeng, G.-M., Chen, L.-X., Shen, G.-L. & Yu, R.-Q. Proton "off-on" behaviour of methylpiperazinyl derivative of naphthalimide: a pH sensor based on fluorescence enhancement. *The Analyst* **129,** 20–24 (2004).

41. Li, Z.-Z., Niu, C.-G., Zeng, G.-M., Liu, Y.-G., Gao, P.-F., Huang, G.-H. & Mao, Y.-A. A novel fluorescence ratiometric pH sensor based on covalently immobilized piperazinyl-1,8-napthalimide and benzothioxanthene. *Sensors and Actuators B: Chemical* **114,** 308–315 (Mar. 2006).

42. Borisov, S. M., Gatterer, K. & Klimant, I. Red light-excitable dual lifetime referenced optical pH sensors with intrinsic temperature compensation. *The Analyst* **135,** 1711 (2010).

43. Killoran, J., McDonnell, S. O., Gallagher, J. F. & O'Shea, D. F. A substituted BF2 -chelated tetraarylazadipyrromethene as an intrinsic dual chemosensor in the 650–850 nm spectral range. *New J. Chem.* **32,** 483–489 (2008).

44. Murtagh, J., Frimannsson, D. O. & O'Shea, D. F. Azide Conjugatable and pH Responsive Near-Infrared Fluorescent Imaging Probes. *Organic Letters* **11,** 5386–5389 (Dec. 3, 2009).

45. Jokic, T., Borisov, S. M., Saf, R., Nielsen, D. A., Kühl, M. & Klimant, I. Highly Photostable Near-Infrared Fluorescent pH Indicators and Sensors Based on BF2 -Chelated Tetraarylazadipyrromethene Dyes. *Analytical Chemistry* **84,** 6723–6730 (Aug. 7, 2012).

46. Klimant, I., Huber, C., Liebsch, G., Neurauter, G., Stangelmayer, A. & Wolfbeis, O. S. in *New Trends in Fluorescence Spectroscopy* 1st ed., 257–274 (Springer, 2001).

47. Liebsch, G., Klimant, I., Krause, C. & Wolfbeis, O. Fluorescent Imaging of pH with Optical Sensors Using Time Domain Dual Lifetime Referencing. *Analytical Chemistry* **73,** 4354–4363 (Sept. 2001).

48. Szmacinski, H. & Lakowicz, J. R. Optical measurements of pH using fluorescence lifetimes and phase-modulation fluorometry. *Analytical Chemistry* **65,** 1668–1674 (July 1993).

49. Lin, H.-J., Szmacinski, H. & Lakowicz, J. R. Lifetime-Based pH Sensors: Indicators for Acidic Environments. *Analytical Biochemistry* **269,** 162–167 (Apr. 1999).

50. Aigner, D., Dmitriev, R. I., Borisov, S. M., Papkovsky, D. B. & Klimant, I. pH-sensitive perylene bisimide probes for live cell fluorescence lifetime imaging. *J. Mater. Chem. B* **2,** 6792–6801 (Aug. 7, 2014).

51. Draxler, S. & Lippitsch, M. E. pH sensors using fluorescence decay time. *Sensors and Actuators B: Chemical* **29,** 199–203 (Oct. 1995).

52. Lippitsch, M. E., Draxler, S. & Leiner, M. J. P. *Time-domain fluorescence methods as applied to pH sensing* in (ed Lieberman, R. A.) (Apr. 30, 1993), 202–209. doi:10.1117/12.143521.

53. Ryder, A. G., Power, S. & Glynn, T. J. Evaluation of Acridine in Nafion as a Fluorescence-Lifetime-Based pH Sensor. *Applied Spectroscopy* **57,** 73–79 (2003).

54. Orte, A., Alvarez-Pez, J. M. & Ruedas-Rama, M. J. Fluorescence Lifetime Imaging Microscopy for the Detection of Intracellular pH with Quantum Dot Nanosensors. *ACS Nano* **7,** 6387–6395 (July 23, 2013).

55. Chen, C., Zhang, P., Zhang, L., Gao, D., Gao, G., Yang, Y., Li, W., Gong, P. & Cai, L. Long-decay near-infrared-emitting doped quantum dots for lifetime-based in vivo pH imaging. *Chem. Commun.* **51,** 11162–11165 (2015).

56. Tang, R., Lee, H. & Achilefu, S. Induction of pH Sensitivity on the Fluorescence Lifetime of Quantum Dots by NIR Fluorescent Dyes. *Journal of the American Chemical Society* **134,** 4545–4548 (Mar. 14, 2012).

57. Clarke, Y., Xu, W., Demas, J. N. & DeGraff, B. A. Lifetime-Based pH Sensor System Based on a Polymer-Supported Ruthenium(II) Complex. *Analytical Chemistry* **72,** 3468–3475 (Aug. 2000).

58. Gon**c**alves, H. M., Maule, C. D., Jorge, P. A. & Esteves da Silva, J. C. Fiber optic lifetime pH sensing based on ruthenium(II) complexes with dicarboxybipyridine. *Analytica Chimica Acta* **626,** 62–70 (Sept. 2008).

59. Malins, C, Glever, H., Keyes, T., Vos, J., Dressick, W. & MacCraith, B. Sol–gel immobilised ruthenium(II) polypyridyl complexes as chemical transducers for optical pH sensing. *Sensors and Actuators B: Chemical* **67,** 89–95 (Aug. 2000).

60. Blair, S., Lowe, M. P., Mathieu, C. E., Parker, D., Senanayake, P. K. & Kataky, R. Narrow-Range Optical pH Sensors Based on Luminescent Europium and Terbium Complexes Immobilized in a Sol Gel Glass. *Inorganic Chemistry* **40,** 5860–5867 (Nov. 2001).

61. Bare, W. D., Mack, N. H., Xu, W., Demas, J. N. & DeGraff, B. A. Multicomponent Lifetime-Based pH Sensors Utilizing Constant-Lifetime Probes. *Analytical Chemistry* **74,** 2198–2209 (May 2002).

62. Martin, J. C. & Smith, R. G. Factors Influencing the Basicities of Triarylcarbinols. The Synthesis of Sesquixanthydrol. *Journal of the American Chemical Society* **86,** 2252–2256 (June 1964).

63. Dileesh, S. & Gopidas, K. Photophysical and electron transfer studies of a stable carbocation. *Chemical Physics Letters* **330,** 397–402 (Nov. 2000).

64. Reynisson, J., Schuster, G. B., Howerton, S. B., Williams, L. D., Barnett, R. N., Cleveland, C. L., Landman, U., Harrit, N. & Chaires, J. B. Intercalation of Trioxatriangulenium Ion in DNA: Binding, Electron Transfer, X-ray Crystallography, and Electronic Structure. *Journal of the American Chemical Society* **125,** 2072–2083 (Feb. 2003).

65. Laursen, B. W., Sorensen, T. J. &, V. Synthesis of Super Stable Triangulenium Dye. *The Journal of Organic Chemistry* **74,** 3183–3185 (Mar. 12, 2009).

66. Badri P., M., Rafal, F., Sangram, R., Rutika, K., Thomas J., S., Bo W., L., Zygmunt, G. & Ignacy, G. Long-Lived Bright Red Emitting Azaoxa-Triangulenium Fluorophores. *PLoS ONE* **8.** doi:10.1371/journal.pone.0063043 (May 7, 2013).

67. Bora, I., Bogh, S. A., Santella, M., Rosenberg, M., Sorensen, T. J. & Laursen, B. W. Azadioxatriangulenium: Synthesis and Photophysical Properties of Reactive Dyes for Bioconjugation: Azadioxatriangulenium. *European Journal of Organic Chemistry* **2015,** 6351–6358 (Oct. 2015).

68. Wallabregue, A., Moreau, D., Sherin, P., Moneva Lorente, P., Jarolimova, Z., Bakker, E., Vauthey, E., Gruenberg, J. & Lacour, J. Selective Imaging of Late Endosomes with a pH-Sensitive Diazaoxatriangulene Fluorescent Probe. *Journal of the American Chemical Society* **138,** 1752–1755 (Feb. 17, 2016).

69. Seybold, G. New perylene and violanthrone dyestuffs for fluorescent collectors. *Dyes and Pigments* **11,** 303–317 (1989).

70. Crosby, G. A. & Demas, J. N. Measurement of photoluminescence quantum yields. Review. *The Journal of Physical Chemistry* **75,** 991–1024 (Apr. 1971).

71. Dmitriev, R. I., Borisov, S. M., Kondrashina, A. V., Pakan, J. M. P., Anilkumar, U., Prehn, J. H. M., Zhdanov, A. V., McDermott, K. W., Klimant, I. & Papkovsky, D. B. Imaging oxygen in neural cell and tissue models by means of anionic cell-permeable phosphorescent nanoparticles. *Cellular and Molecular Life Sciences* **72,** 367–381 (Jan. 2015).

72. Fercher, A., Borisov, S. M., Zhdanov, A. V., Klimant, I. & Papkovsky, D. B. Intracellular O2 Sensing Probe Based on Cell-Penetrating Phosphorescent Nanoparticles. *ACS Nano* **5,** 5499–5508 (July 26, 2011).

73. Wittig, G. & Pockels, U. Über den Austausch von aromatisch gebundenem Brom gegen Lithium mittels Phenyl-lithiums. *Berichte der Deutschen Chemischen Gesellschaft* **72,** 89–92 (Jan. 11, 1939).

74. Laursen, B. W., Krebs, F. C., Nielsen, M. F., Bechgaard, K., Christensen, J. B. & Harrit, N. 2,6,10-Tris(dialkylamino)trioxatriangulenium Ions. Synthesis, Structure, and Properties of Exceptionally Stable Carbenium Ions. *Journal of the American Chemical Society* **120,** 12255–12263 (Dec. 1998).

75. Krebs, F. C., Laursen, B. W., Johannsen, I., Faldt, A., Bechgaard, K., Jacobsen, C. S., Thorup, N. & Boubekeur, K. The geometry and structural properties of the 4,8,12-trioxa-4,8,12,12c-tetrahydrodibenzo[cd,mn]pyrene system in the cationic state. Structures of a planar organic cation with various monovalent and divalent anions. *Acta Crystallographica Section B Structural Science* **55,** 410–423 (June 1, 1999).

76. Aigner, D., Freunberger, S. A., Wilkening, M., Saf, R., Borisov, S. M. & Klimant, I. Enhancing Photoinduced Electron Transfer Efficiency of Fluorescent pH-Probes with Halogenated Phenols. *Analytical Chemistry* **86,** 9293–9300 (Sept. 16, 2014).

77. Huszthy, P., Lempert, K. & Simig, G. The reduction of triarylcarbenium ions by n-nucleophiles. The operation of the intramolecular version of the Olah–Svoboda mechanism in the reductive cyclization of the tris-(2,6-dimethoxyphenyl)carbenium ion. *J. Chem. Soc., Perkin Trans. 2,* 1351–1354 (1985).

78. Hammershoj, P., Sorensen, T. J., Han, B.-H. & Laursen, B. W. Base-Assisted One-Pot Synthesis of N, N', N"-Triaryltriazatriangulenium Dyes: Enhanced Fluorescence Efficiency by Steric Constraints. *The Journal of Organic Chemistry* **77,** 5606–5612 (July 6, 2012).

79. Wolfbeis, O. S. & Urbano, E. Fluorescence quenching method for determination of two or three components in solution. *Analytical Chemistry* **55,** 1904–1906 (Oct. 1983).

80. Huber, C., Krause, C., Werner, T. & Wolfbeis, O. S. Serum Chloride Optical Sensors Based on Dynamic Quenching of the Fluorescence of Photo-Immobilized Lucigenin. *Microchimica Acta* **142,** 245–253 (Jan. 1, 2003).

81. Mindell, J. A. Lysosomal Acidification Mechanisms. *Annual Review of Physiology* **74,** 69–86 (Mar. 17, 2012).

8 List of Figures

9 List of Tables

10 Appendix

10.1 NMR Data

10.1.1 2,2',6,6'-Tetramethoxybenzophenone

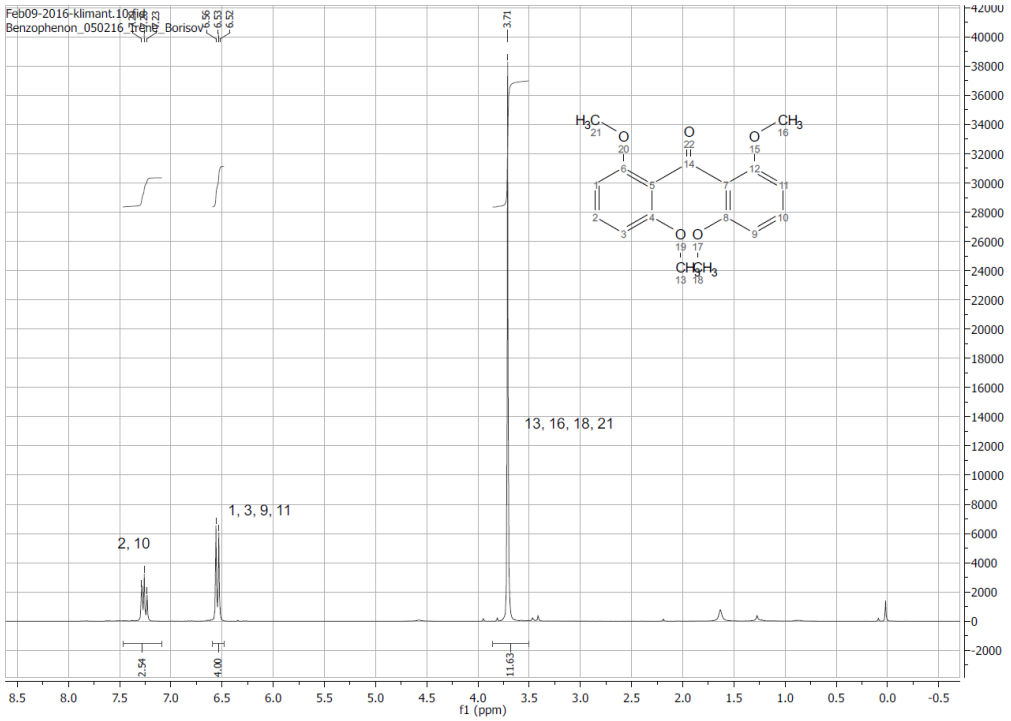

Figure 10.1: ^{1}H-NMR spectrum of 2,2',6,6'-tetramethoxybenzophenone in $CDCl_3$, measured at 300MHz

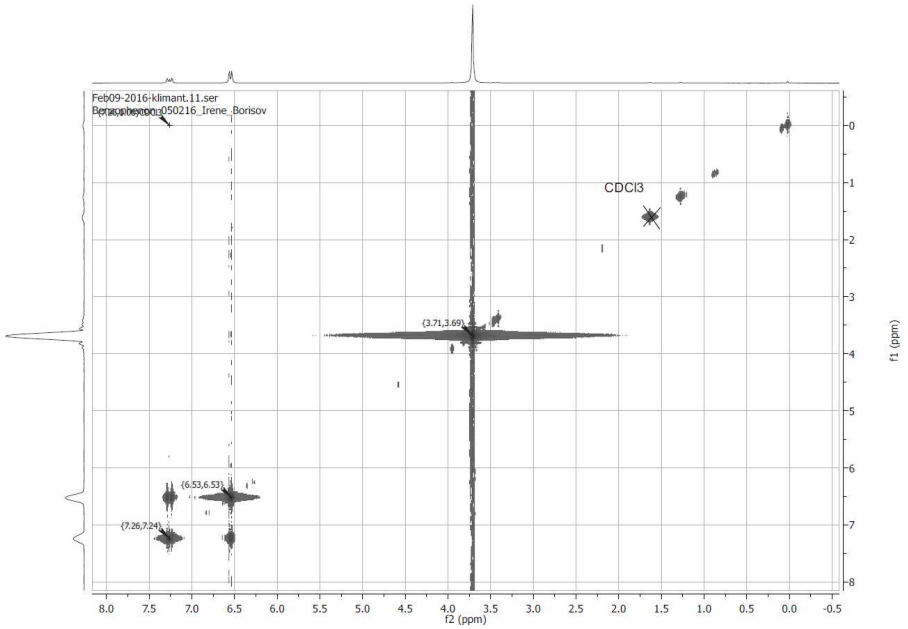

Figure 10.2: COSY-NMR spectrum of 2,2',6,6'-tetramethoxybenzophenone in $CDCl_3$, measured at 300MHz

10.1.2 Tris(2,6-dimethoxyphenyl)methanol

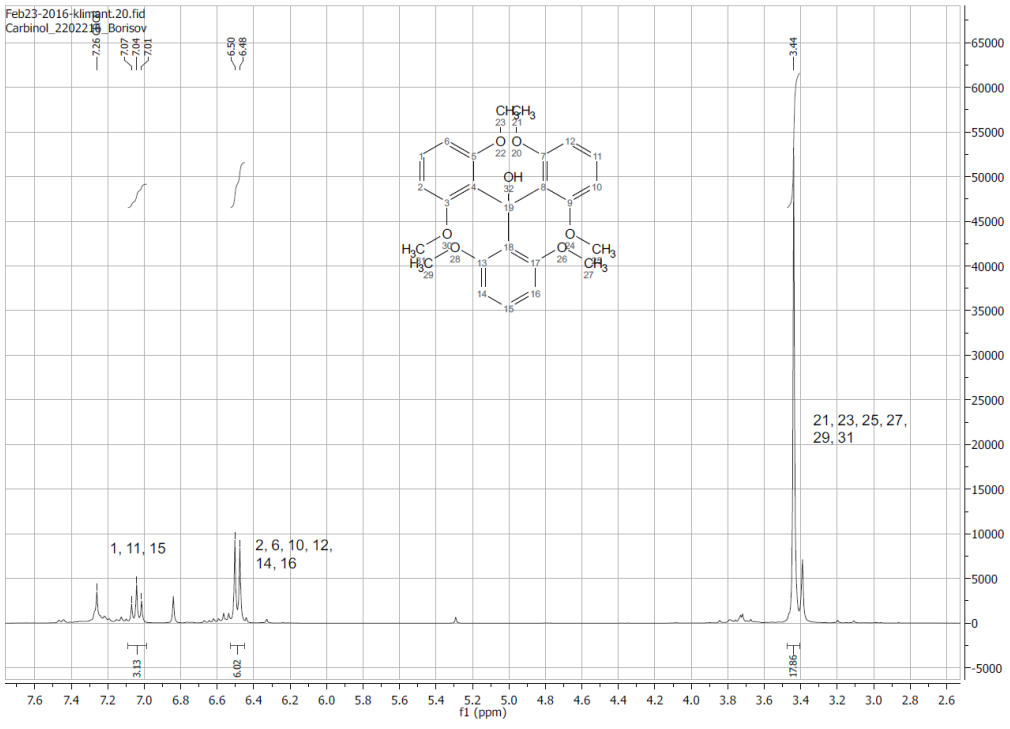

Figure 10.3: ^{1}H-NMR spectrum of tris(2,6-dimethoxyphenyl)methanol in $CDCl_3$, measured at 300MHz

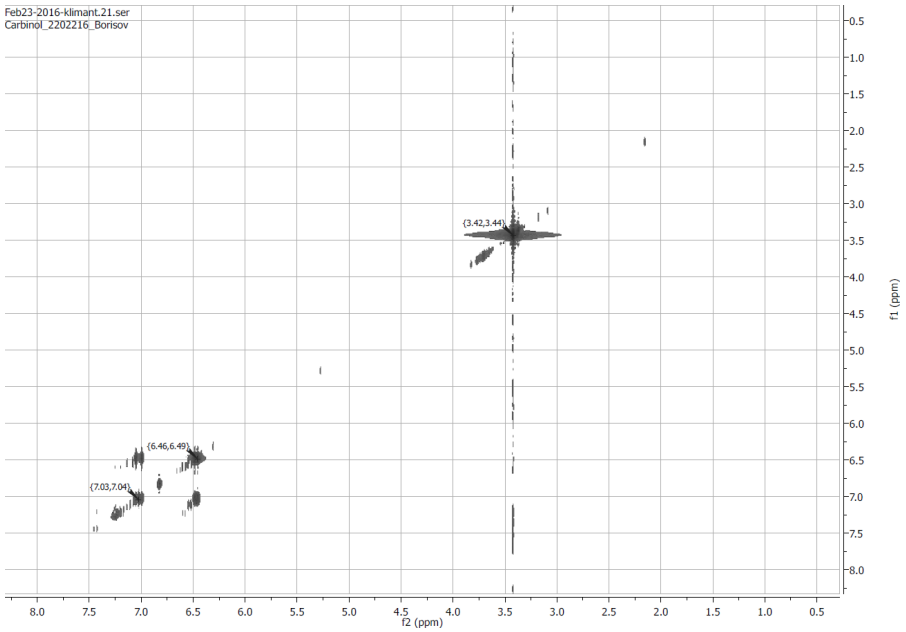

Figure 10.4: COSY-NMR spectrum of tris(2,6-dimethoxyphenyl)methanol in $CDCl_3$, measured at 300MHz

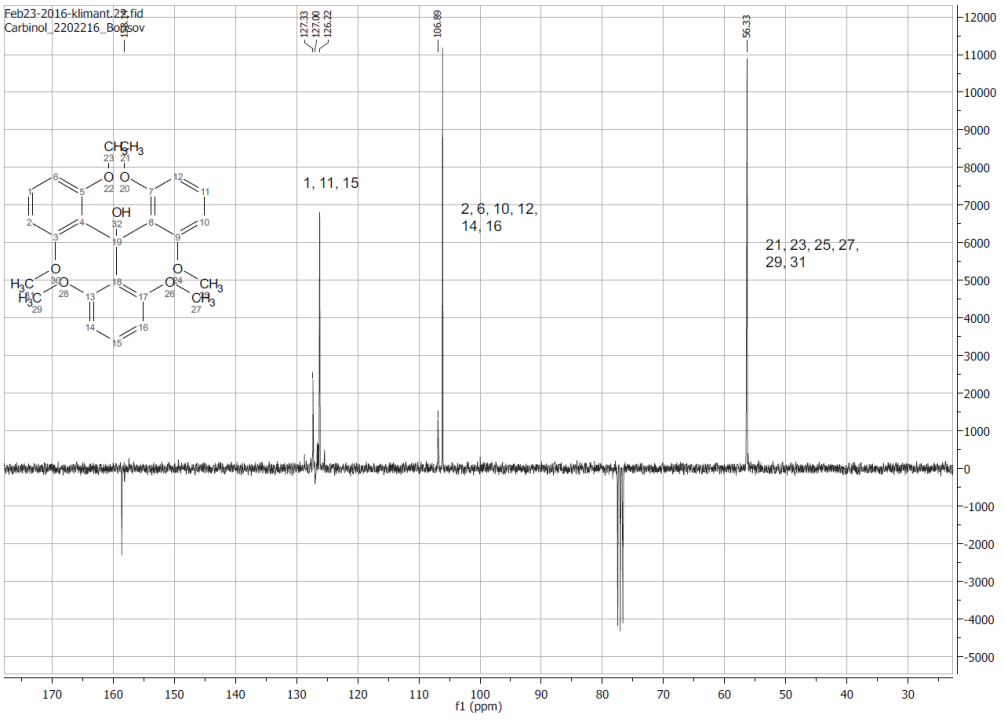

Figure 10.5: APT-NMR spectrum of tris(2,6-dimethoxyphenyl)methanol in $CDCl_3$, measured at 300MHz;
at 128 ppm: probably quarternary carbon atoms 4, 8, 18; at 160 ppm probably quarternary carbons 3, 5, 7, 9, 13, 17; quarternary carbons cannot be assigned with certainty

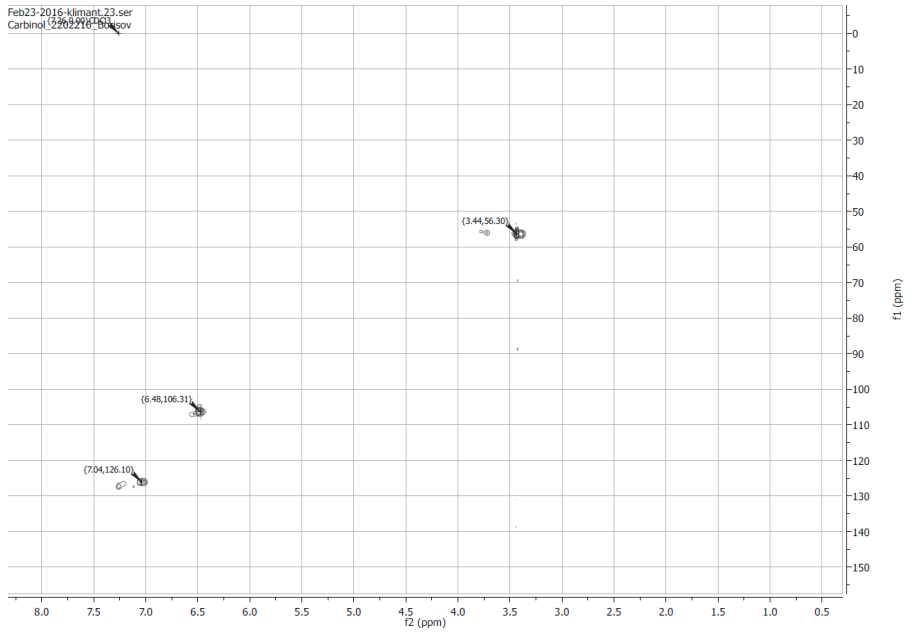

Figure 10.6: HSQC-NMR spectrum of tris(2,6-dimethoxyphenyl)methanol in $CDCl_3$, measured at 300MHz

10.1.3 TOTA$^+$

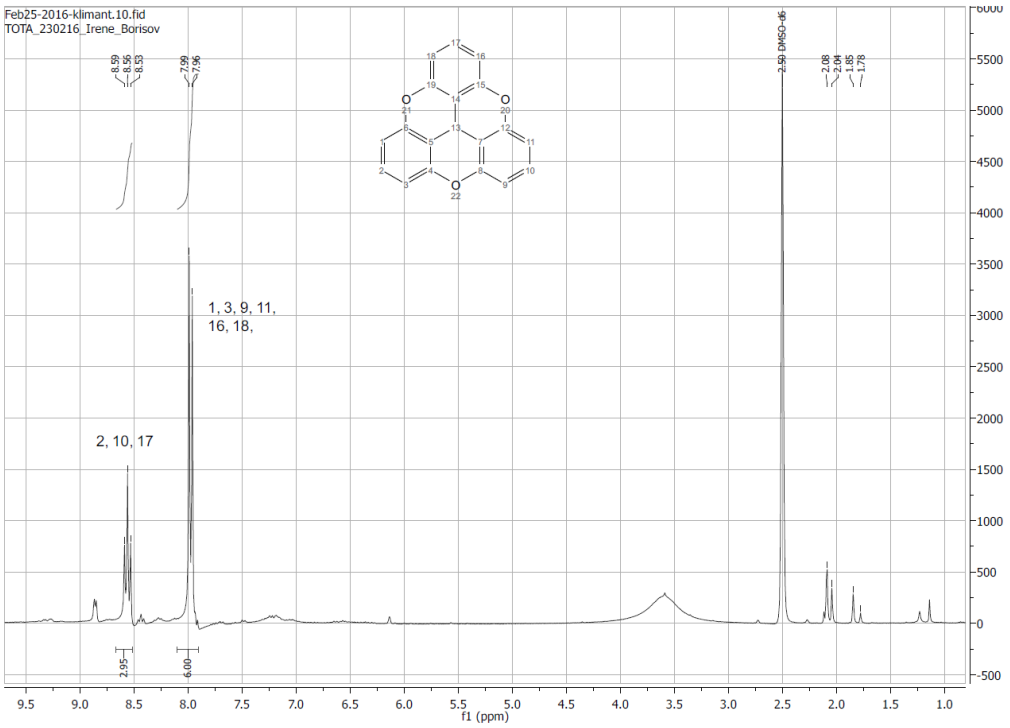

Figure 10.7: ^{1}H-NMR spectrum of TOTA$^+$ in DMSO-d_6, measured at 300MHz

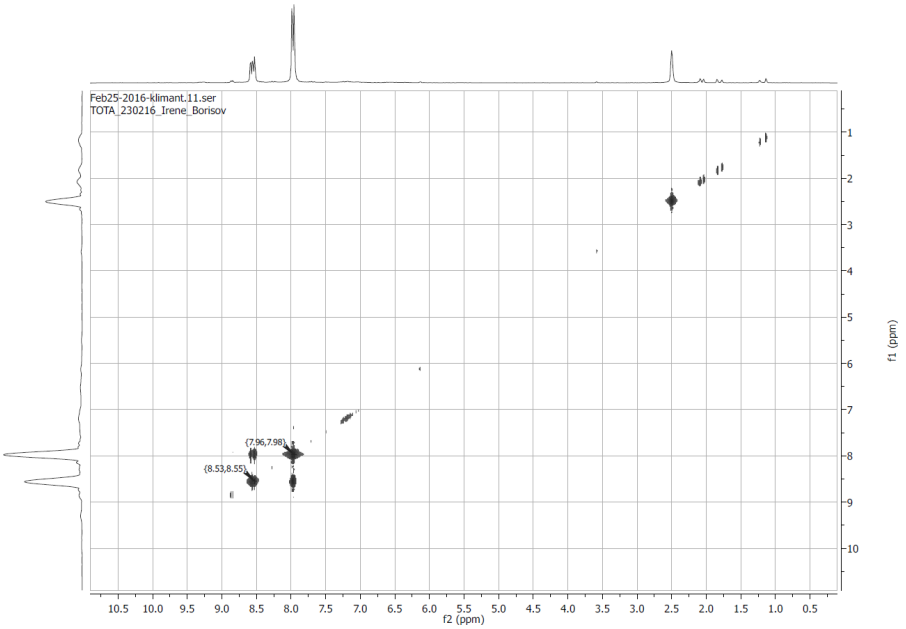

Figure 10.8: COSY-NMR spectrum of $TOTA^+$ in DMSO-d_6, measured at 300MHz

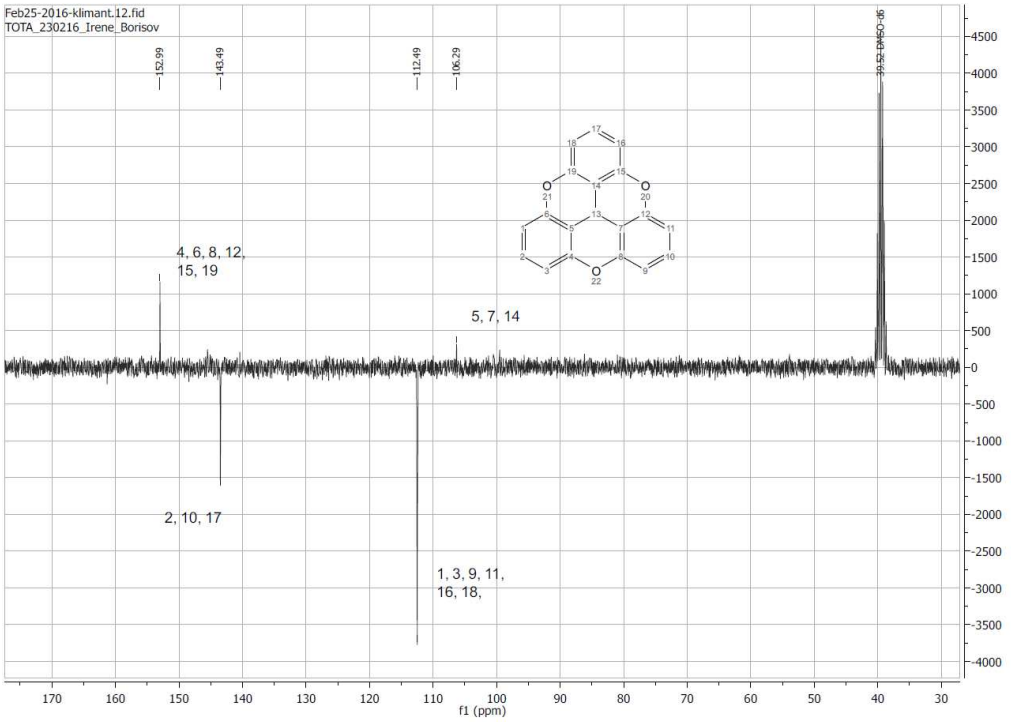

Figure 10.9: APT-NMR spectrum of $TOTA^+$ in DMSO-d_6, measured at 300MHz

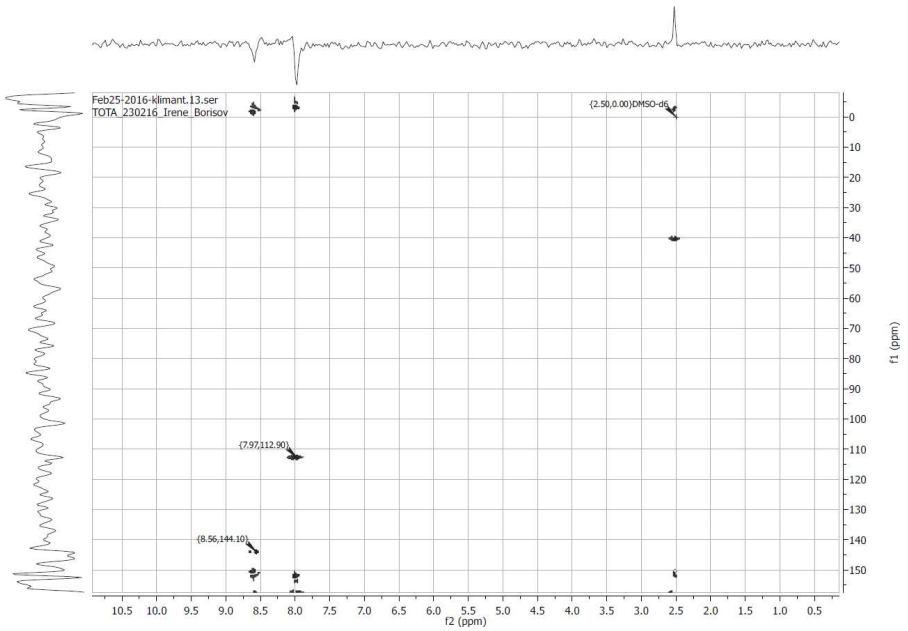

Figure 10.10: HSQC-NMR spectrum of $TOTA^+$ in DMSO-d_6, measured at 300MHz

10.1.4 *N*-Butyl ADOTA

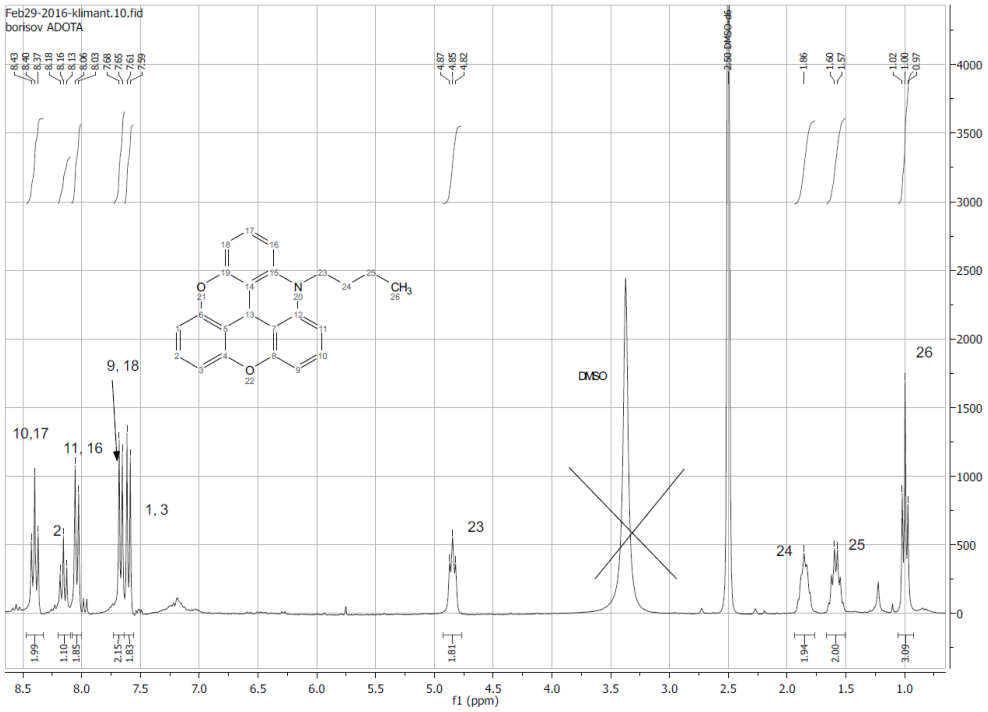

Figure 10.11: ^{1}H-NMR spectrum of *N*-Butyl ADOTA in DMSO-d_6, measured at 300MHz

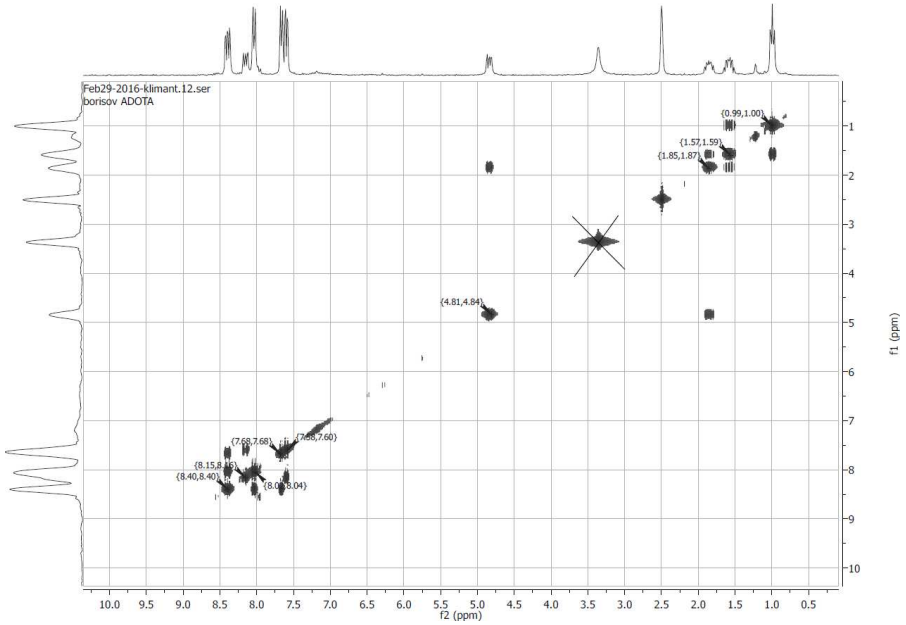

Figure 10.12: COSY-NMR spectrum of *N*-Butyl ADOTA in DMSO-d_6, measured at 300MHz

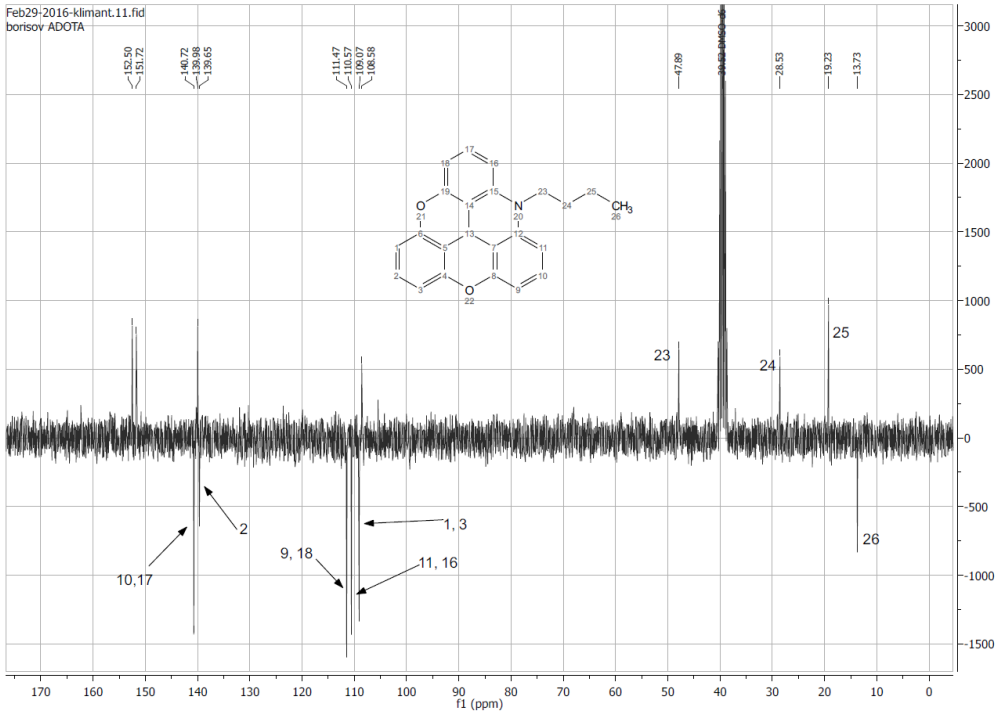

Figure 10.13: APT-NMR spectrum of *N*-Butyl ADOTA in DMSO-d_6, measured at 300MHz; at ∼110 ppm probably quarternary carbons 5, 7 and 14, at 150-152 ppm probably 4, 6, 8, 12, 15 and 19; quarternary carbons cannot be assigned with certainty

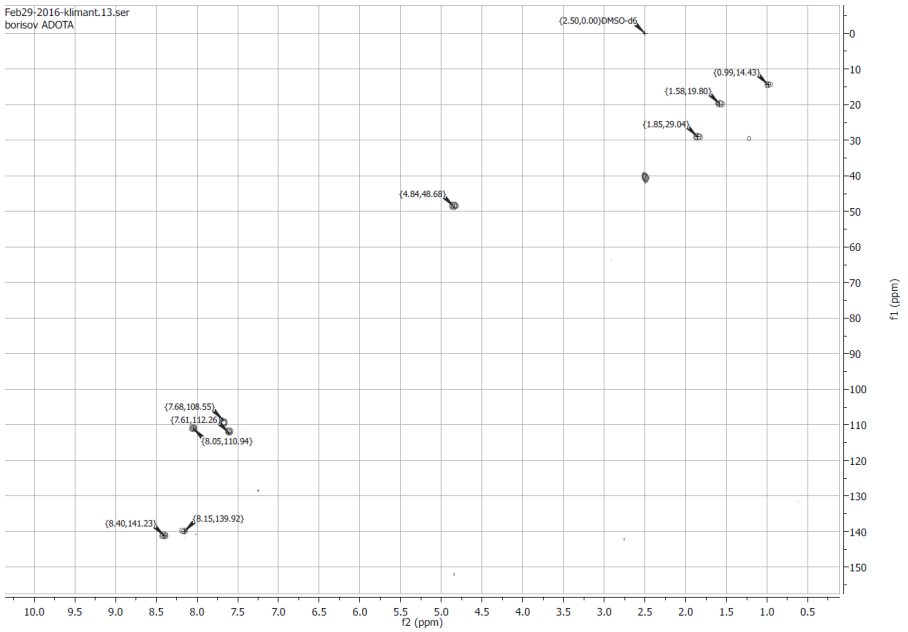

Figure 10.14: HSQC-NMR spectrum of *N*-Butyl ADOTA in DMSO-d_6, measured at 300MHz

10.1.5 Di-*N*-dodecyl DAOTA

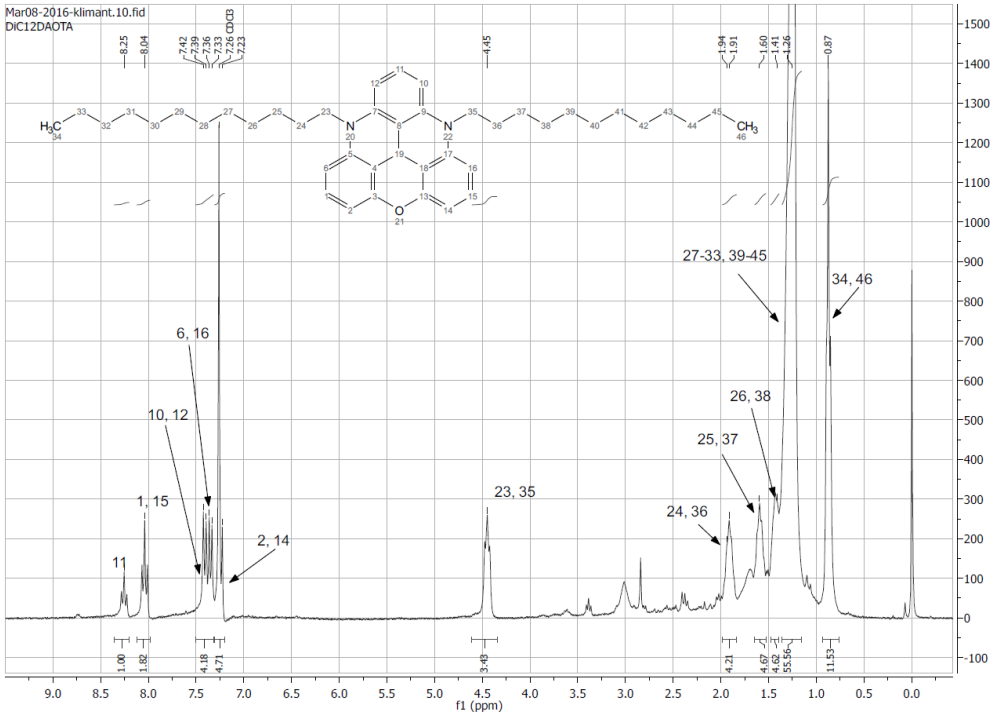

Figure 10.15: ^{1}H-NMR spectrum of Di-*N*-doodecyl DAOTA in $CDCl_3$, measured at 300MHz; at 0.87 and 1.26 ppm: impurities, probably H-grease or residual dodecylamine

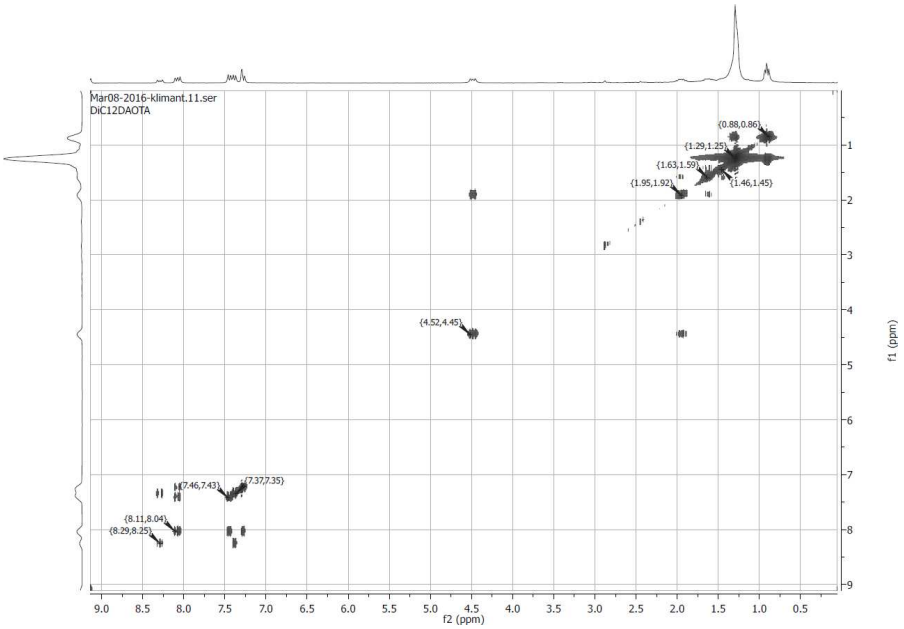

Figure 10.16: COSY-NMR spectrum of Di-*N*-doodecyl DAOTA in $CDCl_3$, measured at 300MHz

10.1.6 *N*-(6-Aminohexyl)-*N*-dodecyl DAOTA

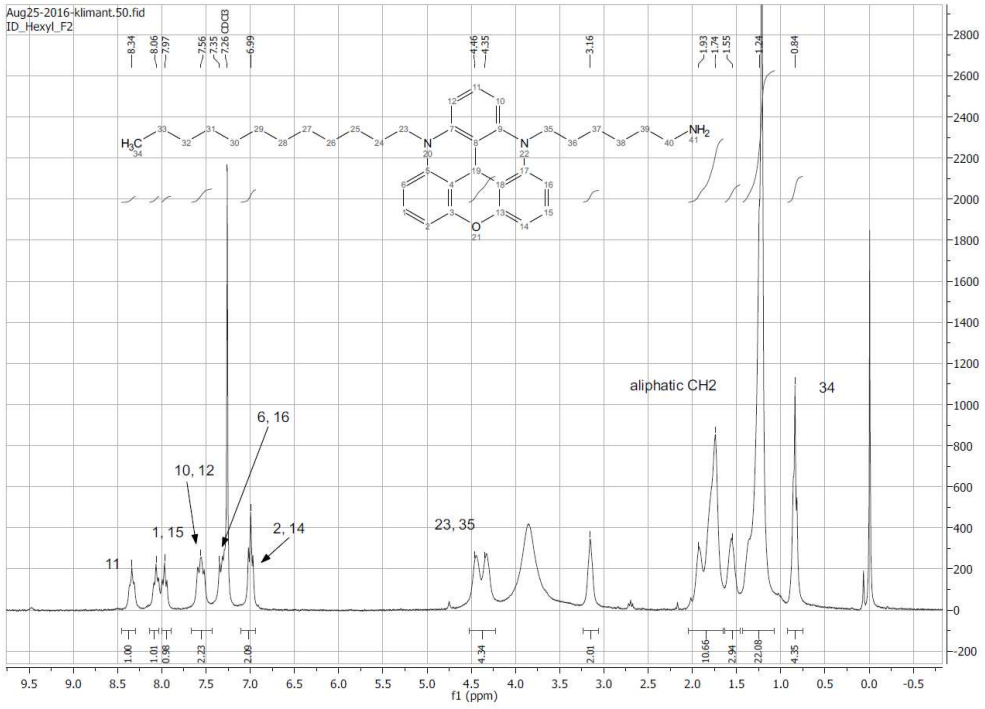

Figure 10.17: ^{1}H-NMR spectrum of *N*-(6-Aminohexyl)-*N*-dodecyl DAOTA in $CDCl_3$, measured at 300MHz

10.1.7 Product of Unsuccessful Synthesis of *N*-(*N*-Butylethyleneamine)-*N*-dodecyl DAOTA

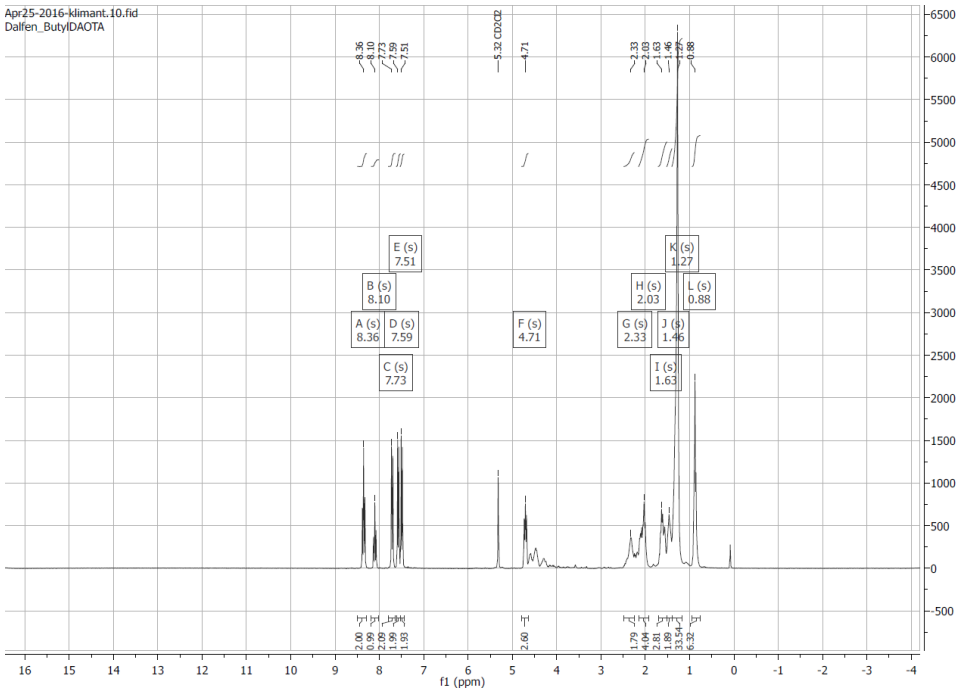

Figure 10.18: ^{1}H-NMR spectrum of product of unsuccessful synthesis of *N*-(*N*-Butylethyleneamine)-*N*-dodecyl DAOTA

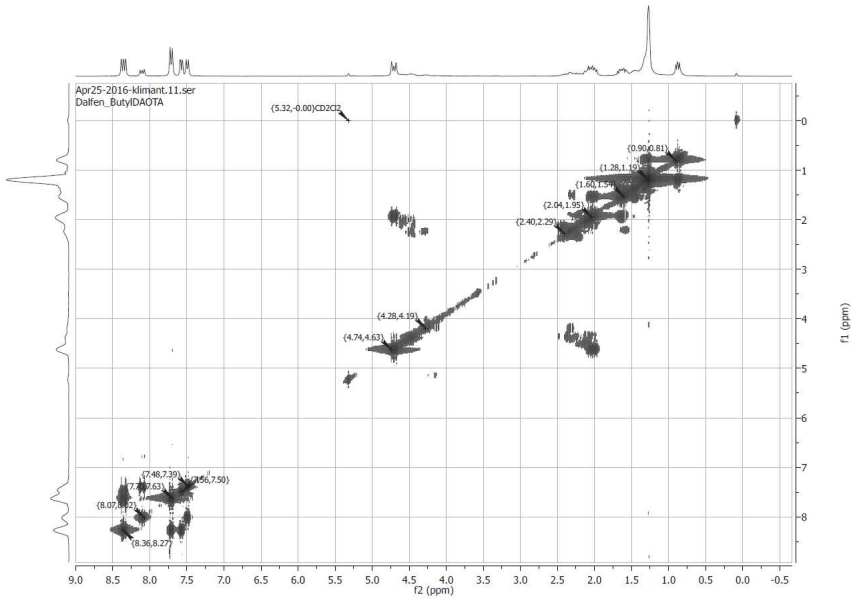

Figure 10.19: COSY-NMR spectrum of product of unsuccessful synthesis of *N*-(*N*-Butylethyleneamine)-*N*-dodecyl DAOTA

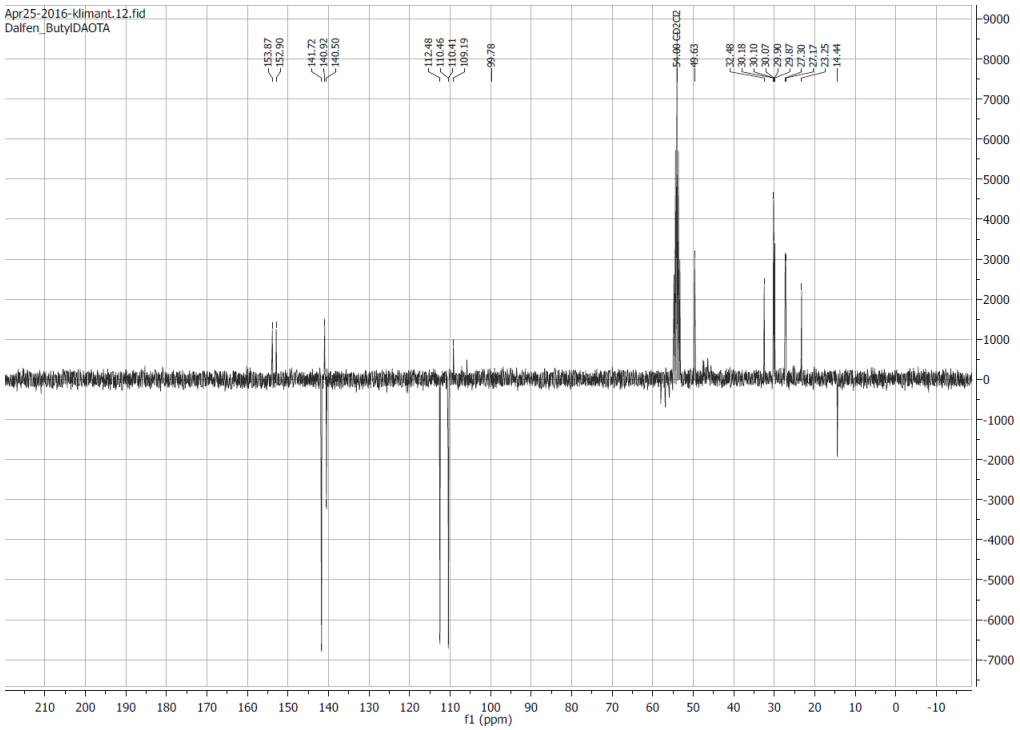

Figure 10.20: APT-NMR spectrum of product of unsuccessful synthesis of *N*-(*N*-Butylethyleneamine)-*N*-dodecyl DAOTA

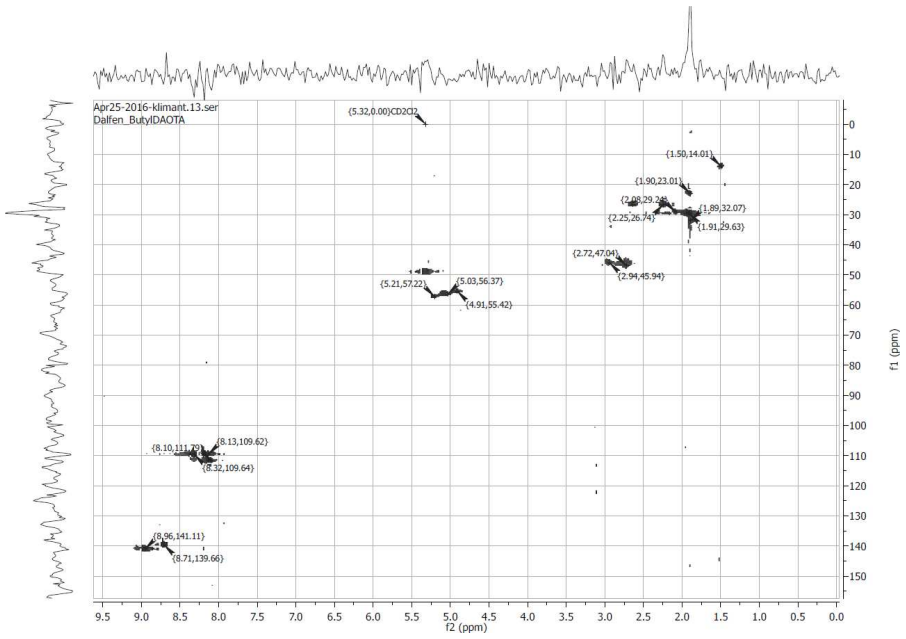

Figure 10.21: HSQC-NMR spectrum of product of unsuccessful synthesis of *N*-(*N*-Butylethyleneamine)-*N*-dodecyl DAOTA

10.1.8 Product of Unsuccessful Synthesis of *N*-(3-Morpholinopropyl)-*N*-dodecyl DAOTA

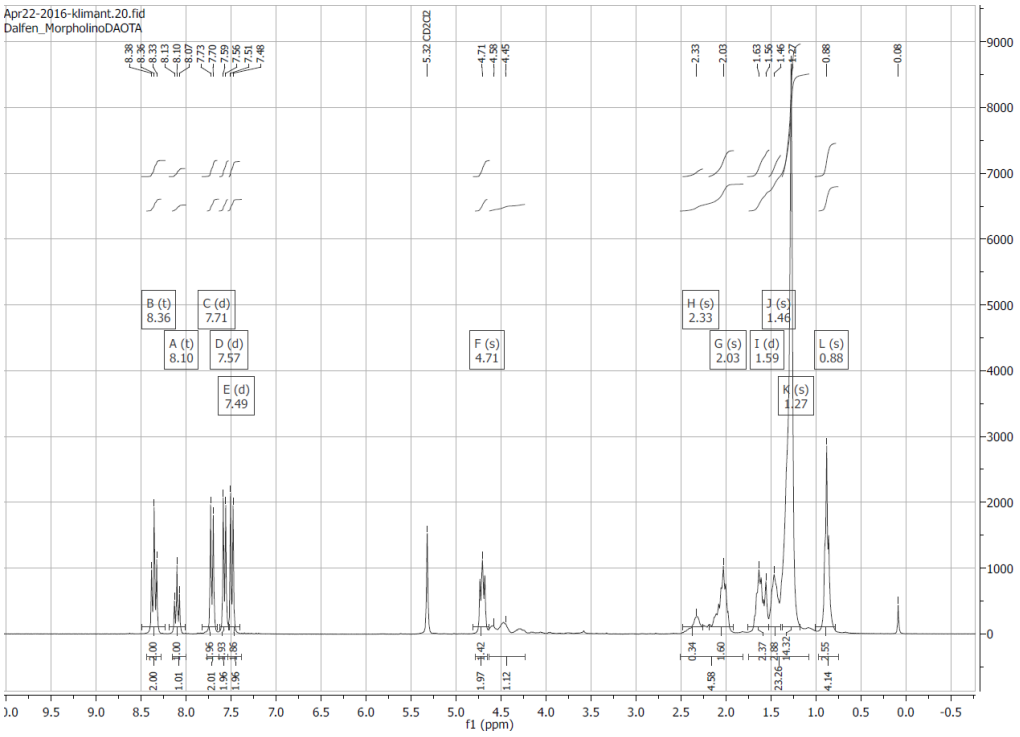

Figure 10.22: ^{1}H-NMR spectrum of product of unsuccessful synthesis of *N*-(3-Morpholinopropyl)-*N*-dodecyl DAOTA

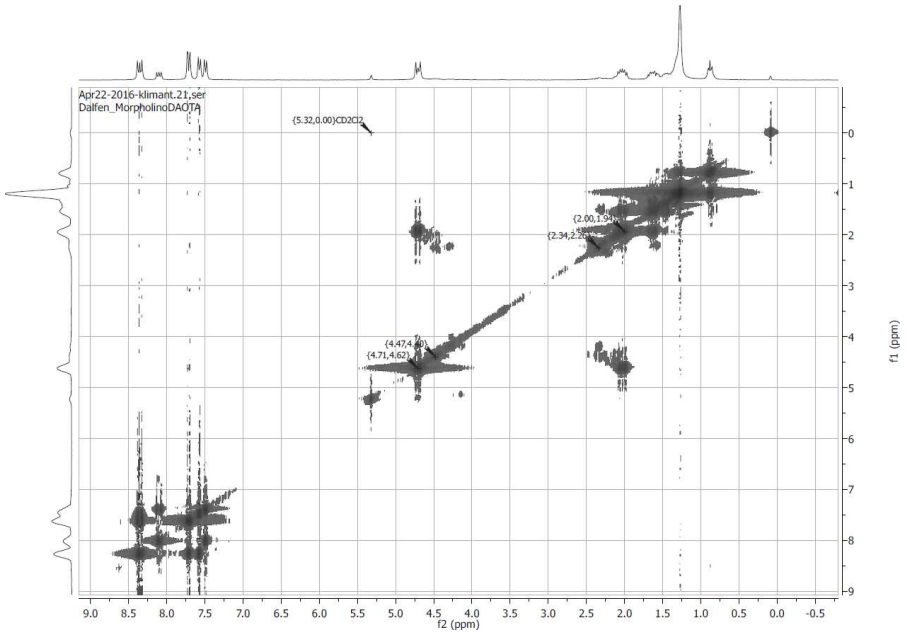

Figure 10.23: COSY-NMR spectrum of product of unsuccessful synthesis of *N*-(3-Morpholinopropyl)-*N*-dodecyl DAOTA

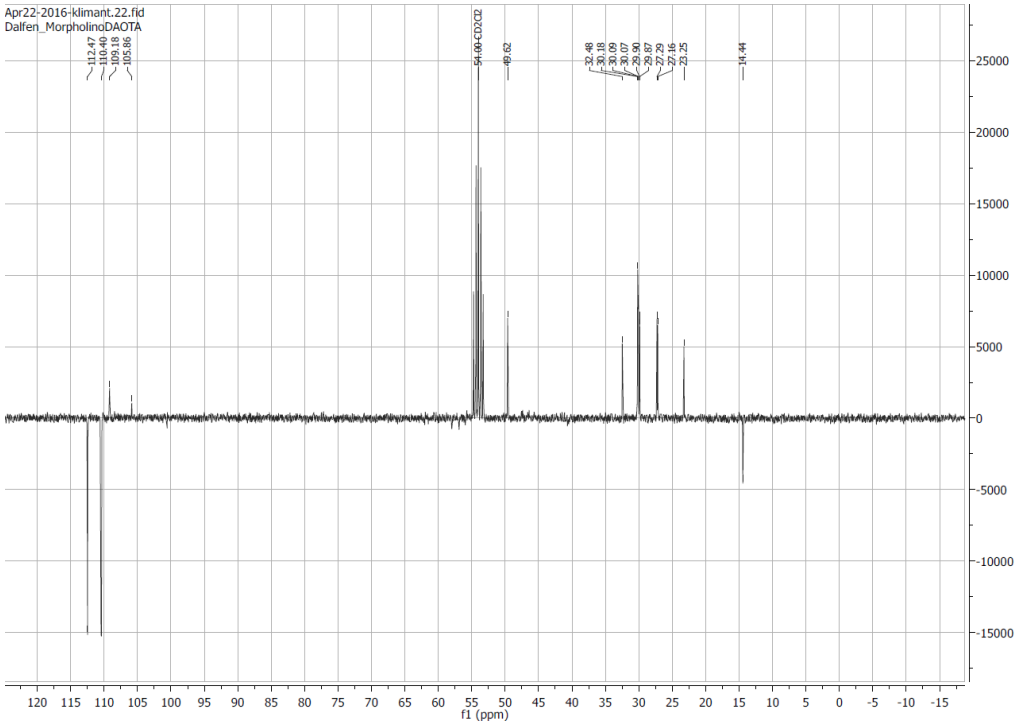

Figure 10.24: APT-NMR spectrum of product of unsuccessful synthesis of *N*-(3-Morpholinopropyl)-*N*-dodecyl DAOTA

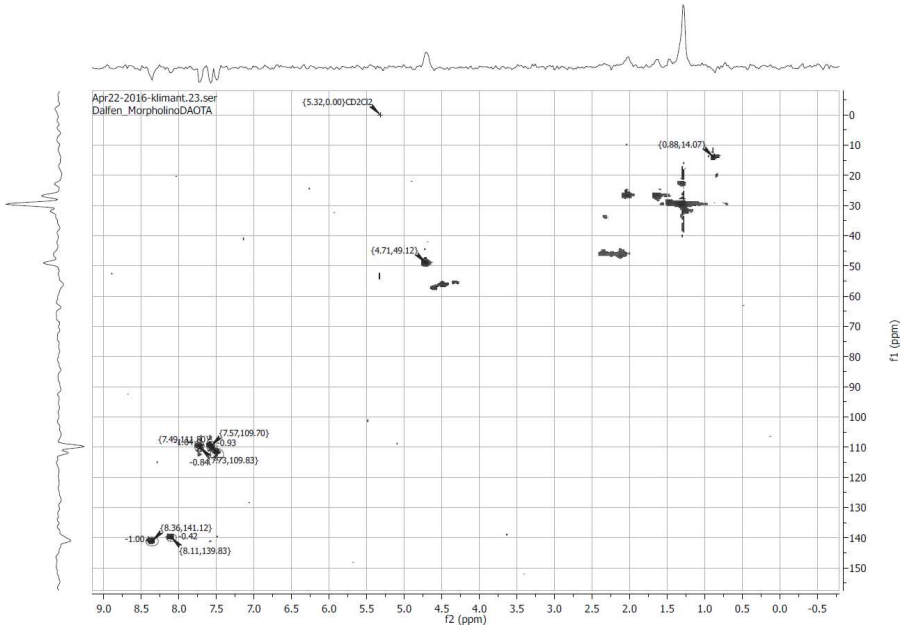

Figure 10.25: HSQC-NMR spectrum of product of unsuccessful synthesis of *N*-(3-Morpholinopropyl)-*N*-dodecyl DAOTA

10.1.9 *N*-(3-Morpholinopropyl)-*N*-dodecyl DAOTA

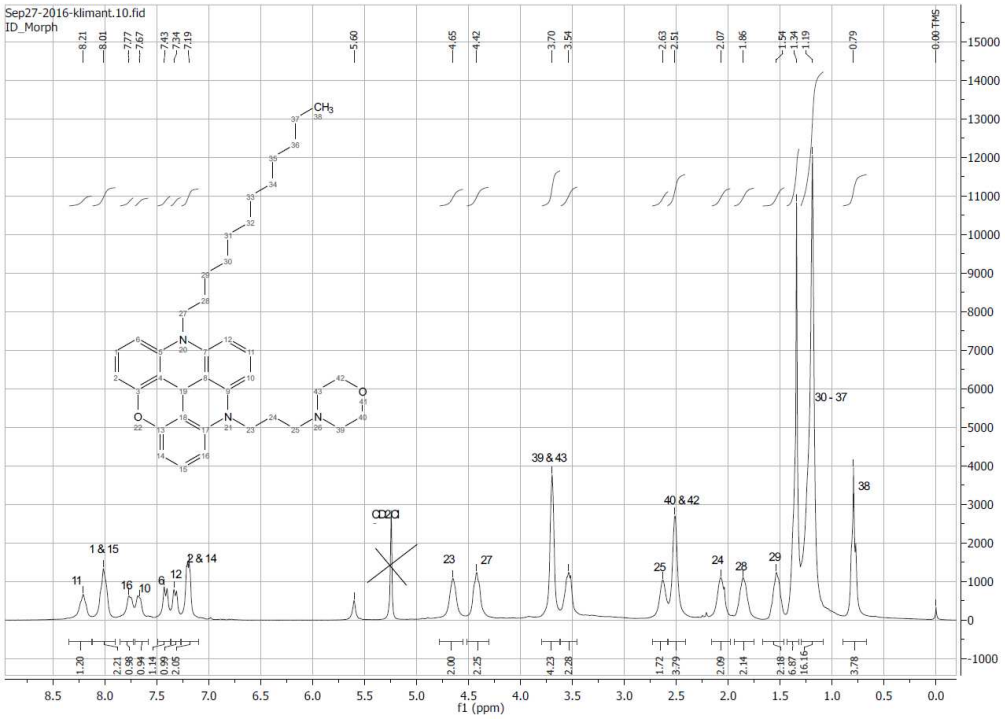

Figure 10.26: ^{1}H-NMR spectrum of *N*-(3-Morpholinopropyl)-*N*-dodecyl DAOTA in CD_2Cl_2, measured at 300 MHz

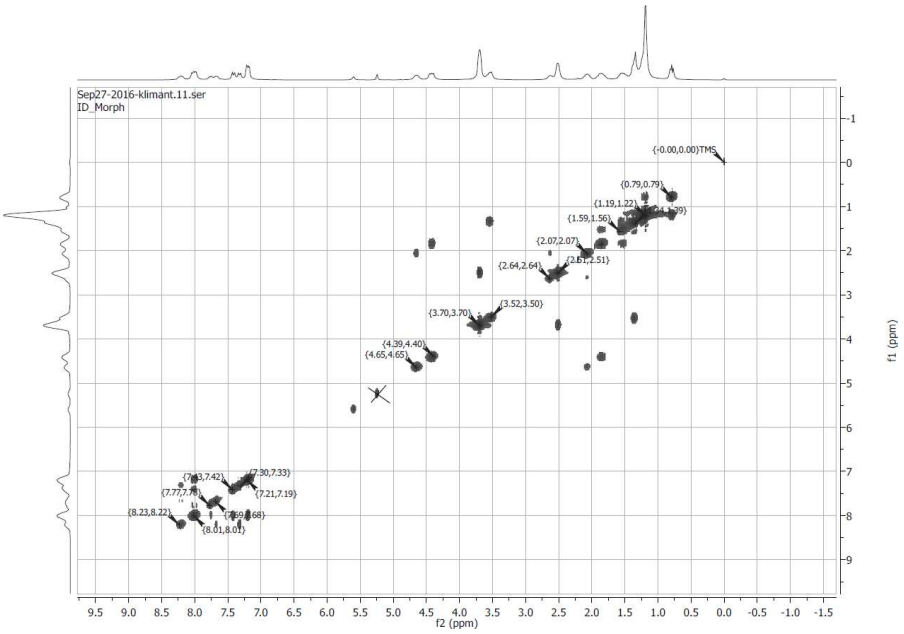

Figure 10.27: COSY-NMR spectrum of *N*-(3-Morpholinopropyl)-*N*-dodecyl DAOTA in CD_2Cl_2, measured at 300 MHz

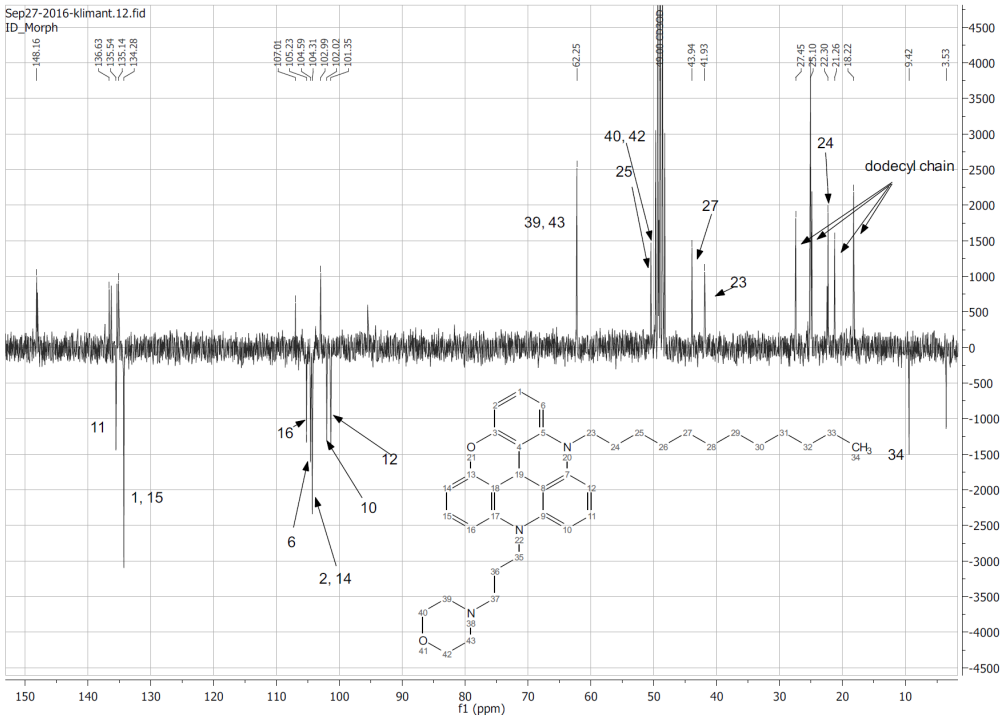

Figure 10.28: APT-NMR spectrum of *N*-(3-Morpholinopropyl)-*N*-dodecyl DAOTA in CD_2Cl_2, measured at 300 MHz

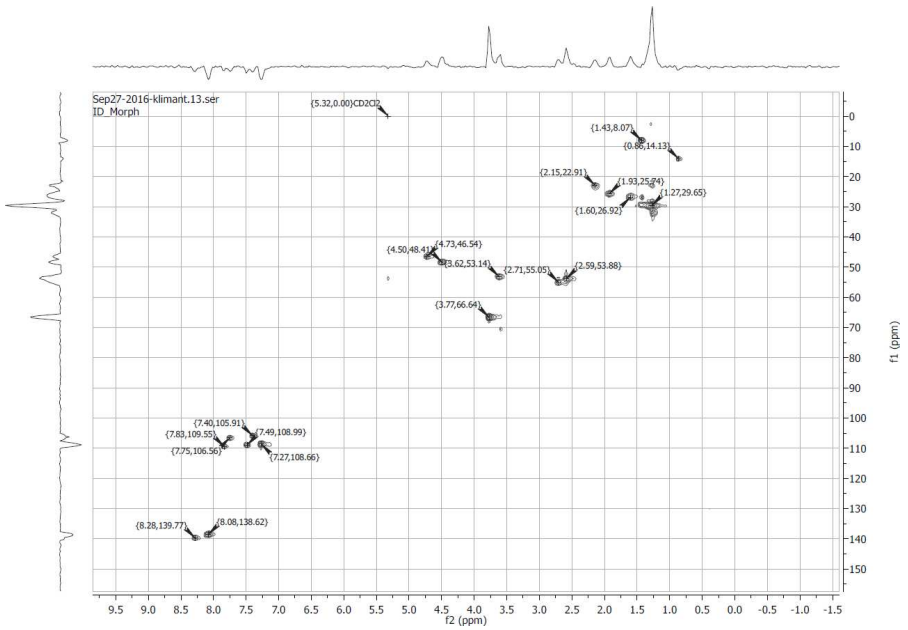

Figure 10.29: HSQC-NMR spectrum of *N*-(3-Morpholinopropyl)-*N*-dodecyl DAOTA in CD_2Cl_2, measured at 300 MHz

10.1.10 3-Chloro-4-hydoxybenzylamine

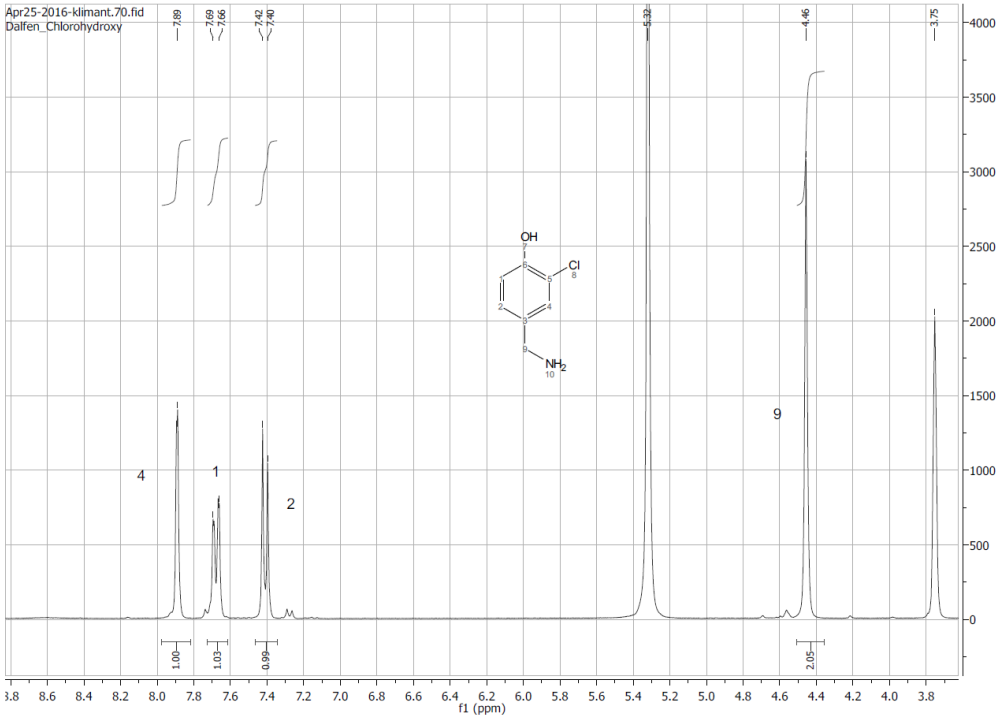

Figure 10.30: ^{1}H-NMR spectrum of 3-Chloro-4-hydoxybenzylamine in CD_2Cl_2, measured at 300 MHz

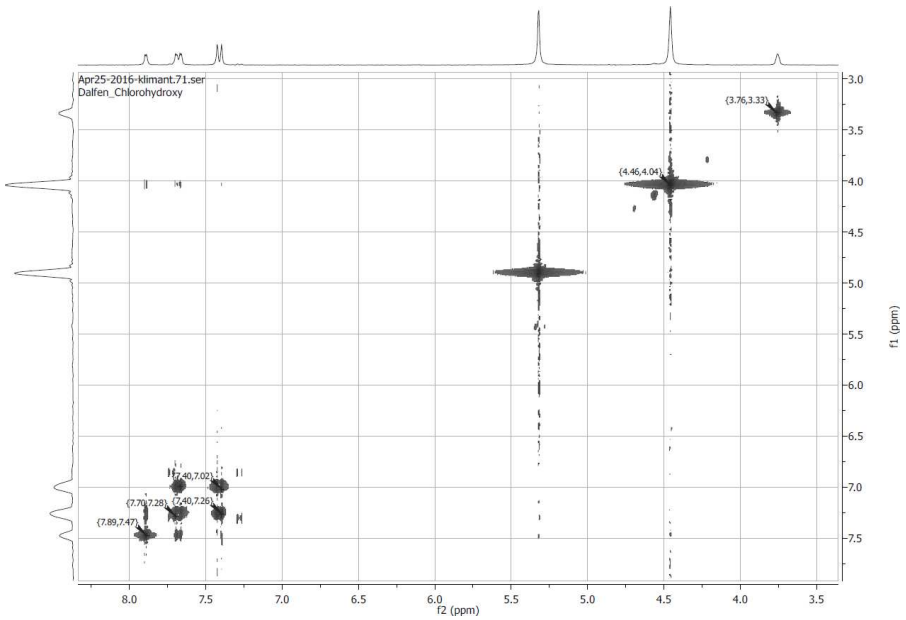

Figure 10.31: COSY-NMR spectrum of 3-Chloro-4-hydoxybenzylamine in CD_2Cl_2, measured at 300 MHz

10.1.11 *N*-(3,5-Dichloro-4-hydroxyphenyl)-*N*-dodecyl DAOTA

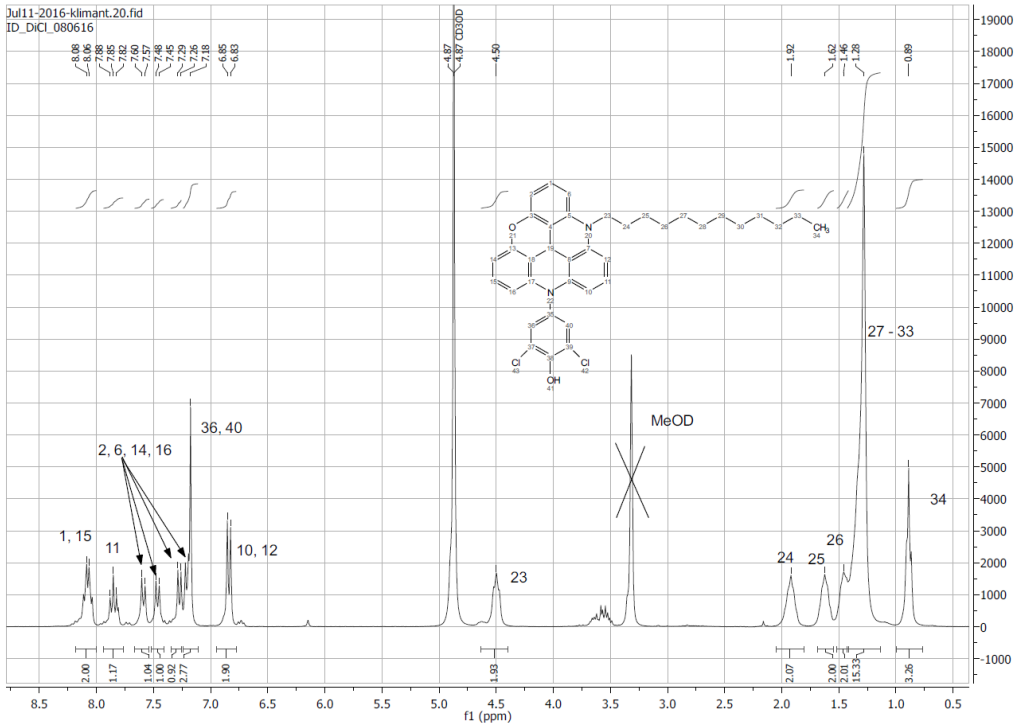

Figure 10.32: ^{1}H-NMR spectrum of *N*-(3,5-Dichloro-4-hydroxyphenyl)-*N*-dodecyl DAOTA in CD_3OD, measured at 300 MHz

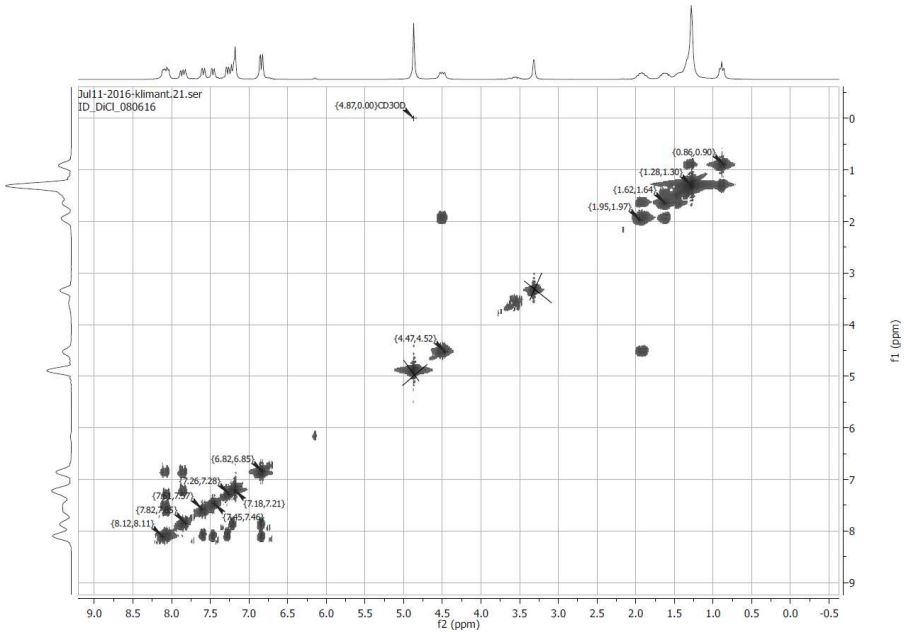

Figure 10.33: COSY-NMR spectrum of *N*-(3,5-Dichloro-4-hydroxyphenyl)-*N*-dodecyl DAOTA in CD_3OD, measured at 300 MHz

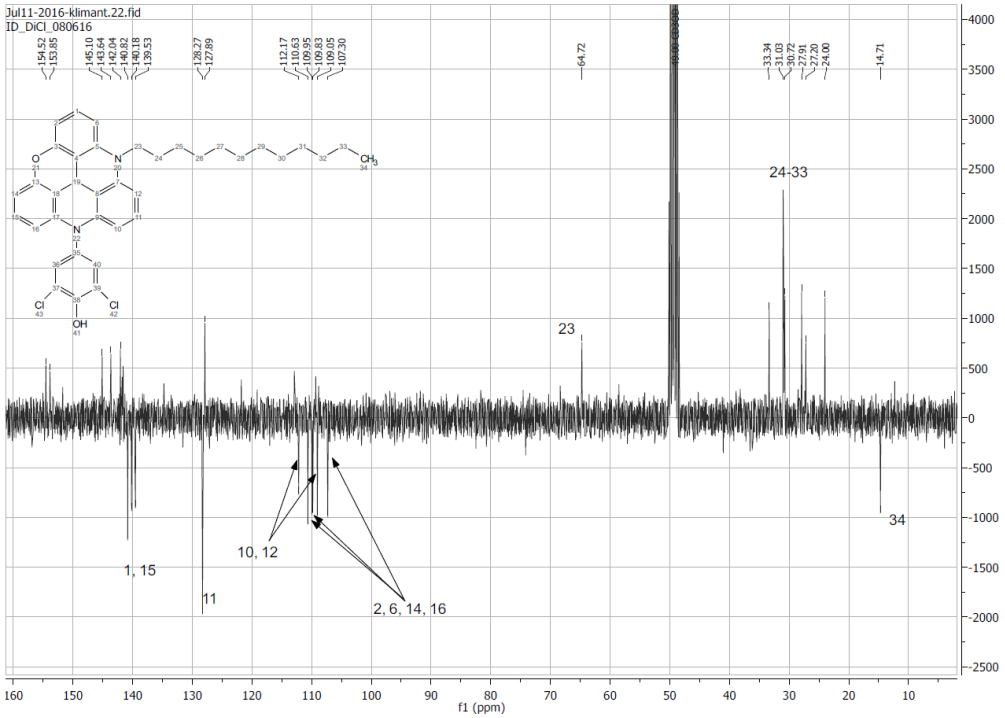

Figure 10.34: APT-NMR spectrum of *N*-(3,5-Dichloro-4-hydroxyphenyl)-*N*-dodecyl DAOTA in CD_3OD, measured at 300 MHz

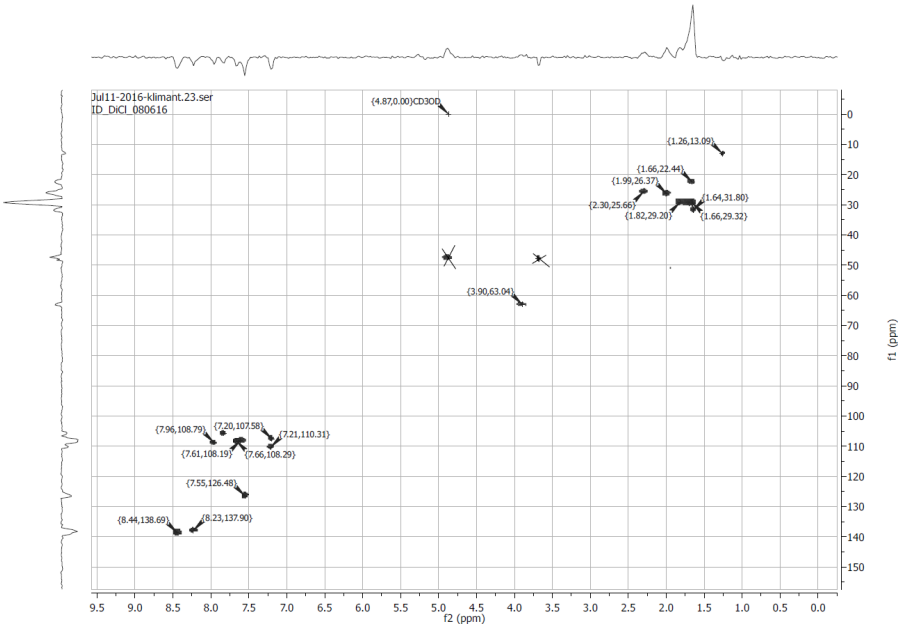

Figure 10.35: HSQC-NMR spectrum of *N*-(3,5-Dichloro-4-hydroxyphenyl)-*N*-dodecyl DAOTA in CD_3OD, measured at 300 MHz

10.1.12 *N*-(3-Chloro-4-hydroxyphenyl)-*N*-dodecyl DAOTA

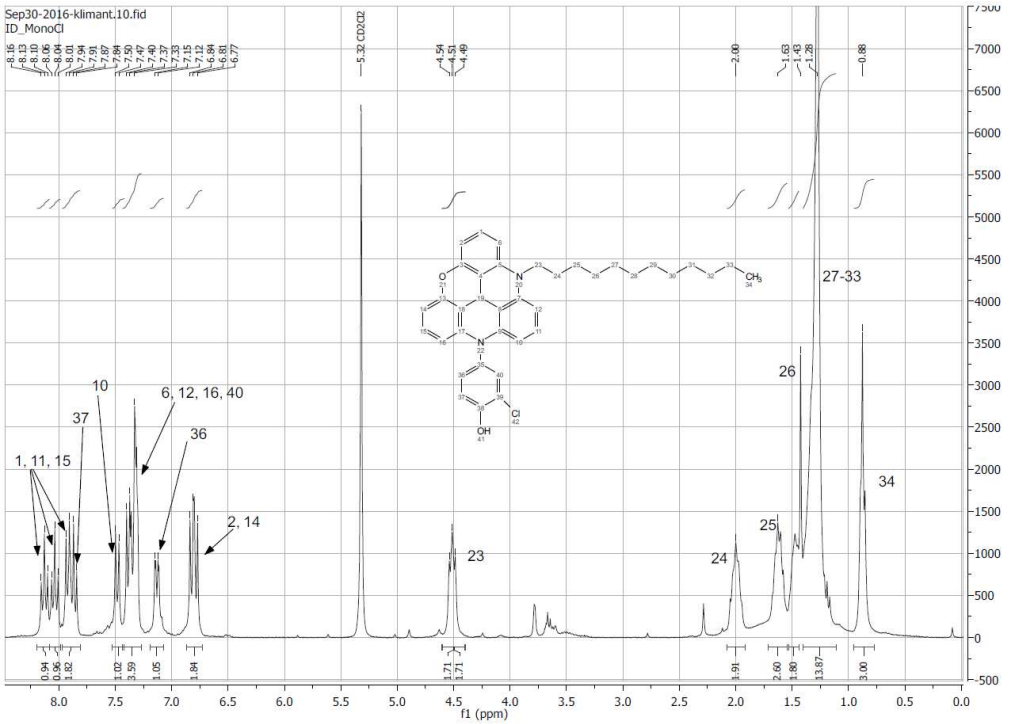

Figure 10.36: ^{1}H-NMR spectrum of *N*-(3-Chloro-4-hydroxyphenyl)-*N*-dodecyl DAOTA in CD_2Cl_2, measured at 300 MHz

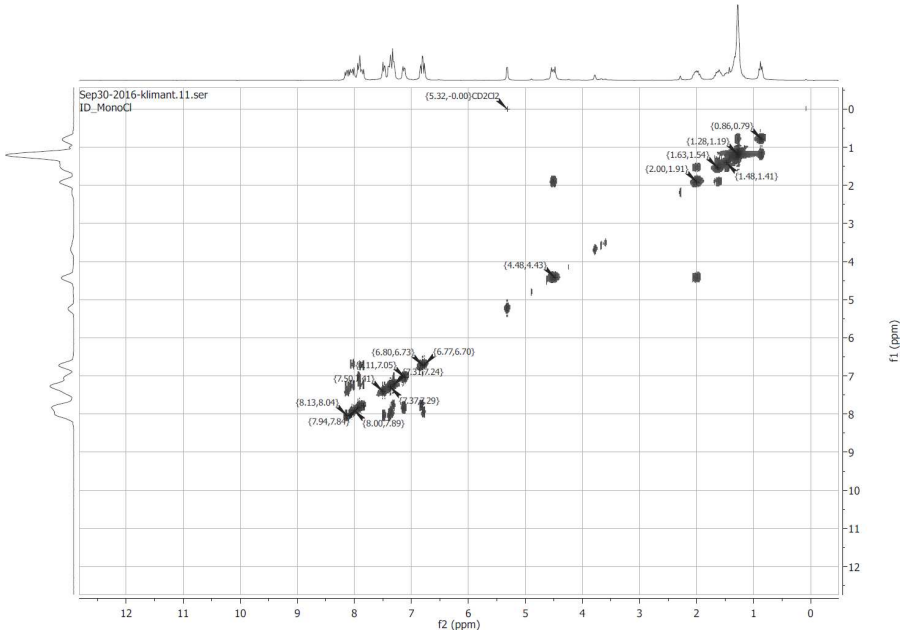

Figure 10.37: COSY-NMR spectrum of *N*-(3-Chloro-4-hydroxyphenyl)-*N*-dodecyl DAOTA in CD_2Cl_2, measured at 300 MHz

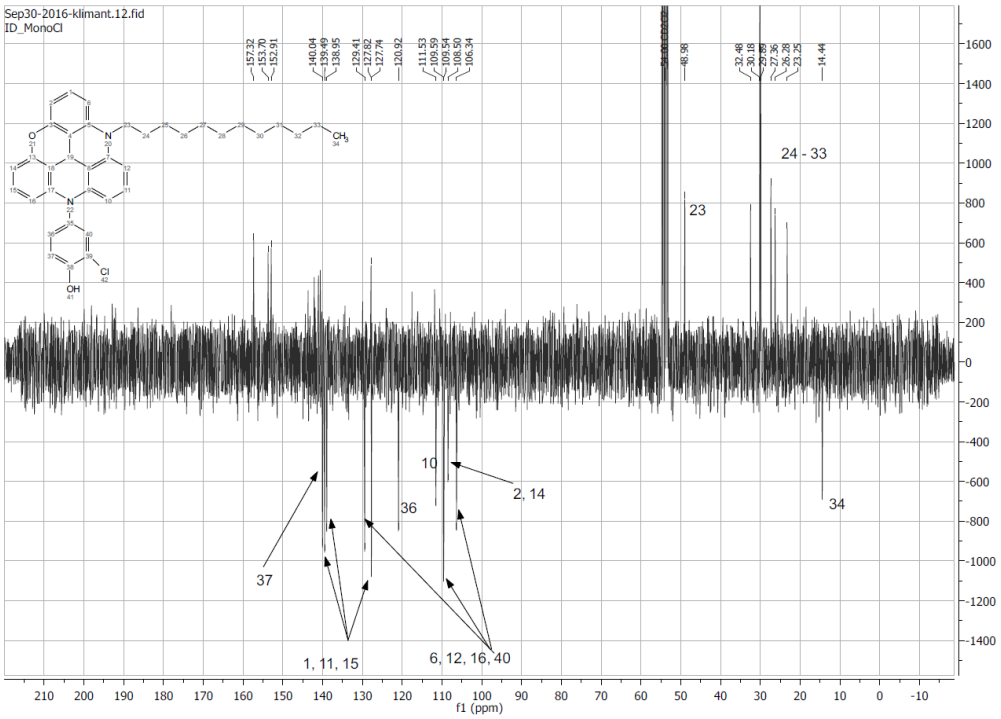

Figure 10.38: APT-NMR spectrum of *N*-(3-Chloro-4-hydroxyphenyl)-*N*-dodecyl DAOTA in CD_2Cl_2, measured at 300 MHz

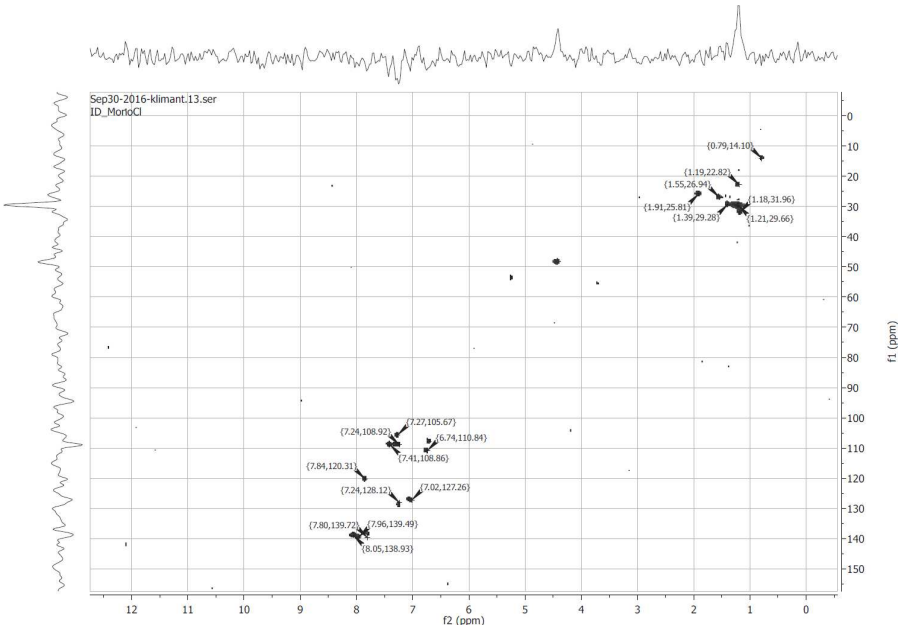

Figure 10.39: HSQC-NMR spectrum of *N*-(3-Chloro-4-hydroxyphenyl)-*N*-dodecyl DAOTA in CD_2Cl_2, measured at 300 MHz

10.2 MS Data

10.2.1 Dye (2) (Didodecyl DAOTA$^+$)

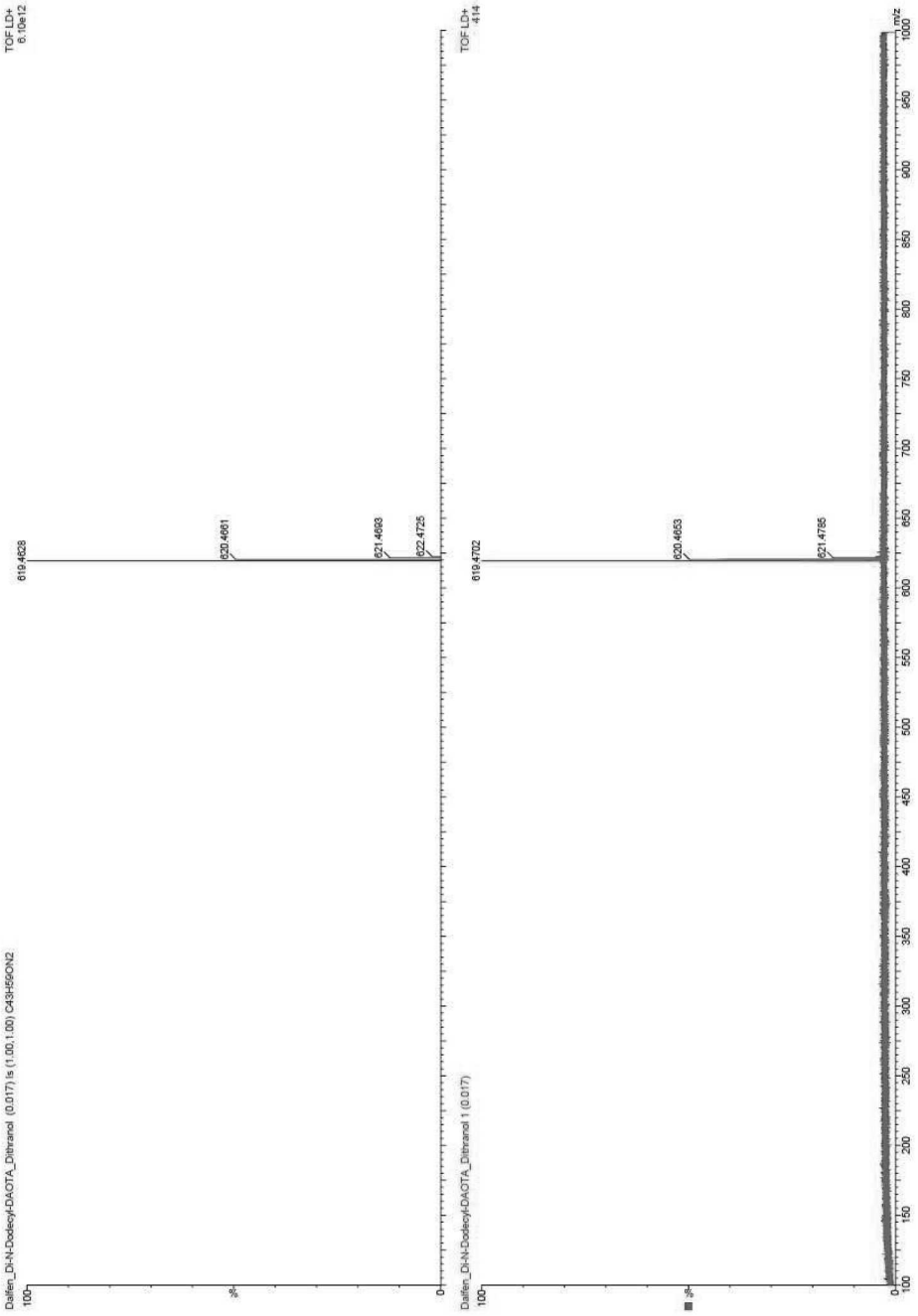

Figure 10.40: MALDI-TOF spectrum of compound **(2)**in a dithranol matrix; upper graph: calculated isotope pattern [M$^+$]=619.46; lower graph: detected isotope pattern [M$^+$]=619.47

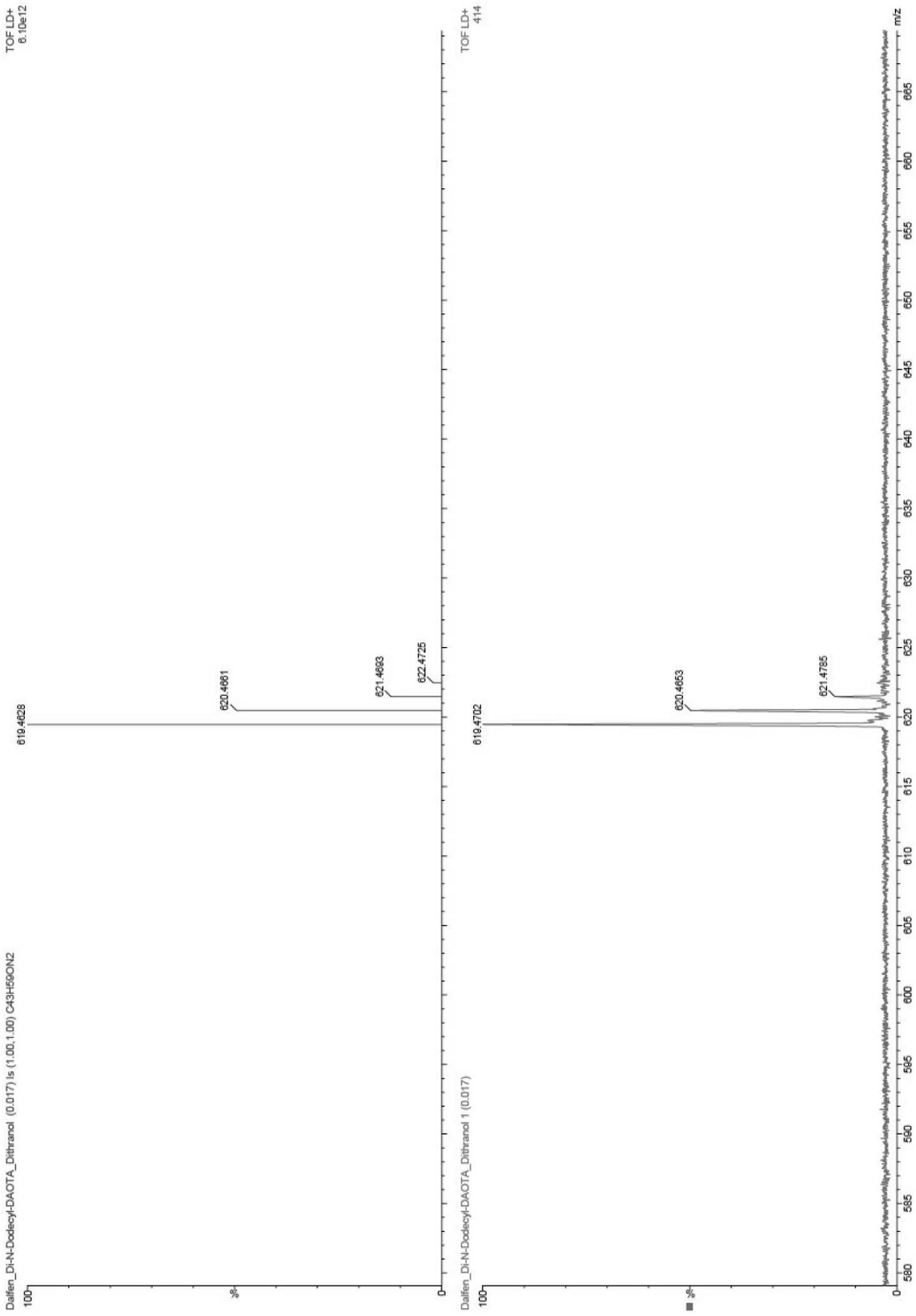

Figure 10.41: Closer view on MALDI-TOF spectrum of compound **(2)**in a dithranol matrix; upper graph: calculated isotope pattern $[M^+]$=619.46; lower graph: detected isotope pattern $[M^+]$=619.47

10.2.2 Dye (3) (Aminohexyl DAOTA$^+$)

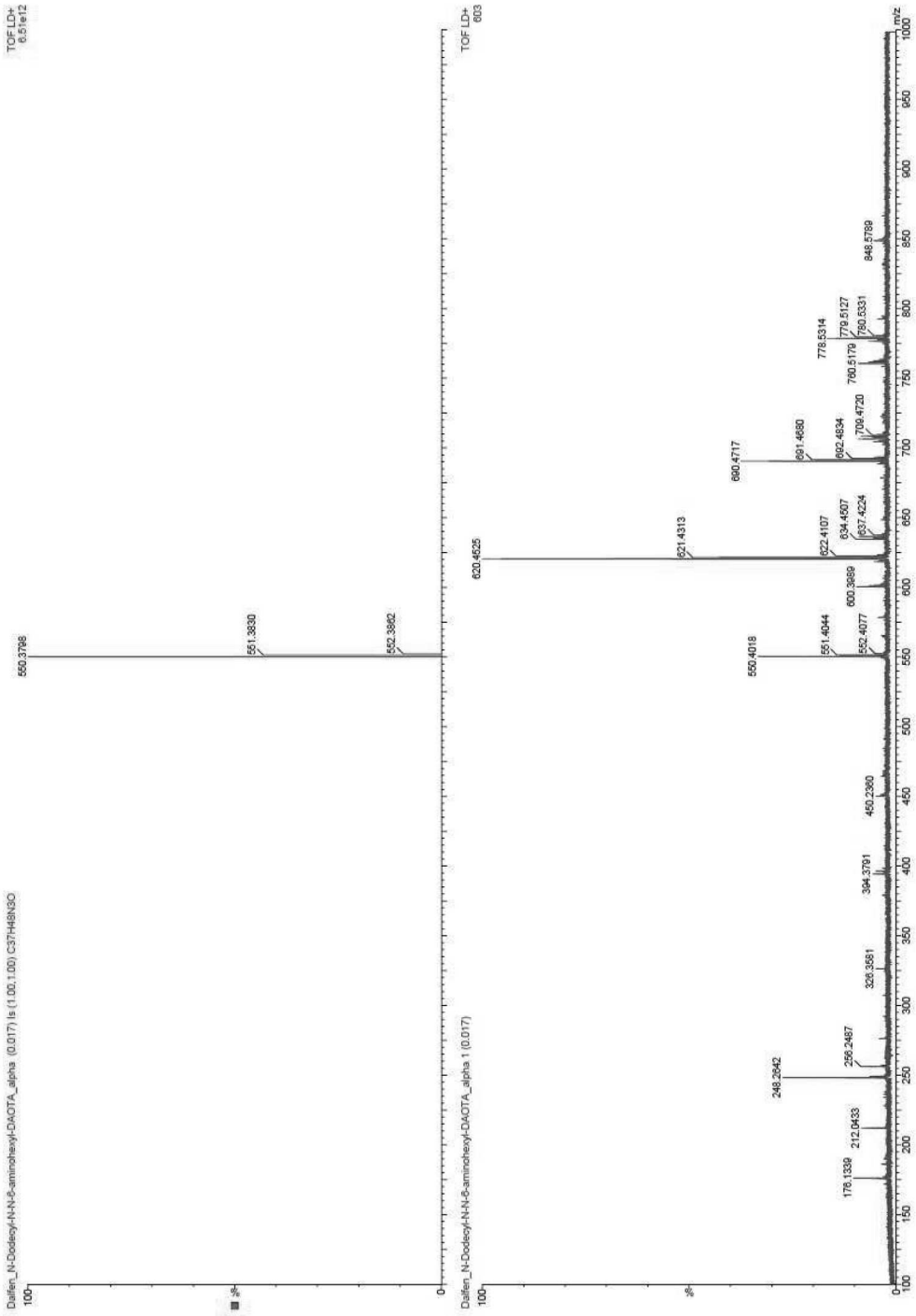

Figure 10.42: MALDI-TOF spectrum of compound **(3)**in an alpha matrix; upper graph: calculated isotope pattern [M$^+$]=550.38; lower graph: detected isotope pattern [M$^+$]=550.40, 620.45, 690.47

10.2.3 Dye (4) (Dichloro DAOTA$^+$)

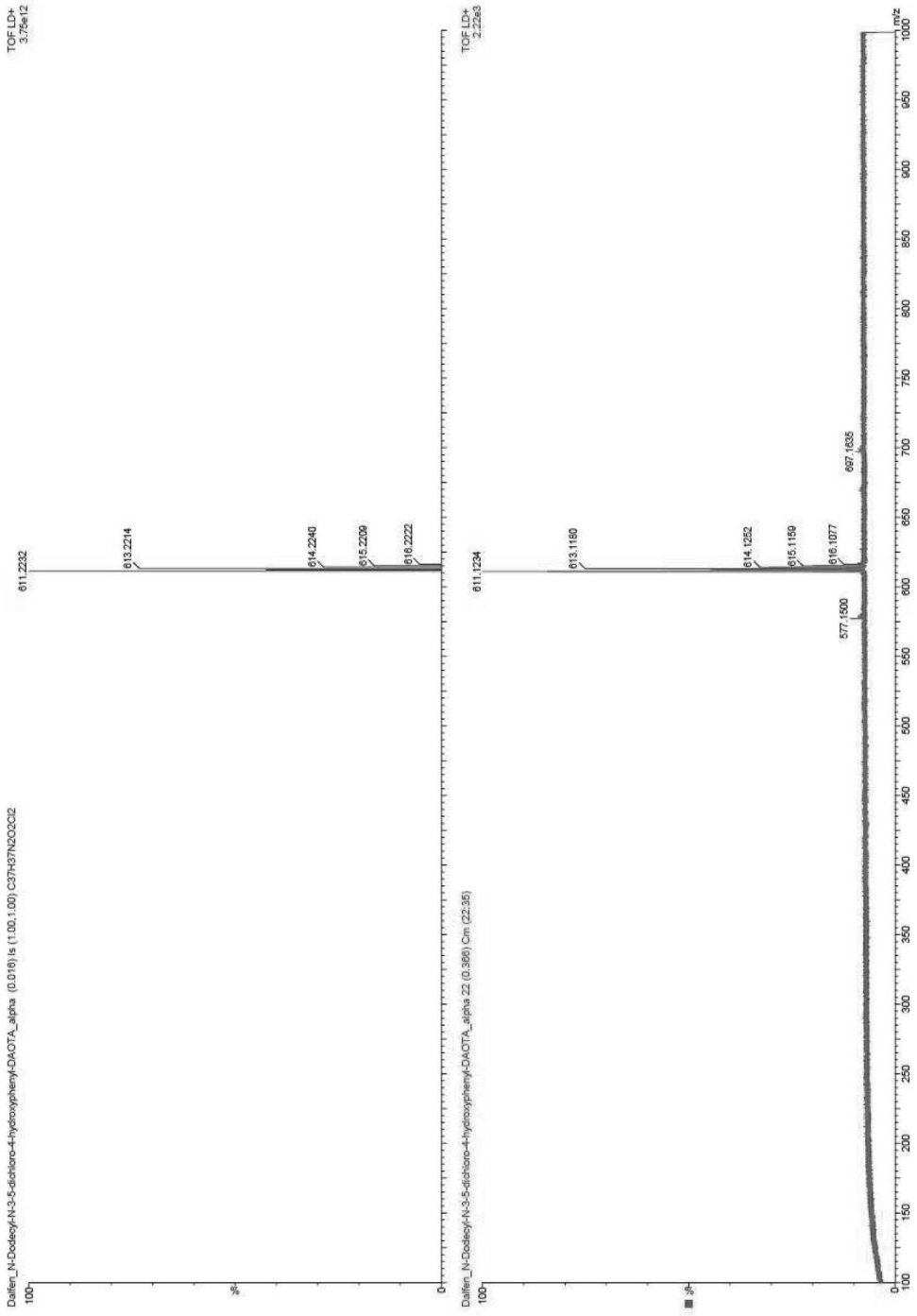

Figure 10.43: MALDI-TOF spectrum of compound **(4)**in an alpha matrix;
upper graph: calculated isotope pattern [M$^+$]=611.22; lower graph: detected isotope pattern [M$^+$]=611.12

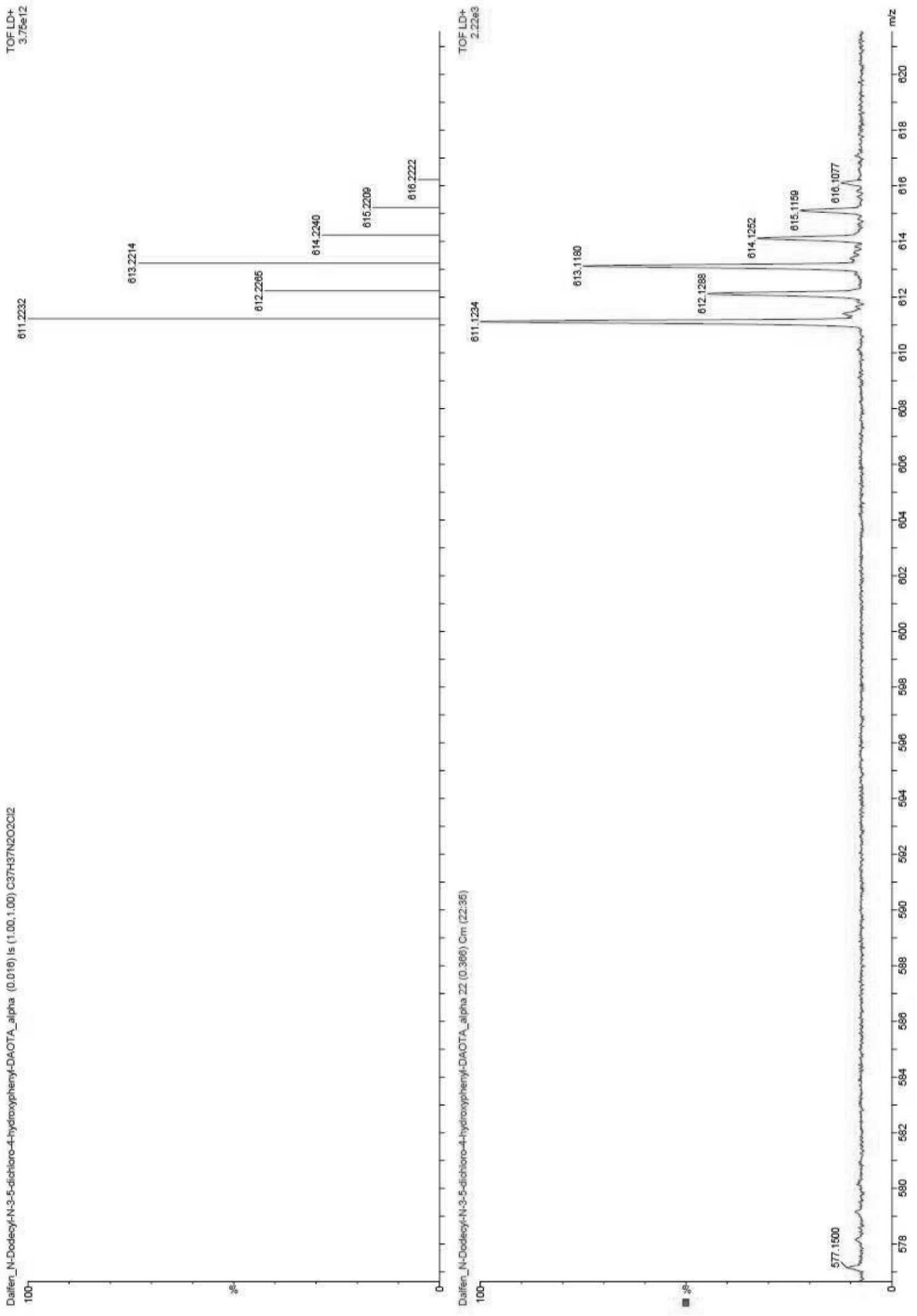

Figure 10.44: Closer view on MALDI-TOF spectrum of compound **(4)**in an alpha matrix; upper graph: calculated isotope pattern $[M^+]$=611.22; lower graph: detected isotope pattern $[M^+]$=611.12

10.2.4 Dye (5) (Monochloro DAOTA$^+$)

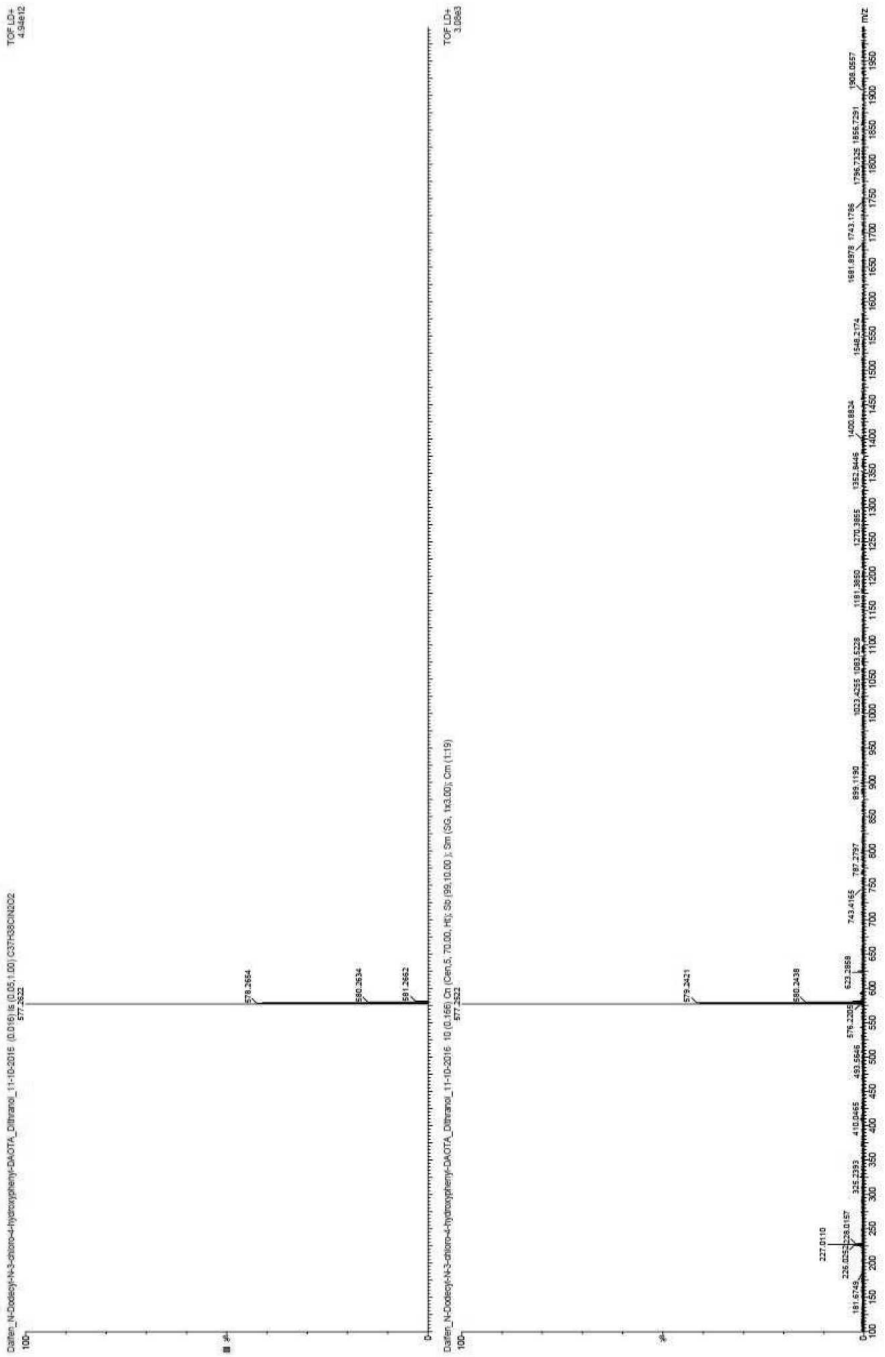

Figure 10.45: MALDI-TOF spectrum of compound **(5)**in a dithranol matrix;
upper graph: calculated isotope pattern [M$^+$]=577.26; lower graph: detected isotope pattern [M$^+$]=577.25

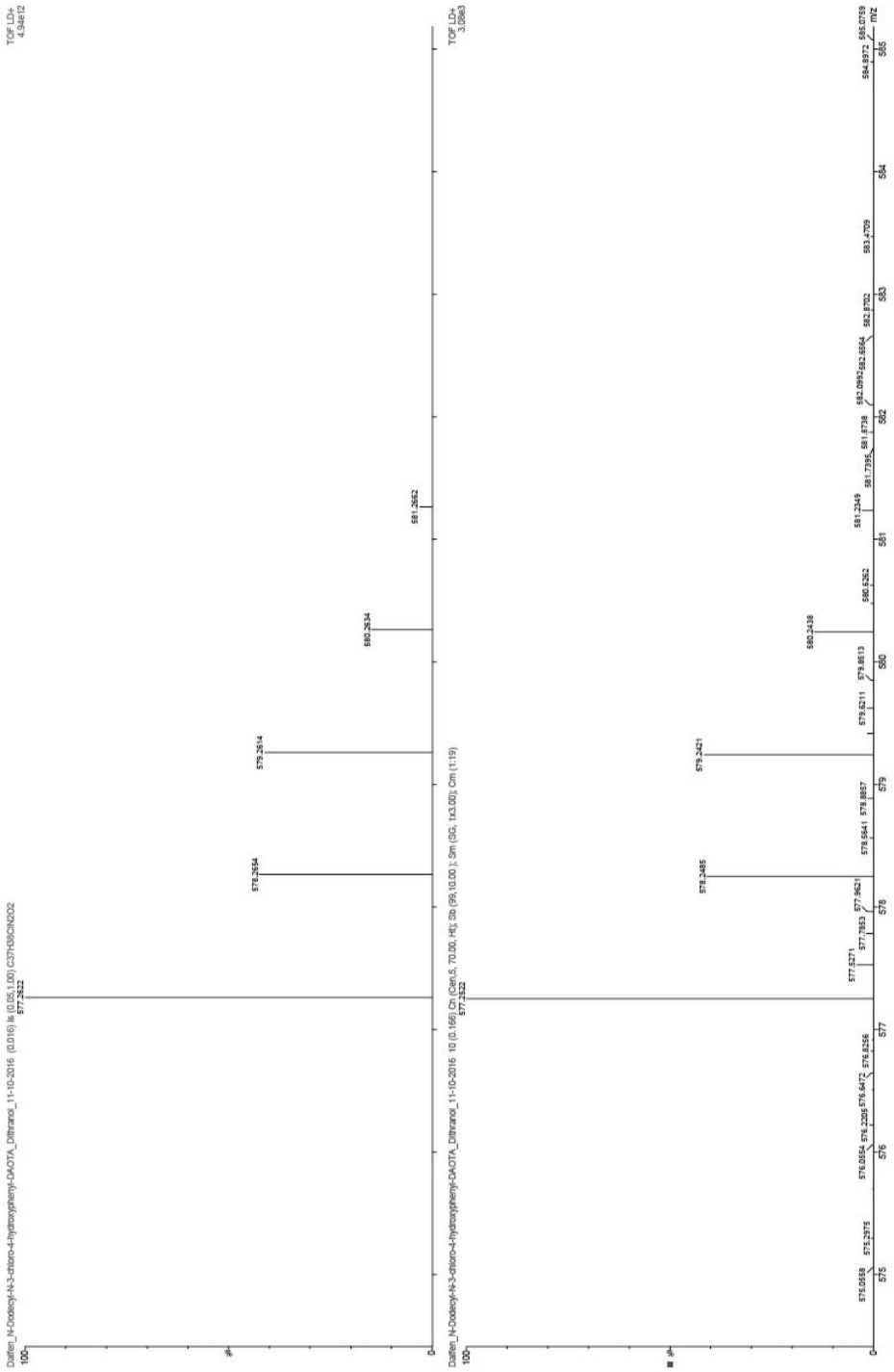

Figure 10.46: Closer view on MALDI-TOF spectrum of compound **(5)**in a dithranol matrix; upper graph: calculated isotope pattern $[M^+]$=577.26; lower graph: detected isotope pattern $[M^+]$=577.25

10.2.5 Compound (6) (Morpholino DAOTA$^+$)

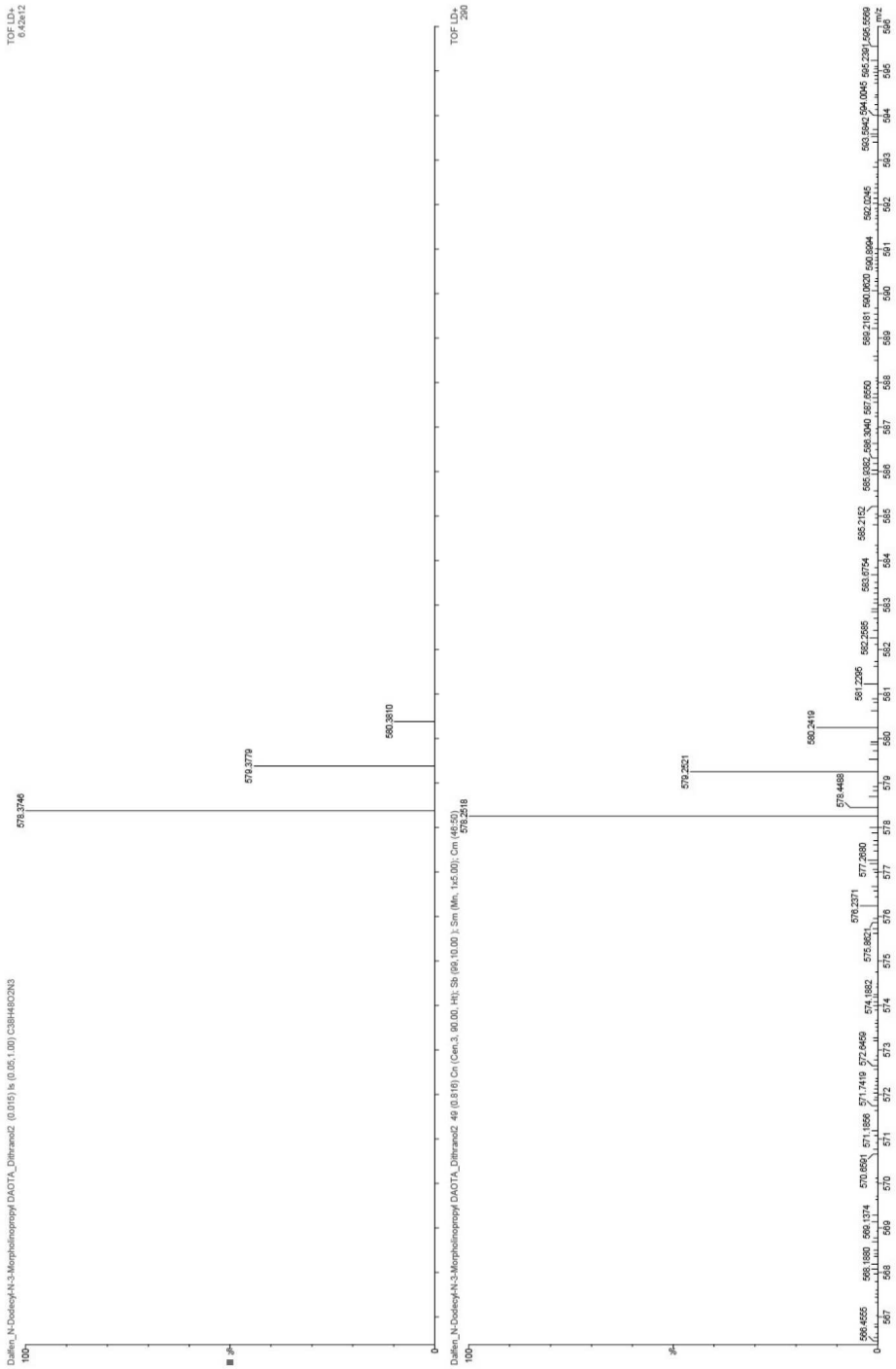

Figure 10.47: MALDI-TOF spectrum of compound **(6)**in a dithranol matrix; upper graph: calculated isotope pattern [M$^+$]=578.37; lower graph: detected isotope pattern [M$^+$]=578.25

10.2.6 Unsucessful Syntheses from Section 4.1.11 (Morpholino and Butyl DAOTA$^+$)

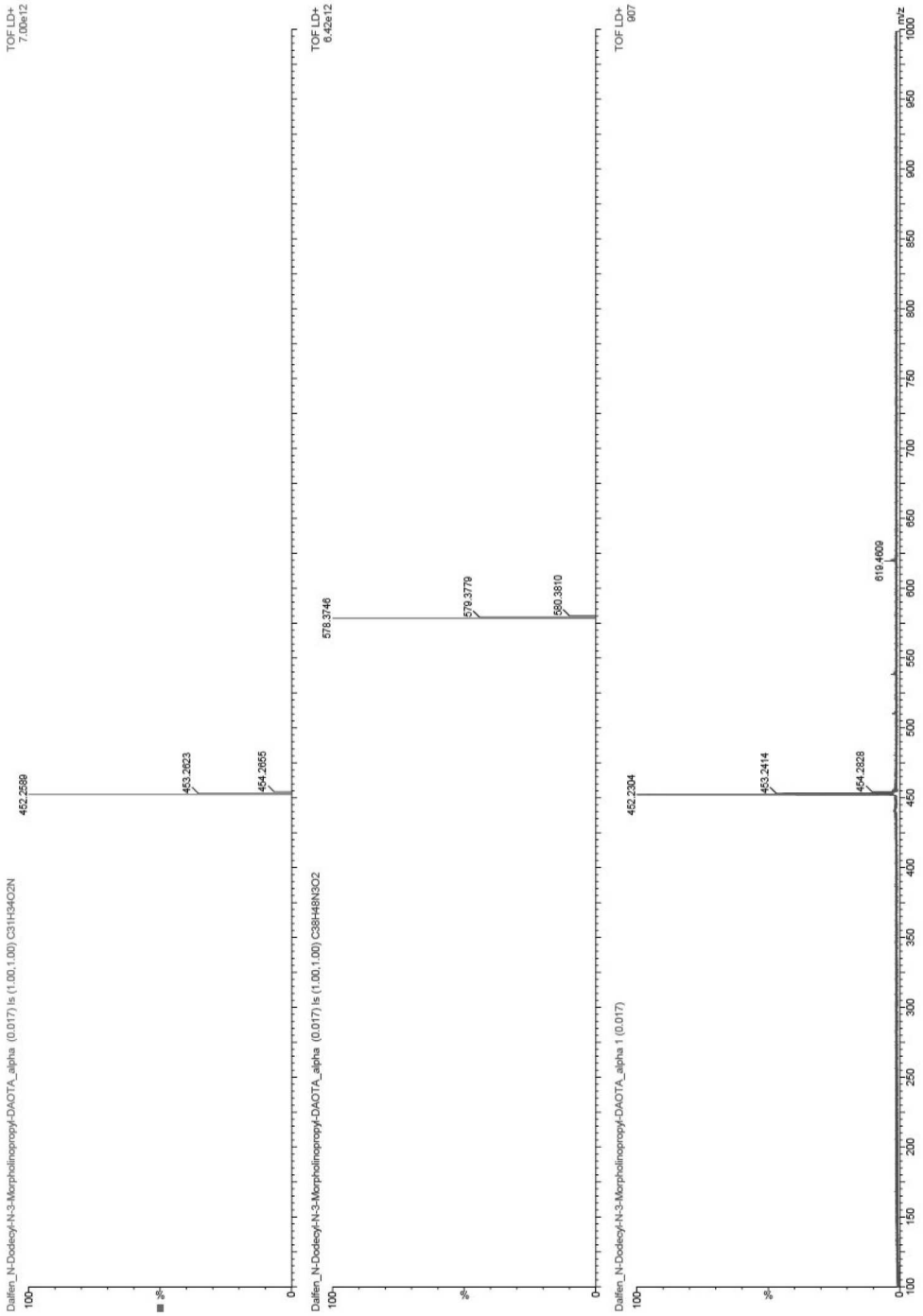

Figure 10.48: MALDI-TOF spectrum of unsuccessful synthesis attempt of **(6)**in an alpha matrix;
upper graph: calculated mass distribution of *N*-dodecyl ADOTA$^+$ [M$^+$]=452.26; middle graph: calculated isotope pattern [M$^+$]=578.37; lower graph: detected isotope pattern [M$^+$]=452.23

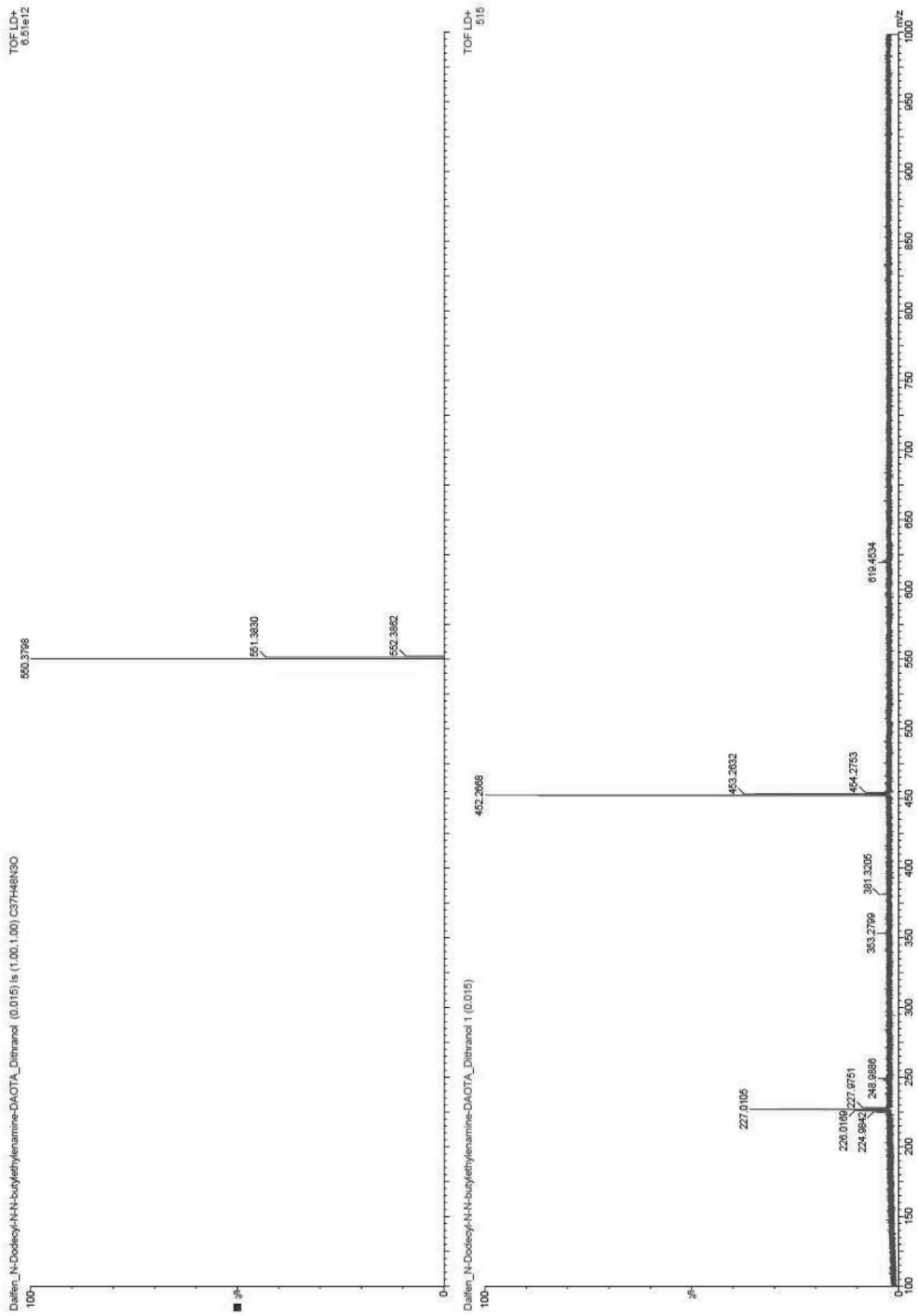

Figure 10.49: MALDI-TOF spectrum of unsuccessful synthesis attempt of *N*-(*N*-Butylethyleneamine)-*N*-dodecyl DAOTA$^+$ in a dithranol matrix;
upper graph: calculated isotope pattern [M$^+$]=550.38; lower graph: detected isotope pattern [M$^+$]=452.23

10.2.7 Unsuccessful Synthesis from Section 4.1.14 (*N*-(3-Chloro-4-hydroxybenzyl)-*N*-dodecyl DAOTA$^+$)

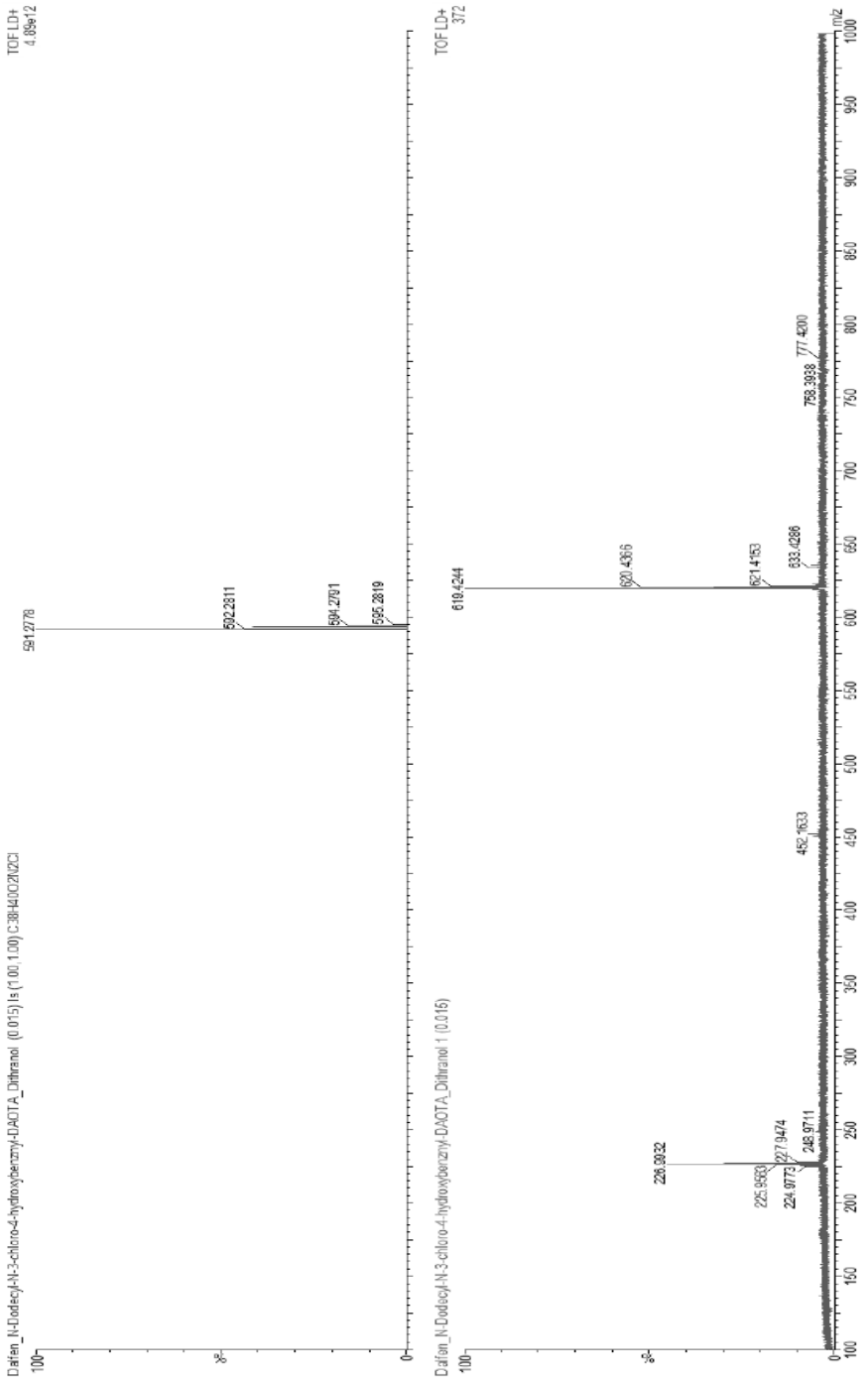

Figure 10.50: MALDI-TOF spectrum of unsuccessful synthesis of *N*-(3-Chloro-4-hydroxybenzyl)-*N*-dodecyl DAOTA$^+$ in a dithranol matrix;
upper graph: calculated isotope pattern [M$^+$]=591.13; lower graph: detected isotope pattern [M$^+$]=619.42

10.3 Additional Absorption/Transmission/Emission Spectra

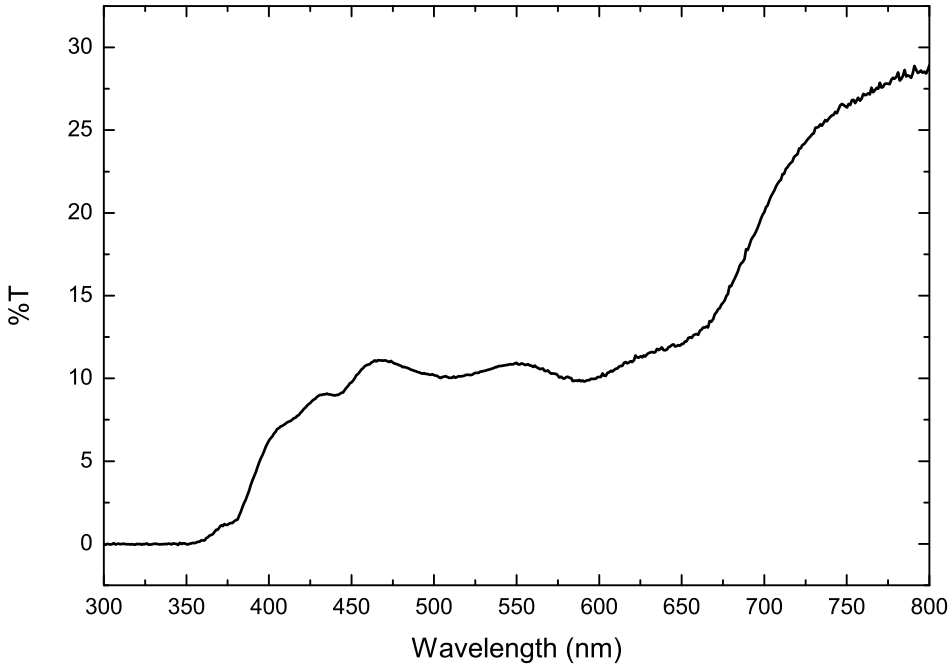

Figure 10.51: Absorption Spectrum of 10 % Transmission Filter

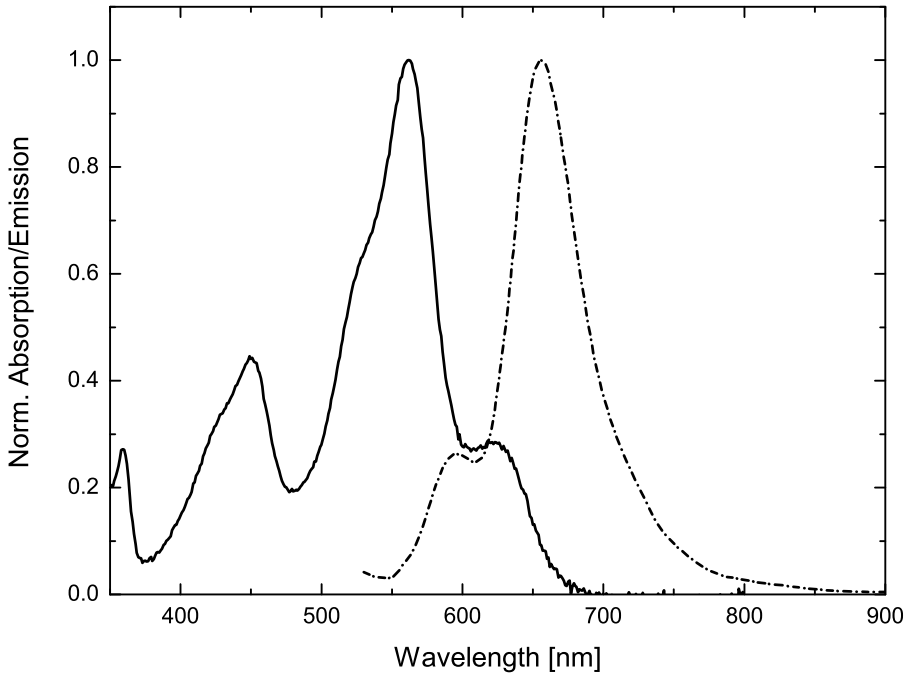

Figure 10.52: Absorption and emission spectrum of dye **(5)** mixed with quinolineacridinium intermediate

10.4 Fluorescence Decay Time pH Calibration of Dye (6)

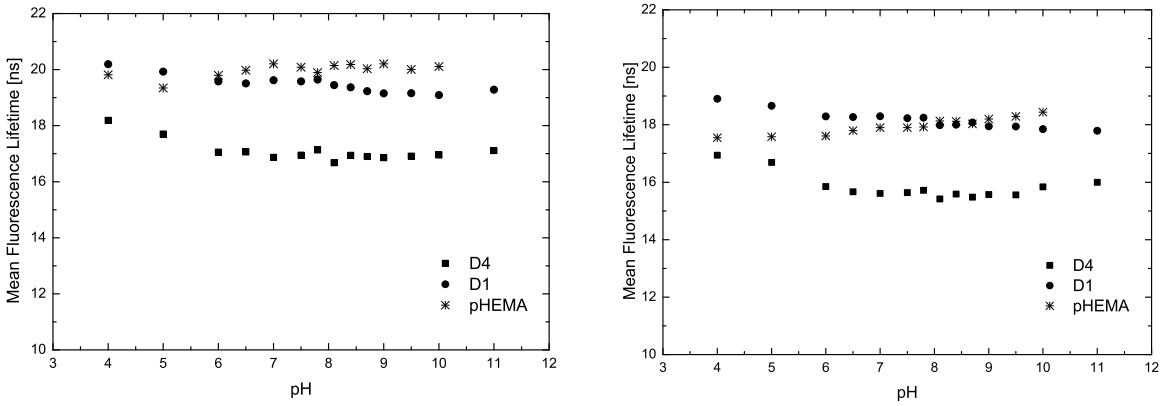

(a) Dye **(6)** fitted biexponentially

(b) Dye **(6)** fitted monoexponentially

Figure 10.53: Fluorescence Lifetime pH Calibration of Dye **(6)** in D4, D1 and pHEMA fitted biexponentially (a) and monoexponentially (b)

10.5 Abbrevations

Table 10.1: List of abbrevations used

Abbreviation	Long name
UV/Vis	Ultraviolet and visible light
IR	Infrared
HOMO	Highest Occupied Molecular Orbital
LUMO	Lowest Unoccupied Molecular Orbital
MO	Molecular Orbital
IC	Internal Conversion
ISC	Inter System Crossing
FLIM	Fluorescence Lifetime Imaging Microscopy
CTAB	Cetyltrimethylammoniumbromide
DOPC	1,2-dioleoyl-*sn*-glycero-3-phosphocholine
PVC	Poly(vinylchloride)
TOTA	Trioxotriangulinium
ADOTA	Azadioxatriangulenium
DAOTA	Diazaoxatriangulenium
H-TOTA	tris(*p*-hydroxy)trioxotriangulenium
A-ADOTA	tris(*p*-dialkylamino)trioxotriangulenium
DCM	Dichloromethane
THF	Tetrahydrofurane
CH	Cyclohexane
EtOH	Ethanol
MeOH	Methanol
Et_2O	Diethylether
NMP	*N*-Methyl-2-pyrrolidon
TEA	Triethylamine
TFA	Trifluoroacetic acid
DMSO	Dimethyl sulfoxide
TMS	Tetramethylsilane
AlOx	Aluminiumoxide
MES	2-(N-morpholino)ethanesulfonic acid
CAPS	N-cyclohexyl-3-aminopropanesulfonic acid
TRIS	tris(hydroxymethyl)aminomethane
TLC	Thin layer chromatography
NMR	Nuclear magnetic resonance
MS	Mass spectrometry
MALDI-TOF	Matrix assisted laser desorption ionisation
PET	Photoinduced Electron Transfer
PMMA-MA	Poly(methylmethacrylat)-methacrylic acid copolymer